

Detection of ultra high energy neutrinos
with an underwater very large volume
array of acoustic sensors:
A simulation study

Den Naturwissenschaftlichen Fakultäten
der Friedrich-Alexander-Universität Erlangen-Nürnberg
zur
Erlangung des Doktorgrades

vorgelegt von
Timo Karg
aus Nürnberg

Als Dissertation genehmigt von den Naturwissenschaftlichen Fakultäten der
Universität Erlangen-Nürnberg.

Tag der mündlichen Prüfung:	25. April 2006
Vorsitzender der Promotionskommission:	Prof. Dr. D.-P. Häder
Erstberichterstatter:	Prof. Dr. G. Anton
Zweitberichterstatter:	Prof. Dr. K.-H. Kampert

Contents

1	Introduction	1
2	Sources of ultra high energy neutrinos	5
2.1	Active Galactic Nuclei	5
2.2	Gamma-ray bursts	7
2.3	The Waxman Bahcall upper limit	8
2.4	GZK neutrinos	8
2.5	Z-Burst neutrinos	10
2.6	Topological Defects	10
2.7	Summary of expected neutrino fluxes	11
3	Detection of ultra high energy neutrinos	13
3.1	Water-Čerenkov detectors	13
3.2	Extensive Air Shower detectors	15
3.3	Radio-Čerenkov detectors	17
3.3.1	Radio detection in ice — RICE	17
3.3.2	Radio observations of the moon — GLUE	18
3.3.3	Satellite experiments — FORTE	19
3.3.4	Balloon experiments — ANITA	19
3.4	Present limits on the neutrino flux	20
4	Thermoacoustic sound generation	25
4.1	Theoretical considerations	25
4.2	Experimental verification of the thermoacoustic model	28
4.2.1	The proton beam experiment	28
4.2.2	The laser experiment	36
5	Acoustic signals from ultra high energy neutrinos	41
5.1	Propagation and interaction of ultra high energy neutrinos	41
5.2	Hadronic cascades	45
5.3	Electromagnetic cascades and the LPM effect	47

6	Sound propagation and detection in water	51
6.1	Attenuation in fresh water and sea water	51
6.2	Refraction and Reflection	54
6.3	Background noise and signal extraction	57
6.3.1	Properties of the background noise	57
6.3.2	Filtering in the time domain	59
6.3.3	Filtering in the frequency domain	60
6.4	Parameterisation of the acoustic signal	60
7	Simulation study of an acoustic neutrino telescope	65
7.1	Detector simulation	65
7.2	Event reconstruction and selection cuts	69
7.3	Separation of background	76
7.4	Sensitivity of an acoustic neutrino telescope	77
7.5	Comparison with other simulations	84
8	Summary	87
9	Zusammenfassung	91
A	Derivation of the thermoacoustic model	95
B	On the calculation of flux limits	99
	Bibliography	103

List of Figures

1.1	Viktor F. Hess	1
1.2	Project Poltergeist	2
1.3	Principle of acoustic neutrino detection	3
2.1	Schematic of an Active Galaxy	6
2.2	Fireball shock model of gamma-ray bursts	7
2.3	Cosmic ray spectrum at the ankle	9
2.4	Z-burst cross section	11
2.5	Expected flux of ultra high energy neutrinos	12
3.1	Detection principle of Water-Čerenkov detectors	14
3.2	Detection principle of the Pierre Auger hybrid detector	16
3.3	Geometry for lunar neutrino cascade detection	18
3.4	The ANITA instrument	20
3.5	Detection principle of ANITA	21
3.6	Experimental limits on the UHE neutrino flux	22
3.7	Comparison of theoretical flux models and experimental limits	23
4.1	The γ parameter of water as a function of temperature	27
4.2	Experimental setup of the proton beam experiment	29
4.3	Energy density deposited by a 180 MeV proton in water	30
4.4	Profile of the proton bunch	31
4.5	Simulated pressure pulses produced by the proton beam	31
4.6	Contribution of different parts of the energy distribution to the acoustic signal	33
4.7	Comparison of measured and simulated signal	34
4.8	Dependency of the signal amplitude on the distance	35
4.9	Amplitude of the proton beam signal as a function of temperature	36
4.10	Laser induced pressure pulses	38
4.11	Amplitude of the laser induced signal as a function of temperature	39
5.1	Mean free path length for neutrinos traversing the Earth	43
5.2	Distribution of the kinematic variable y	44

5.3	Energy density deposited by π^+ mesons in water	46
5.4	Bipolar acoustic signal produced by a 10^5 GeV π^+ meson in water	47
5.5	Normalised cross section for bremsstrahlung	49
5.6	Normalised cross section for pair production	50
6.1	Sonic attenuation length in water	52
6.2	Typical deep sea sound velocity profile	54
6.3	Refraction in a medium with a linear velocity gradient	55
6.4	Geometrically accessible detection volume	56
6.5	Acoustic noise power density in the sea	58
6.6	Coordinate system used for the parameterisation of the pressure field	61
6.7	Dependence of the signal amplitude on the distance	62
6.8	Parameter set to describe the pressure field	63
6.9	Parameterisation of the pressure amplitude	64
7.1	Schematic of the detector simulation setup	66
7.2	Simulated energy spectra	68
7.3	Reconstruction errors for hadronic cascades	71
7.4	Reconstruction errors as a function of the zenith angle	72
7.5	Reconstruction errors as a function of Δ_p , θ_{reco} , and φ_{reco}	73
7.6	Reconstruction errors for hadronic cascades after selection cuts	75
7.7	Energy spectrum of reconstructed events	76
7.8	Distribution of the variables f_{10} , f_{50} , and f_{90}	78
7.9	Effective volume as a function of energy	79
7.10	Effective volume as a function of the detection threshold p_{th}	80
7.11	Effective volume as a function of the sensor density	81
7.12	Effective volume as a function of the instrumented volume	82
7.13	Model independent sensitivity of an acoustic neutrino telescope	83
7.14	Sensitivity of an acoustic neutrino telescope to GZK neutrinos and to the WB limit	84

Chapter 1

Introduction

In astroparticle physics the processes powering the most energetic objects in our universe are studied as well as particle interactions at energies not accessible at accelerator laboratories. Hard x-rays, TeV gamma rays, electrons, hadrons, nuclei, and neutrinos emitted from single stars, but also, for example, from active galactic nuclei and gamma-ray bursts can be observed by experiments on the Earth, by high-altitude balloon experiments, or by satellites.

Until the beginning of the twentieth century, astronomy, and with it our knowledge of the universe, was limited to the observation of visible light.

The field of particle astrophysics was born in 1912, when Viktor Hess undertook several balloon flights up to an altitude of 5200 m to measure the assumed decrease of the ionising radiation known to exist on the Earth's surface, which was believed to originate in the decay of radioactive nuclei in the Earth's crust. What he found was a completely unexpected *increase* of the flux with altitude [1]. In the same publication Hess already suggested, that the radiation must be of extra-terrestrial origin. He was further able to rule out a solar origin, because he did not measure any intensity variations, neither during a day night cycle, nor during a solar eclipse.



Figure 1.1: Viktor F. Hess (1883 – 1964).

Soon people started to study the composition of cosmic rays, and it was found, that they provided excellent means to study particle physics at the highest energies

available at this time. For his discovery Hess was awarded the Nobel prize in 1936 together with Carl D. Anderson, who discovered the positron in the cosmic radiation.

Another important discovery on the way to neutrino astronomy was, of course, the first detection of the (electron anti-)neutrino (which had already been predicted in 1930 by Wolfgang Pauli) in 1956 in the “Project Poltergeist” [2, 3], for which Frederick Reines was awarded the Nobel prize in 1995. To measure the inverse beta decay, his group designed a detector situated near the core of the Savannah River nuclear reactor. It consisted of a water target sandwiched between 4200 litres of liquid scintillator read out by 330 photomultiplier tubes.



Figure 1.2: Frederick Reines’ Project Poltergeist group with the “Herr Auge” detector, a smaller predecessor of the Savannah River detector.

Soon after, also the muon neutrino was discovered, and the possibility of observing extraterrestrial neutrinos was discussed.

Doing astronomy with neutrinos is especially appealing because of their unique properties. Neutrinos are electrically neutral particles, so they are not deflected in the electromagnetic fields present nearly everywhere in the universe. If one can determine the direction of an observed neutrino, the direction will always point back to the source, which is essential for imaging astronomy. Neutrinos have a very small total cross section, so they will (practically) not be absorbed on their way through the interstellar medium. They allow a direct view into cosmological objects, whereas optical astronomy is always confined to the observation of the surface of the source.

The small cross section also poses the great challenge of neutrino astronomy: Enormous target masses are required to observe at least a few neutrino interactions. The flux of cosmological neutrinos is believed to decrease steeply with energy. For energies up to a few hundred TeV, gigaton (1 km^3 of water or ice) detectors are built, which detect the Čerenkov light emitted by muons or cascades produced in neutrino interactions. To measure neutrinos at even higher energies, detectors with an observed target mass in the teraton range (1000 km^3 of water or ice) will be required. There are several different experimental approaches to build such a detector, which want to use a variety of different target media ranging from water and ice, over the Earth’s atmosphere, to the moon.

In this thesis neutrino detection utilising the thermoacoustic sound generation mechanism in fluids is discussed: A neutrino induced hadronic cascade heats a narrow region of the medium, leading to a rapid expansion, which propagates perpendicular to the cascade axis as a bipolar sonic pulse through the fluid (cf. Fig. 1.3). If this pulse of a few ten microseconds length can be recorded at different positions, the direction and energy of the neutrino can be inferred. We will show that a detector consisting of 1000 km^3 of sea water instrumented sparsely with acoustic sensors would allow to detect neutrinos with energies above some EeV¹.

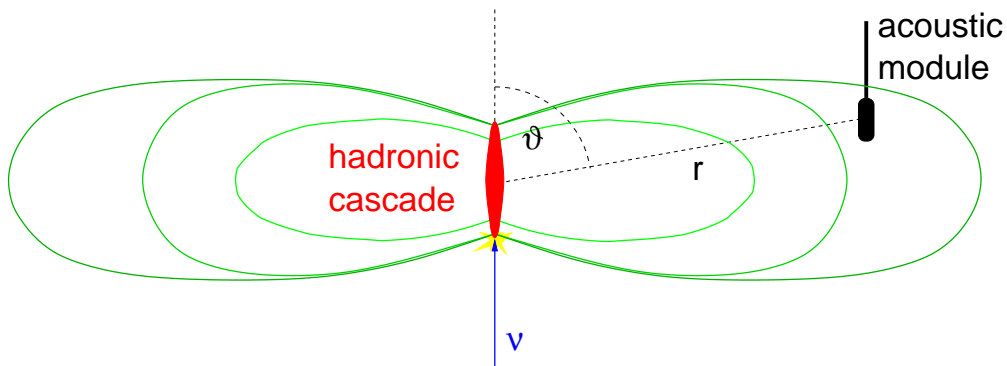


Figure 1.3: Principle of acoustic neutrino detection: Measurement of bipolar pressure pulses, which are emitted perpendicular to a neutrino induced particle cascade developing in a fluid.

In chapter 2 theoretical models of various cosmological sources are presented, which are expected to produce ultra high energy (UHE) neutrinos. Chapter 3 discusses different existing experimental techniques for the detection of ultra high energy neutrinos exemplified by existing or planned experiments. In chapter 4 the thermoacoustic sound generation model is introduced, and measurements for its verification are described. Afterwards, the sound generation of UHE neutrinos in water is analysed in chapter 5, followed by a discussion of the propagation of acoustic signals in sea water and their detection (Chap. 6). Finally, we will present

¹1 EeV = 10^{18} eV.

in chapter 7 a simulation study of an underwater acoustic neutrino telescope, and will derive its sensitivity to a diffuse flux of neutrinos.

Chapter 2

Sources of ultra high energy neutrinos

Contents

2.1	Active Galactic Nuclei	5
2.2	Gamma-ray bursts	7
2.3	The Waxman Bahcall upper limit	8
2.4	GZK neutrinos	8
2.5	Z-Burst neutrinos	10
2.6	Topological Defects	10
2.7	Summary of expected neutrino fluxes	11

In this chapter several theoretical models are discussed, which predict the emission of ultra high energy neutrinos.

2.1 Active Galactic Nuclei

The model of the Active Galactic Nucleus (AGN) was developed to describe a whole range of cosmological objects. These include Seyfert galaxies¹, blazars, and quasars [4]. AGNs are spiral galaxies with a super massive ($10^7 - 10^9$ solar masses) black hole at the centre, which accretes matter from its host galaxy. Particles can be accelerated to ultra high energies by Fermi acceleration in jets perpendicular to the accretion disc.

AGNs are characterised by a very high energy output from a relatively small volume. A schematic of an Active Galactic Nucleus is shown in Fig. 2.1. Depending on the direction under which an AGN is observed, its spectrum will show various

¹Galaxies with very broad emission lines.

prominent features. If the accretion disc is observed edge-on all visible light is usually absorbed in molecular clouds in and around the disc, and a strong radio source with no optical counterpart is measured. In the case where AGNs are observed in the direction of the jet, a very luminous object with high variability, a *blazar*, is seen. The light from blazars shows a high degree of polarisation, which indicates a synchrotron production mechanism in the magnetic fields of the jet.

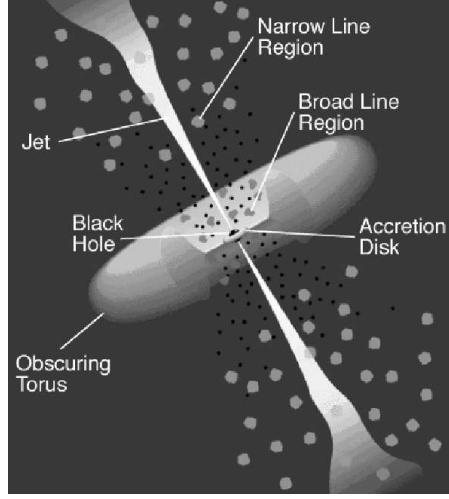
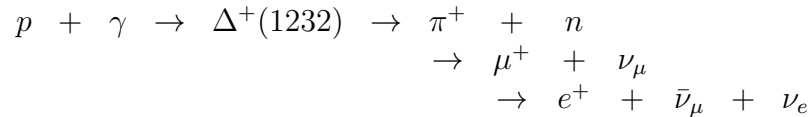


Figure 2.1: Unified model of an Active Galactic Nucleus: The characteristic features observed depend on the direction to the observer.

AGNs are believed to be a source of ultra high energy neutrinos, since the accelerated protons can interact with hadrons or gamma-rays producing charged pions which then decay into leptons and neutrinos, e.g.:



The $\Delta^+(1232)$ can also decay into a proton and a neutral pion, the latter one decaying into two high energy photons, which are a possible source for the high energy (TeV) gamma-rays observed in the cosmic radiation.

The first prediction for the neutrino flux from AGNs was derived in 1991 by Stecker et al. [5, 6] assuming a hidden-core model where all hadronic energy is transformed into neutrinos, and the AGN can thus only be observed in neutrinos. They also pointed out that the main production mechanism must be proton photon interactions, because the column density of hadronic matter surrounding the AGN is limited by the absence of strong x-ray absorption lines in their spectra. Other models predict a neutrino flux at higher energies, e.g. [7], which could already be ruled out by the AMANDA and Baikal [8] experiments. A summary of the neutrino fluxes predicted by the source models described in this chapter is shown in Fig. 2.5.

2.2 Gamma-ray bursts

Gamma-ray bursts (GRBs) are sudden, very short (from milliseconds up to a few seconds) and very intense flashes of gamma-rays, which were discovered in the late 1960s by the Vela military satellites monitoring the Nuclear Test Ban Treaty. It was found that GRBs are accompanied by an afterglow in the x-ray, optical, and radio band. GRBs are distributed isotropically over the sky, and spectral analysis of the afterglow revealed that they have high redshifts.

The large distances (high redshifts) require a model, where, under the assumption of isotropic emission, photon energies of 10^{52} erg to 10^{54} erg are produced during the short duration of the burst². In addition, causality and the short timescale limit the spatial extension of the source to the order of tens to hundreds of kilometres. In the *fireball shock model* (e.g. [9]) the collapse of a massive star induces a relativistically expanding e^\pm , γ fireball with Lorentz factors $\Gamma \approx 100$ [10]. The fireball kinetic energy is converted into non-thermal particle and radiation energy in collisionless shocks mediated by chaotic electric and magnetic fields in which the electrons produce a synchrotron power-law radiation spectrum similar to that observed, while inverse Compton scattering of these synchrotron photons extends the spectrum into the GeV range. There are also modifications to this model, which propose an energy release into relativistic jets, reducing the total energy produced to $10^{52} - 10^{54} (\Omega/4\pi)$ erg, where Ω is the solid angle of the jets (cf. Fig. 2.2).

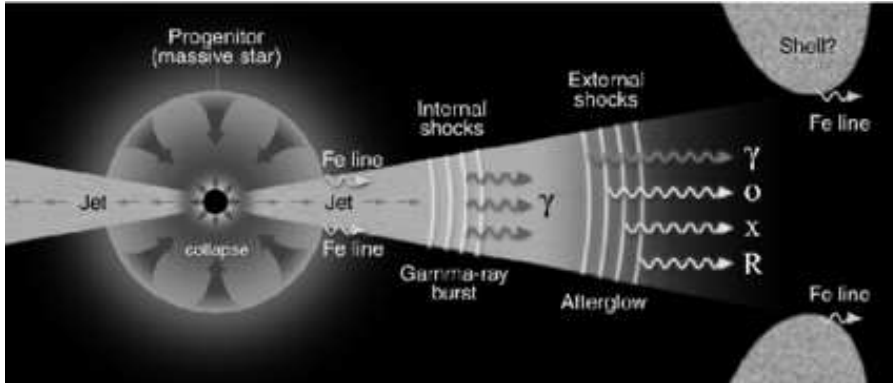


Figure 2.2: The fireball shock model of gamma-ray bursts (from [9]).

In the same shock fronts where electrons are accelerated to highest energies also protons should be accelerated. These ultra high energy protons will be converted into neutrinos by the same mechanism as described for AGNs (cf. Sec. 2.1).

The model predicts a neutrino flux with a power law energy spectrum $\Phi_\nu \propto E_\nu^{-2}$, as expected for first order Fermi acceleration [10, 11]:

²For comparison: Luminosity of the sun $L_\odot = 3.8 \cdot 10^{33}$ erg/s.

$$E_\nu^2 \Phi_{\nu,GRB} = 3.0 \cdot 10^{-9} \text{ GeVcm}^{-2}\text{s}^{-1}\text{sr}^{-1} \quad 10^5 \text{ GeV} < E_\nu < 10^7 \text{ GeV}$$

For energies $E_\nu > 10^7 \text{ GeV}$ the neutrino spectral index rises (i.e. the flux decreases faster), since these neutrinos are produced by charged pions and muons with energies above the synchrotron emission threshold. These pions and muons lose a considerable amount of their energy by synchrotron emission before decaying, producing lower energy neutrinos. The expected neutrino spectrum is shown in Fig. 2.5.

2.3 The Waxman Bahcall upper limit

The Waxman Bahcall (WB) limit [11] is a model independent upper bound to the flux of ultra high energy neutrinos derived from the measured flux of UHE cosmic hadrons and the assumption of optically thin sources, i.e. sources of size not much larger than the mean free path for proton photon interactions.

The assumption of optically thin sources is motivated by the fact, that cosmic rays with energies up to 10^{11} GeV have been observed at Earth, which disfavours the AGN hidden core model, where all hadrons are absorbed within the source. It is applicable to all sources where protons are Fermi accelerated to ultra high energies and interact with ambient photons or protons, like AGNs or GRB fireballs. Assuming that the *complete* energy observed in UHE cosmic rays would be transformed into neutrinos one can derive a strict upper limit on the flux of UHE neutrinos:

$$E_\nu^2 \Phi_{\nu,WB} = 2.0 \cdot 10^{-8} \text{ GeVcm}^{-2}\text{s}^{-1}\text{sr}^{-1}$$

This limit overestimates the most likely neutrino flux by a factor of approximately $5/\tau$, for small optical depths τ (number of proton photon interaction lengths) [12], since in proton photon interactions only 20% of the proton energy is transferred to the charged pion.

The flux of GRB neutrinos presented in Sec. 2.2 is compatible with the WB bound. However, the AGN neutrino fluxes discussed in Sec. 2.1 exceed the bound, but they were derived under the assumption of optically thick sources. These models can thus not be tested by cosmic ray observations on Earth, but only by the detection of the corresponding neutrinos.

2.4 GZK neutrinos

One of the most promising models predicting ultra high energy neutrinos is the GZK effect. It was first described in 1966 by Greisen [13], Zatsepin, and Kuzmin [14] who

inferred that cosmic ray protons with energies $E_p \gtrsim 50$ EeV should interact with the 2.7K cosmic microwave background (CMB). In this interaction mostly $\Delta^+(1232)$ are produced, which partly decay into π^+ and subsequently into neutrinos giving rise to a flux of ultra high energy neutrinos if there are sources of UHE protons with redshifts $z \gtrsim 1$ (which is approximately the interaction length for proton photon interactions). It is widely believed that for example AGNs and GRBs, which have been measured with much higher redshifts, are the required proton sources. The non-existence of the GZK cutoff would lead to the need of a strongly modified cosmology, in the sense that the (yet unknown) sources of ultra high energy cosmic rays must be very close to us, at redshifts $z < 1$.

However, there is still disagreement between cosmic ray experiments whether there is a GZK cutoff. Figure 2.3 shows the energy spectrum of cosmic rays at the “ankle” measured by different experiments. Clarification is expected from the results of the Pierre Auger Observatory (cf. Sec. 3.2), which began to measure cosmic rays at highest energies in 2004.

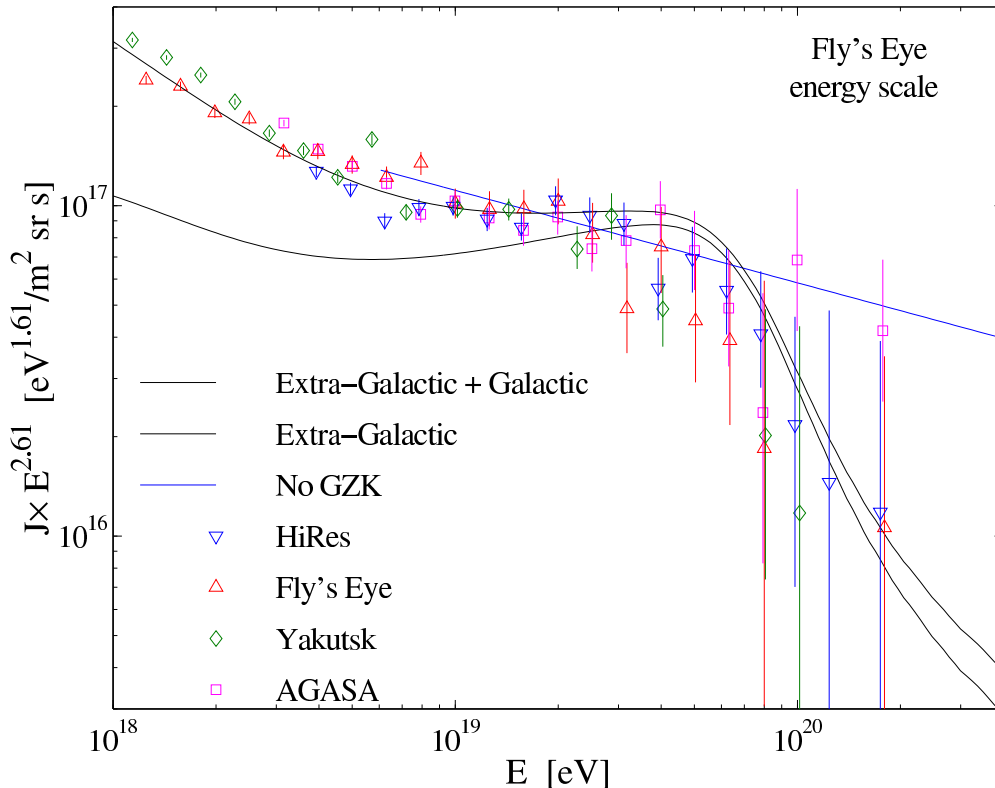


Figure 2.3: The spectrum of cosmic rays at the ankle measured by different experiments (from [15]). The Fly’s Eye and HiRes data suggest the existence of the GZK cutoff (cosmic ray spectrum expected including the GZK cutoff is indicated by the black curves); AGASA on the other hand does not see a cutoff (blue curve).

Detailed calculations [16] using different cosmic ray source distributions, cosmic ray injection spectra, cosmological evolution of the sources, and different cosmologies lead to a considerable neutrino flux exceeding even the Waxman Bahcall bound between 10^8 GeV and 10^{11} GeV (see Fig. 2.5). This is not in contradiction to the WB upper limit, since via the GZK effect, the integrated proton flux above the GZK threshold is scaled down in energy below this threshold through neutrino production. Thus there is an accumulation of the neutrino flux around the GZK threshold.

2.5 Z-Burst neutrinos

Another possible production mechanism for ultra high energy neutrinos are Z-bursts, which are particularly interesting, since they would allow, if detected, the determination of the absolute neutrino mass.

Similarly to the cosmic microwave background the universe is presumably filled with a background of relic neutrinos from the big bang, which decoupled when the universe had cooled down to a temperature of $kT \approx 2$ MeV [17]. At present time these neutrinos have a number density of 114 cm^{-3} per massive neutrino family with a black body temperature of 1.9 K.

The only cosmic ray process sensitive to these relic neutrinos is the Z-burst scenario [18]. An ultra high energy neutrino emitted by a cosmic accelerator and propagating through the universe can interact with a relic neutrino producing a Z boson. The Z decays in 70% of all cases into hadronic jets, which produce neutrinos with a somewhat lower energy, but with a great multiplicity. This leads to a very high neutrino flux around the Z resonance. Figure 2.4 shows the cross sections for ultra high energy neutrinos propagating through the black body neutrino background. For lower neutrino masses the resonance is shifted to higher energies.

In Fig. 2.5 two different predictions for the Z-burst neutrino flux are shown.

2.6 Topological Defects

The last model to be presented in this section is different from the other models discussed so far, because it does not require any hadronic accelerators.

In the early universe, when the symmetry of the Higgs field was broken at the GUT scale, regions which were causally not connected might have acquired Higgs fields with different “orientations”. The boundaries between such domains with different ground states are called *topological defects* (TD), because their manifestation is determined by the topology of these regions. Topological defects may appear as so called domain walls, cosmic strings, monopoles, or textures [20].

The energy associated with a topological defect is of the order of magnitude

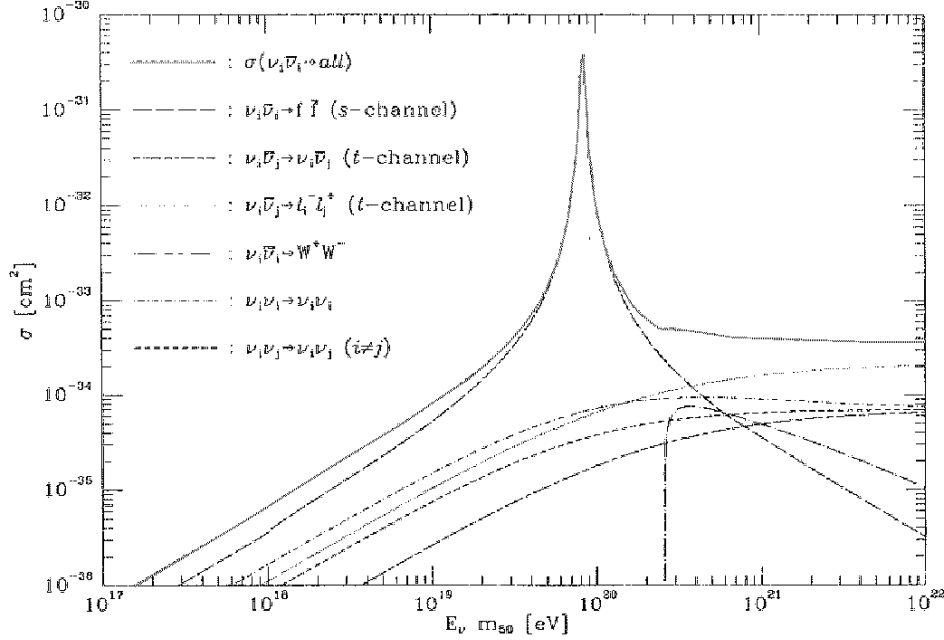


Figure 2.4: Cross section for the production of Z bosons by ultra high energy neutrinos propagating through the 1.9 K black body neutrino background as a function of the neutrino energy times $m_{50} = m_\nu/50$ eV (from [19]).

of the GUT energy, i.e. 10^{15} GeV to 10^{16} GeV. This energy is released during the annihilation or collapse of the defects in the form of super massive gauge bosons and Higgs bosons, which are usually referred to as X particles [21].

These X particles can decay into leptonic and hadronic channels, the latter one producing ultra high energy neutrinos in hadronic cascades, which will not be associated with any cosmic accelerators. The neutrino flux predicted from TD models is shown in Fig. 2.5.

2.7 Summary of expected neutrino fluxes

Figure 2.5 shows the flux of ultra high energy neutrinos predicted by the models discussed in this chapter. On the ordinate the neutrino flux multiplied by E_ν^2 is plotted, so that models predicting a flux proportional to E_ν^{-2} as from first order Fermi acceleration are flat in this representation. The plot gives the total flux over all (anti-)neutrino flavours, since the acoustic detection method discussed in this thesis is not sensitive to lepton flavour. For models where in the literature only the $\nu_\mu + \bar{\nu}_\mu$ flux at Earth is given, this flux is multiplied by a factor of three, since due

to neutrino oscillations an equipartition between all neutrino flavours is expected if the neutrinos are produced in distant and extended sources with a flavour ratio of $\nu_e : \nu_\mu : \nu_\tau = 1 : 2 : 0$, which is the case for cosmic neutrinos from pion decay.

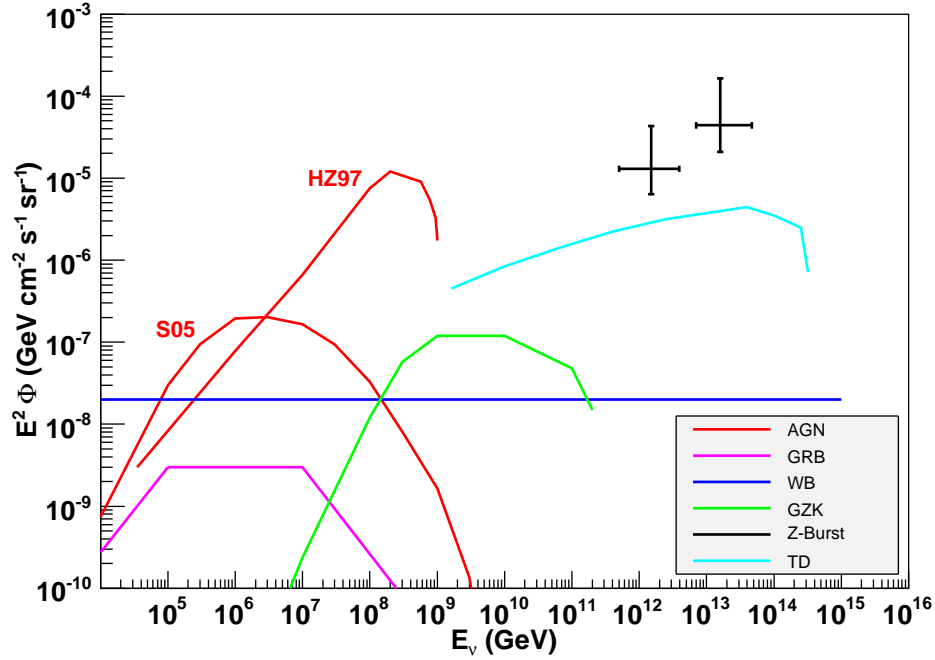


Figure 2.5: Total flux (all flavours) of ultra high energy neutrinos predicted by the various theoretical models. AGNs: S05 from [6], HZ97 from [7]; GRB from [10]; WB from [12]; GZK from [16]; Z-Bursts from [22]; TD from [21] ($m_\nu = 1$ eV).

Chapter 3

Detection of ultra high energy neutrinos

Contents

3.1	Water-Čerenkov detectors	13
3.2	Extensive Air Shower detectors	15
3.3	Radio-Čerenkov detectors	17
3.3.1	Radio detection in ice — RICE	17
3.3.2	Radio observations of the moon — GLUE	18
3.3.3	Satellite experiments — FORTE	19
3.3.4	Balloon experiments — ANITA	19
3.4	Present limits on the neutrino flux	20

In this chapter different experimental approaches towards the detection of ultra high energy neutrinos are discussed and several experiments already existing or starting in the near future are presented.

3.1 Water-Čerenkov detectors

There are several experiments currently taking data or being built, aiming at the detection of cosmic neutrinos in the high-energy range from about 50 GeV to 100 TeV. All these experiments are based on the Water-Čerenkov (or Ice-Čerenkov) technique, i.e. on the detection of Čerenkov photons in the visual frequency band, which are emitted by charged particles propagating at superluminal velocities through a transparent medium (water or ice).

Water-Čerenkov detectors consist of arrays of photomultiplier tubes deeply embedded in water or ice and looking below the horizon for upward going particles, since at these energies neutrinos are the only particles able to propagate freely

through the Earth. The overburden of water or ice, typically several kilometres thick, acts as a shielding against downward going muons from atmospheric air showers, which are produced in interactions of cosmic rays in the atmosphere.

The detectors are designed to detect muon neutrinos interacting via charged current weak interactions in the detector or in the surrounding medium or bottom rock. The produced muon propagates freely through the detector and emits Čerenkov light. The muon path can be reconstructed by measuring the arrival times and the corresponding number of causally connected photoelectrons in the different photomultipliers (cf. Fig. 3.1). At high energies, the direction of the muon coincides well enough with the direction of the initial neutrino, so that the direction of the source can be determined with an angular resolution better than 1° in water. Due to the shorter scattering length of light in ice, the angular resolution of Ice-Čerenkov telescopes is slightly worse; it is about 2° .

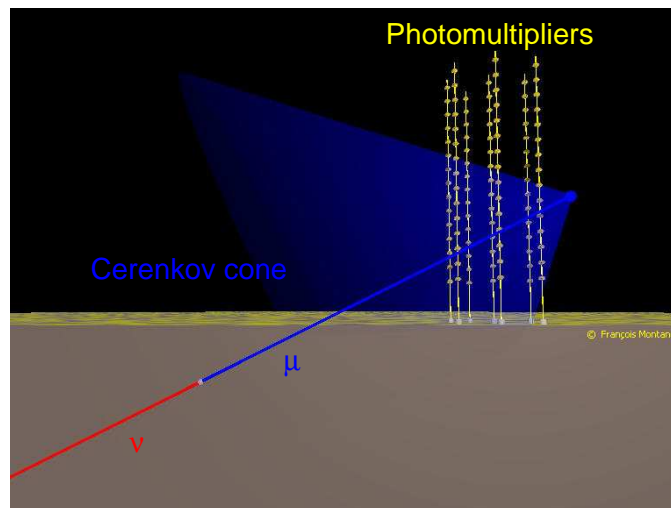


Figure 3.1: Detection principle of Water-Čerenkov detectors: A neutrino interacts in the surroundings of the detector and the resulting muon produces a cone of Čerenkov light, which is detected by photomultipliers.

The lower threshold energy of Water-Čerenkov detectors, which is about 50 GeV, is set by the spacing of the photomultipliers. For lower energies the muon tracks become too short to be resolved by the detector. The upper energy threshold is set by the target mass of the detector. At higher energies, the neutrino flux becomes so low, that the number of neutrinos from the different theoretical source models expected to be measured within the lifetime of the experiment is insufficient to get reliable information.

Table 3.1 summarises the parameters of a selection of existing and planned Water-Čerenkov neutrino telescopes, all of which deploy their photomultipliers fixed to vertical structures which are either frozen into the ice or set on the seabed.

The Baikal¹ experiment is the oldest neutrino telescope which is still taking data. It is situated in Lake Baikal in Siberia, which freezes in winter and thus allows to use the ice sheet as a deployment platform. AMANDA and its successor IceCube² are located at the south pole. Their strings are deployed by hot water drilling into the ice. There are three detectors currently being constructed in the Mediterranean Sea: ANTARES³, NEMO⁴, and Nestor⁵, all using different technical approaches. Further, there are plans for a cubic-kilometre sized counterpart to IceCube in the northern hemisphere: KM3NeT⁶.

Table 3.1: Parameters for a selection of Water-Čerenkov neutrino telescopes. (V : instrumented volume, d_{xy} : horizontal PMT spacing, d_z : vertical PMT spacing)

	Medium	# PMTs	V (km ³)	d_{xy} (m)	d_z (m)	Overburden (m)
Baikal	fresh water	192	10 ⁻⁴	21	5, 7.5	1100
AMANDA	ice	677	10 ⁻²	50	14.0	1500
IceCube	ice	4800	1.0	125	17.0	1400
ANTARES	sea water	900	10 ⁻²	70	14.5	2000

None of the existing experiments could measure an unambiguous signal of cosmic neutrinos, yet. However, there has been a recent observation by the AMANDA experiment of two neutrinos in spatial and temporal coincidence with a TeV gamma flare of the blazar 1ES 1959+650 [23]. Unfortunately, those events were only discovered after the unblinding of the data, and thus their statistical significance cannot be reliably estimated.

3.2 Extensive Air Shower detectors

Another promising approach towards the detection of ultra high energy neutrinos are extensive air shower (EAS) detectors. EAS detectors are designed for the detection of particle cascades produced by cosmic rays in the atmosphere, but new telescopes like the Pierre Auger Observatory⁷ have apertures large enough to detect also very rare neutrino induced cascades.

The Pierre Auger Observatory is a hybrid detector, which uses two independent experimental techniques to measure air showers. The detection principle is shown

¹<http://www.ifh.de/baikal/baikalhome.html>

²<http://icecube.wisc.edu/>

³<http://antares.in2p3.fr/>

⁴<http://nemoweb.lns.infn.it/>

⁵<http://www.nestor.org.gr/>

⁶<http://www.km3net.org/>

⁷<http://www.auger.org/>

in Fig. 3.2: A surface array of 1600 Water-Čerenkov tanks is spread over an area of 3000 km² in a triangular grid with 1.5 km spacing. Each tank contains 12 m³ of water, which is observed by three photomultipliers to measure the spatial and temporal distribution of air shower particles reaching ground level. Further, the whole area is observed by four fluorescence detectors, each of which has a field of view of 180° in azimuth angle. These Fly's Eyes are designed to detect the fluorescence light emitted by atmospheric nitrogen when a particle cascade develops in the atmosphere. Their duty cycle is about 10% since they can only be operated at night and when the weather conditions are suitable.

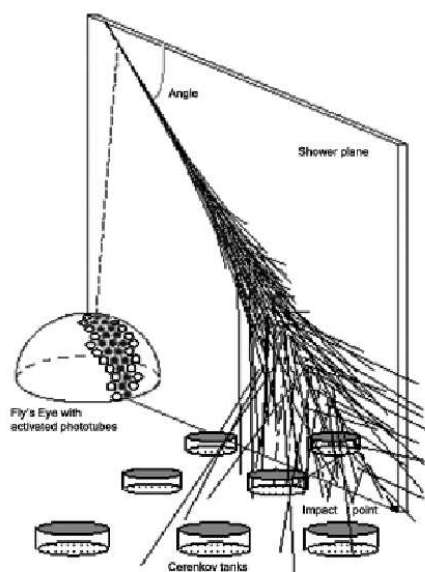


Figure 3.2: Detection principle of the Pierre Auger hybrid detector: The fluorescence light produced by an extensive air shower is detected in Fly's Eye imaging telescopes; particles reaching ground level are measured in Water-Čerenkov tanks.

This hybrid setup allows the reconstruction of the primary particle energy with an error of 9%, and of its direction better than 1° (Surface detector only: 1.4° direction resolution and 10% energy resolution).

The Pierre Auger Observatory can also detect ultra high energy neutrinos if they interact in the atmosphere. Cosmic ray hadrons interact at the top of the atmosphere⁸, whereas neutrinos as only weakly interacting particles can interact at any atmospheric depths. The depth of interaction can be fixed by determining the depth of the shower maximum, i.e. the depth, where the cascade particle density is highest. The shower maximum can either be measured directly by the fluorescence detectors, or can be calculated from the ratio of the number of muons to electrons

⁸At an altitude between 10 and 20 km for a vertically downward going particle.

arriving at ground level and seen by the surface array, since the number of high-energy electrons decreases faster than the number of muons because of their larger electromagnetic cross section.

Promising neutrino candidates are inclined showers with zenith angles larger than approximately 60° , since those showers must have been created deeply in the atmosphere when reaching the surface detector. The neutrino flux predicted to be detectable within one year of measurement time is plotted in Fig. 3.6.

3.3 Radio-Čerenkov detectors

Even larger target masses can be observed if the signal to be detected propagates over wide distances, and thus the number of single sensors can either be reduced, or they can be distributed using larger inter-sensor spacing. For example, radio waves can propagate over large distances in nearly any medium. Such radio waves are emitted coherently from the excess of negative charge in electromagnetic cascades.

An electromagnetic cascade developing, especially in dense media, gathers an excess of electrons, since positrons annihilate in the medium and additional electrons are gathered via Compton scattering. This propagating, uncompensated charge emits highly polarised Čerenkov radiation, bremsstrahlung, and transition radiation, which are coherent for wavelengths larger than the extensions of the cascade [24]. Since ultra high energy electromagnetic cascades in matter typically have a length of several metres, coherent emission is expected in the radio frequency band.

This is called Askarian effect. It was verified experimentally by directing picosecond pulses of GeV bremsstrahlung photons into a silica sand target, where nanosecond radio-frequency pulses in the 0.3 GHz to 6 GHz range were measured [25]. This allows for simple and cheap experiments, since only conventional radio antennas are required for detection.

In the next sections different experimental approaches to detect this coherent Radio-Čerenkov radiation are presented which presently set the best experimental limits on the flux of ultra high energy neutrinos. These upper limits on the neutrino flux are summarised in Sec. 3.4.

3.3.1 Radio detection in ice — RICE

The Radio Ice Čerenkov Experiment⁹ (RICE) consists of an array of 18 radio antennas deployed together with the AMANDA detector in the antarctic ice cap. The antennas are spread over a $200 \times 200 \times 200 \text{ m}^3$ cube in a depth of 100 to 300 m, and are sensitive from 0.2 GHz to 1 GHz [26].

This setup is designed to detect the radio emission and reconstruct the vertex of electromagnetic cascades induced by UHE neutrinos ($E_\nu \gtrsim 10^7 \text{ GeV}$) in an effective

⁹<http://www.bartol.udel.edu/~spiczak/rice/rice.html>

volume of $2 \times 2 \times 1 \text{ km}^3$ around the detector. Neutrino signals can be discriminated from background by the characteristic conical emission pattern of the cascade: the Čerenkov cone, whereas the background typically is produced by point sources, which emit spherical waves. Spherical waves typically produce large-voltage signals in a higher number of antennas than a signal limited to a cone.

RICE is taking data since 2000, and no neutrino candidates were measured yet. The resulting limit on the neutrino flux is shown in Fig. 3.6.

3.3.2 Radio observations of the moon — GLUE

Looking for an even larger monolithic target, which, at the cost of a higher energy threshold, can be observed with a single antenna, one inevitably has to consider the moon.

The Goldstone Lunar Ultra-high energy neutrino Experiment¹⁰ (GLUE) uses the 70 m and the 34 m Deep Space Network antennas at the Goldstone Tracking Facility in California to detect 2 GHz radio signals from the moon, which are produced by neutrino induced cascades.

With this technique cascades up to a depth of 10 m under the lunar surface can be observed, which results in an effective volume exceeding 10^5 km^3 at highest energies [27]. Figure 3.3 shows the geometry under which cascades can be observed, which is limited because the angle for total internal reflection is to the first order the complement of the Čerenkov angle of 56° , and the emitted Čerenkov cone is collimated with a spread of 1° FWHM. The upper limit on the diffuse neutrino flux set by GLUE is shown in Fig. 3.6.

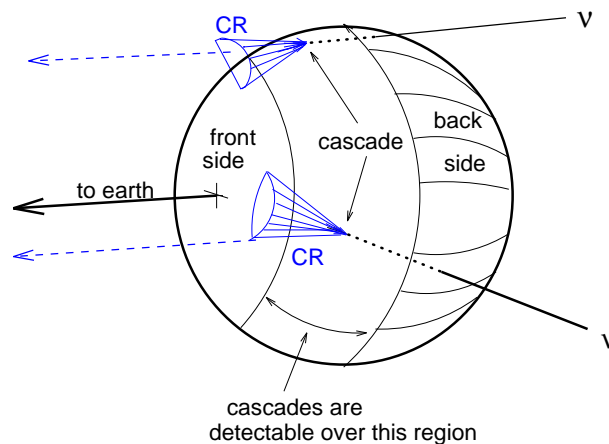


Figure 3.3: Schematic of the geometry for lunar neutrino cascade detection (from [27]).

¹⁰<http://www.physics.ucla.edu/~moonemp/public/>

There are also suggestions to detect the radio emission at lower frequencies in the 150 MHz band [28], where the Čerenkov cone is less collimated, and thus the limitations imposed by total internal reflections are avoided. First estimates show that the sensitivity to UHE neutrinos might be increased substantially compared to the experiments working in the 2 GHz band.

3.3.3 Satellite experiments — FORTE

At highest energies the radio emission from particle cascades in ice can not only be detected in the ice (cf. Sec. 3.3.1) itself, but also with satellites orbiting the Earth.

In 1997 NASA launched the FORTE (Fast On-orbit Recording of Transient Events) satellite¹¹ which carries several instruments for meteorological studies and the U.S. nuclear detonation detection system. Among these are two broadband (30 to 300 MHz) radio-frequency dipole antennas that are orthogonal to each other, and which can also be used to search for radio emission from neutrino induced cascades.

FORTE orbits the Earth at an altitude of 800 km with an inclination of 70° towards the equator. From this orbit it cannot monitor Antarctica, but it can detect events in the Greenland ice sheet with a depth up to 1 km. This results in an effective volume of approximately $2 \cdot 10^6$ km³. Čerenkov radiation is highly polarised which allows to select nanosecond pulses that are neutrino candidates out of a background of lightning and other natural phenomena.

The FORTE collaboration has observed one event, which survives all their selection cuts, and which is still being analysed [29]. Assuming that this single event defines the background rate, one can derive the limit on the neutrino flux shown in Fig. 3.6.

3.3.4 Balloon experiments — ANITA

A new experiment has been proposed which will be able to monitor large masses of Antarctic ice at much lower cost as a satellite.

The Antarctic Impulse Transient Antenna¹² (ANITA) is an instrument planned to contain 40 dual polarisation horn antennas (cf. Fig. 3.4) operating from 0.2 to 1.2 GHz [30].

ANITA will be attached to a balloon and circle the south pole at an altitude of approximately 40 km. As sketched in Fig. 3.5, it will be able to detect nanosecond radio pulses emitted from neutrino induced electromagnetic cascades in the Antarctic ice cap with an effective volume of about 10^6 km³.

Due to the short propagation path of the radio signals compared to FORTE, ANITA will be able to detect neutrinos with a much lower energy threshold of

¹¹http://nis-www.lanl.gov/nis-projects/forte_science/

¹²<http://www.ps.uci.edu/~anita/>

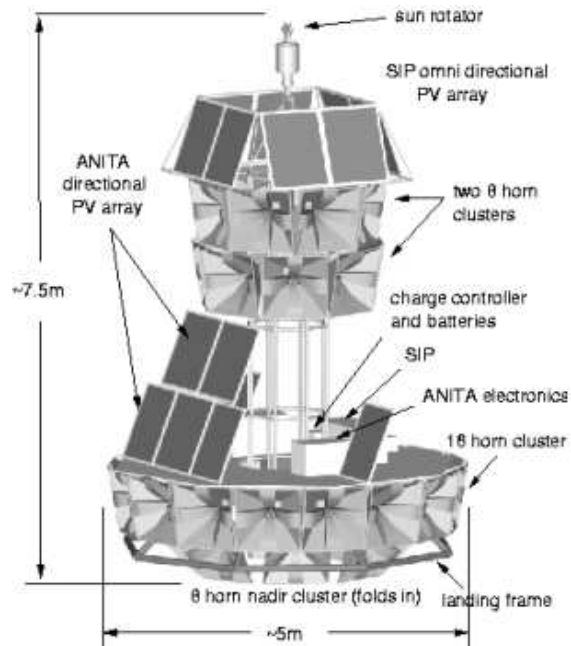


Figure 3.4: The ANITA instrument (from [30]).

10^9 GeV. The neutrino flux expected to be detectable with ANITA during three flights of about 15 days each is shown in Fig. 3.6. The ANITA collaboration has demonstrated the feasibility of the concept with the flight of ANITA-lite [30], and expects to be able to perform one to two flights per Antarctic summer season starting in 2006.

3.4 Present limits on the neutrino flux

Table 3.2 gives, for comparison, an overview over some of the presented existing and planned detectors for ultra high energy neutrinos, stating the energy range and the effective volumes V_{eff} inside which neutrino events can be detected at the highest energies. The upper energy threshold E_{max} is set by the fact, that for the theoretically predicted fluxes (cf. Chap. 2) no events above this energy are expected during the lifetime of the experiment.

In Fig. 3.6 the experimental limits on the neutrino flux, which are set by the different experiments, are summarised. The calculation of these flux limits is discussed in detail in Appendix B. The presented limits are for a 90% confidence level (C.L.). The Auger limit is for one year of lifetime; the ANITA limit is for 45 days, expected to be cumulated during three flights.

The experimental limits are compared to the theoretically predicted flux models shown in Fig. 3.7. The AGN model HZ97 could be excluded by the Baikal and

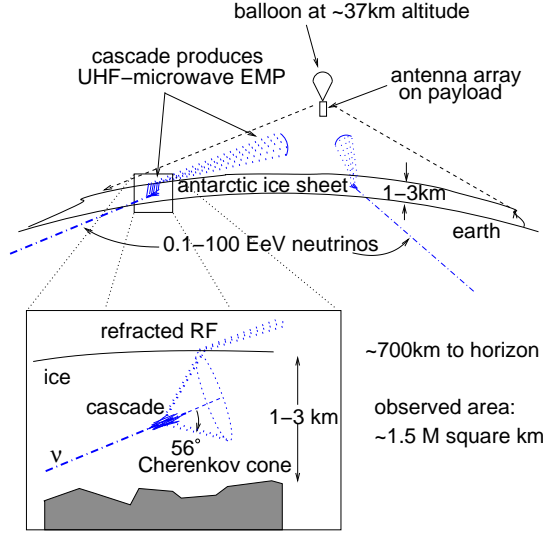


Figure 3.5: Schematic of the detection principle of balloon borne experiments (from [30]).

Table 3.2: Summary of some of the presented neutrino detectors (V_{eff} : effective volume, E_{min} : lower neutrino-energy threshold, E_{max} : upper energy threshold)

	Detection principle	V_{eff} (km^3)	E_{min} (GeV)	E_{max} (GeV)
Baikal	Water-Cherenkov		10^4	10^8
Auger	Air shower		10^8	10^{11}
RICE	Radio-ice in ice	4	10^7	10^{11}
GLUE	Radio-moon from Earth	10^5	10^{11}	10^{14}
FORTE	Radio-ice from satellite	$2 \cdot 10^6$	10^{13}	10^{17}
ANITA	Radio-ice from balloon	10^6	10^9	10^{14}

RICE experiments. GLUE could already rule out different Z-burst scenarios not presented in this work. Auger and ANITA will be able to test the Topological Defect model presented. ANITA will further be sensitive to GZK and WB neutrinos.

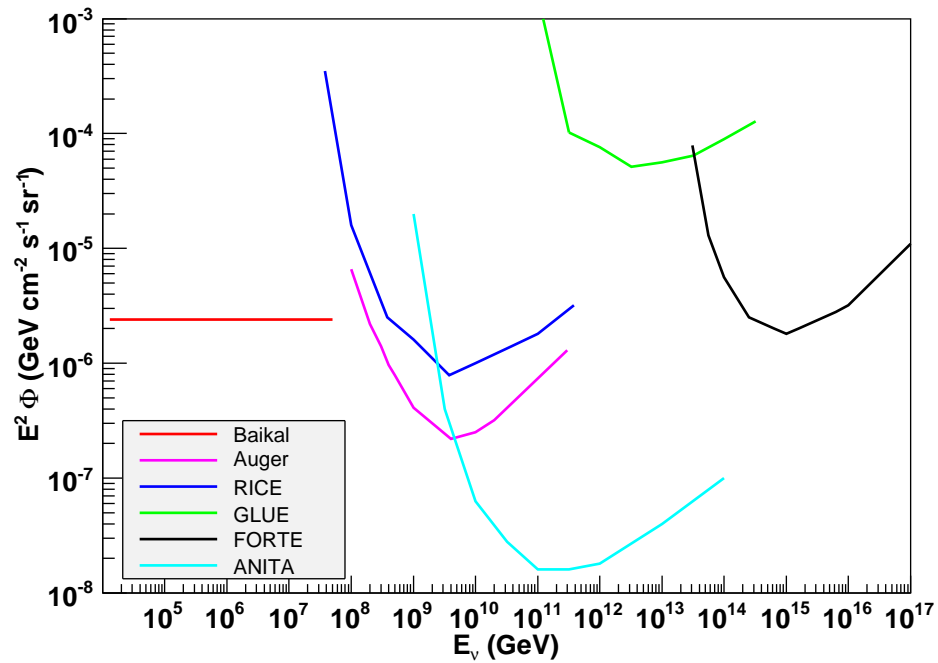


Figure 3.6: Experimental limits on the flux of ultra high energy neutrinos (Baikal from [8], Auger from [31], RICE from [30], GLUE from [32], FORTE from [29], ANITA from [30]).

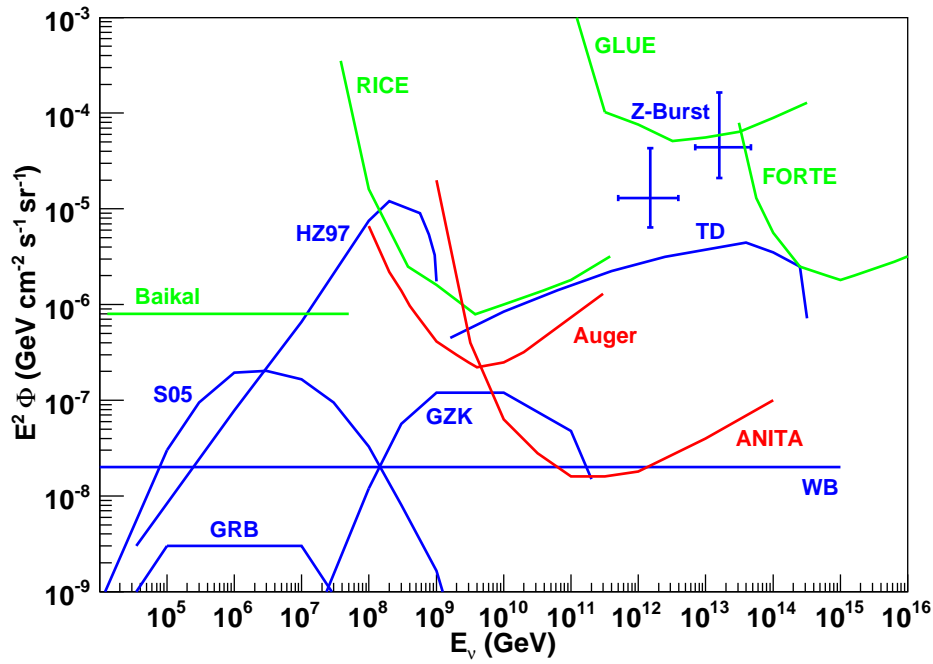


Figure 3.7: Comparison of theoretical flux models and experimental limits. Blue curves are the theoretically predicted fluxes from Fig. 2.5. Green and red curves are the experimental flux limits shown in Fig. 3.6 (Green curves: limits measured by existing experiments; red curves: limits projected for future experiments).

Chapter 4

Thermoacoustic sound generation

Contents

4.1	Theoretical considerations	25
4.2	Experimental verification of the thermoacoustic model	28
4.2.1	The proton beam experiment	28
4.2.2	The laser experiment	36

In this chapter a new approach towards the detection of ultra high energy neutrinos is introduced: Acoustic detection. Thermoacoustic sound generation in general is discussed, and experimental verifications of the thermoacoustic model are presented.

4.1 Theoretical considerations

Acoustic particle detection is based on the thermoacoustic model – a hydrodynamic theory, which was first discussed by G.A. Askarian in 1957 [33, 34].

The basic idea is, that energy deposited locally in a medium, e.g. by a particle cascade, leads to local heating of the medium, and thus to a fast expansion, which spreads in form of a sonic wave from the place of energy deposition. This sound wave is described by a pressure field $p(\vec{r}, t)$, where p is a small deviation from the static pressure p_0 of the fluid. This pressure field can be calculated from the energy density $\varepsilon(\vec{r}, t)$ deposited in the medium. The details are worked out in Appendix A, and the result describing the pressure field is the inhomogeneous wave equation (A.11):

$$\frac{1}{c^2} \frac{\partial^2 p}{\partial t^2} - \Delta p = \frac{\alpha}{C_p} \frac{\partial^2 \varepsilon}{\partial t^2} \quad (4.1)$$

Here, c is the speed of sound, α is the bulk expansion coefficient, and C_p is the specific heat capacity at constant pressure. Equation 4.1 is solved by a *Kirchhoff integral*:

$$p(\vec{r}, t) = \frac{\alpha}{4\pi C_p} \int \frac{d^3 r'}{|\vec{r} - \vec{r}'|} \frac{\partial^2}{\partial t^2} \varepsilon \left(\vec{r}', t - \frac{|\vec{r} - \vec{r}'|}{c} \right) \quad (4.2)$$

This can further be simplified, if we assume an instantaneous energy deposition at time t_0 , i.e. an energy deposition on much shorter timescales, than the propagation of the acoustic wave:

$$\varepsilon(\vec{r}, t) = \tilde{\varepsilon}(\vec{r}) \Theta(t - t_0) \quad \text{or} \quad \frac{\partial}{\partial t} \varepsilon(\vec{r}, t) = \tilde{\varepsilon}(\vec{r}) \delta(t - t_0) \quad (4.3)$$

where $\Theta(t)$ is the Heaviside step function and $\delta(t)$ is the Dirac delta distribution. This assumption is certainly true for the sound generation of particle cascades in water which are considered in this work. Particle cascades, as discussed in the following sections, typically develop with the speed of light in vacuum, whereas the thermoacoustic sound generation is governed by the speed of sound¹, which is much smaller. Inserting (4.3) into (4.2) leads to the following equation:

$$p(\vec{r}, t) = \frac{\alpha}{4\pi C_p} c^2 \frac{\partial}{\partial R} \int_{S_{\vec{r}}^R} d^2 r' \frac{\tilde{\varepsilon}(\vec{r}')}{R} \quad (t > t_0) \quad (4.4)$$

where the integration is over spherical surfaces $S_{\vec{r}}^R$ centred at the observation point \vec{r} and with radius $R = c(t - t_0)$. This means, that for a given position \vec{r} at any time t the thermoacoustic pressure signal is a superposition of all the signal contributions produced in a distance $c(t - t_0)$, i.e. of all the signal contributions that propagate in the given time interval from the production location considered to the observation point.

Using water as detection medium, one has to take further considerations into account. The expansion coefficient α and the heat capacity C_p both strongly depend on the temperature T . Especially, α vanishes at 4°C due to the anomaly of water. The temperature dependent factor in (4.4) is defined as γ , and the temperature dependence is shown in Fig. 4.1.

$$\gamma = \frac{\alpha}{4\pi C_p} \quad (4.5)$$

There are several groups studying the feasibility of using the acoustic signal produced by particle cascades from neutrino interactions as a basis for a future large-scale acoustic neutrino detector. In-situ acoustic measurements using existing arrays (civil and military) of hydrophones as well as custom made detectors have been carried out in Lake Baikal [36], in the Atlantic Ocean near the Bahamas [37], and in the Mediterranean Sea [38, 39].

¹The speed of sound in water is $c \approx 1500$ m/s.

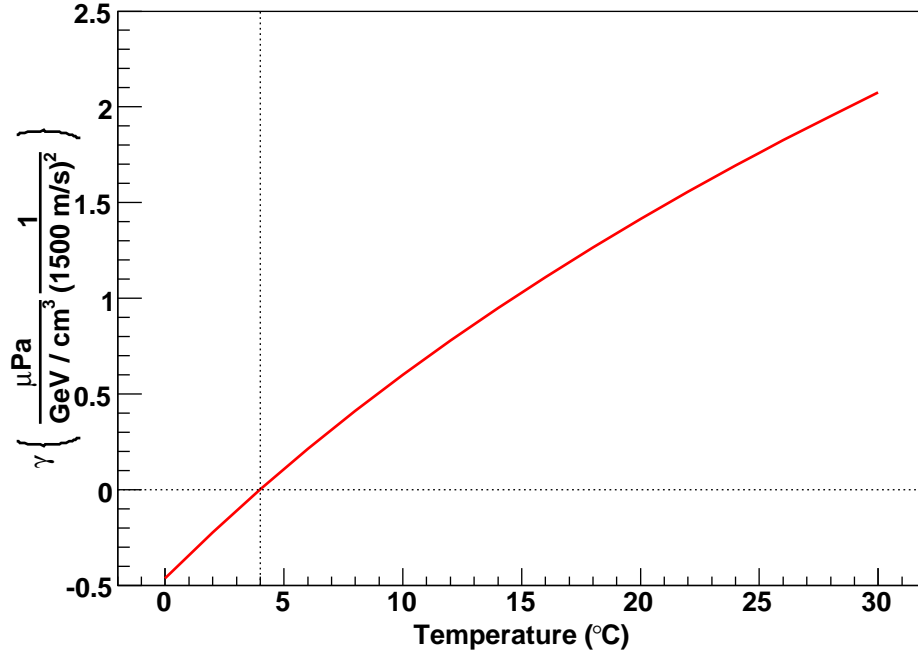


Figure 4.1: The γ parameter of water as a function of temperature in units convenient for the purposes of acoustic particle detection (Data from [35]).

These experiments mainly allowed, apart from addressing the technical feasibility of such a detector, to study the important subject of acoustic background noise in water (cf. Sec. 6.3). Also an experimental limit on the diffuse neutrino flux at energies $E_\nu \gtrsim 10^{13}$ GeV could already be derived from the SAUND experiment at the Bahamas consisting of seven military hydrophones [40], but it is not yet on a competitive basis compared to the FORTE result (Sec. 3.3.3), which is at the moment the best limit in this energy range.

For all those experiments, the vanishing of γ at 4°C, and with it of the thermoacoustic signal, poses no problem since they operate at locations with modest water temperature². For example, at the bottom of the Mediterranean Sea there is a constant temperature between 12°C and 14°C.

²The experiment in Lake Baikal has great systematic limitations due to the temperature gradient between 0°C at the frozen surface and 4°C at the bottom.

4.2 Experimental verification of the thermoacoustic model

In order to study the validity of the thermoacoustic model and to test custom designed hardware like hydrophones we performed several experiments. Different means of energy deposition – a proton beam and a laser – were used to mimic the line-like energy deposition of a particle cascade under controlled conditions. We investigated the dependence of the thermoacoustic pulses on the beam parameters, i.e. intensity and beam width, and on the water temperature. The pulses were measured with both commercial and custom-made hydrophones and were compared to Monte Carlo simulations.

4.2.1 The proton beam experiment

Experimental setup

To test the applicability of the thermoacoustic model to the detection of ultra high energy neutrinos by measuring the sound pulse generated from the neutrino induced particle cascade, an intuitive approach is to dump a particle beam from an accelerator into a water target. It turns out that proton beams with particle energies ranging from a 100 MeV to 1 GeV are ideal candidates for such an experiment, since their range in water is a few 10 cm, a distance most suitable for laboratory setups.

Several such experiments were performed in the past [41, 42, 43], but the results always had large statistical errors as well as systematic uncertainties. Thus, the thermoacoustic sound generation model is verified in principle, but no high precision measurements exist.

We designed and carried out an experiment [44, 45], that would on the one hand allow for precision measurements of the thermoacoustic pressure pulses, especially as a function of the temperature³, and on the other hand give the possibility to test acoustic sensors custom-made for in-situ studies of the background noise in the Mediterranean Sea. In this work I will concentrate on the Monte Carlo studies used to analyse the measured signals. Details on the technical realisation of the experiment can be found in [44].

For the experiment, the 177 MeV proton beam of the Gustaf Werner Cyclotron at the The Svedberg Laboratory⁴ of the University of Uppsala, Sweden was used. The beam was dumped into a $150 \times 60 \times 60 \text{ cm}^3$ water tank. The beam entry window is set about 10 cm from the tank walls into the water volume to delay the

³The temperature dependence is important to distinguish the thermoacoustic signal from pulses produced by other possible sound generation mechanisms which are supposed to persist at 4°C.

⁴<http://www.tsl.uu.se/>

signal reflections from the walls and separate them from the direct signal. This is achieved by a plastic pipe set into the tank wall, where one end is sealed with plastic foil. The acoustic signals were recorded by up to five position adjustable hydrophones simultaneously, and digitised with a rate of 10 MS/s to 100 MS/s. This rate corresponds to a time of 100 ns to 10 ns between two samples which is sufficiently short for an expected length of the thermoacoustic pulse in the order of 100 μ s. The data were stored on disc and analysed off-line. The experimental setup is shown in Fig. 4.2.

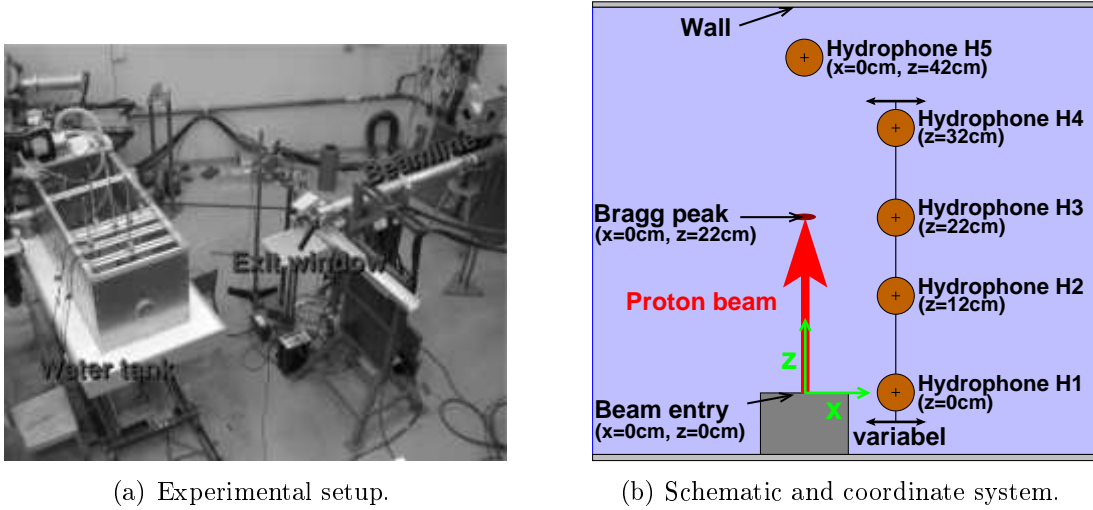


Figure 4.2: Experimental setup of the proton beam experiment: (a) The water tank set up at the end of the beam line, and (b) schematic of the hydrophone positions relative to the beam entry and coordinate system used.

Monte Carlo simulations

To analyse the recorded data we developed a simulation code. In a first step the energy deposition of a single proton in water was studied with GEANT4 [46], an Open Source⁵ simulation package for high energy physics written in C++.

The main energy loss mechanism for 180 MeV protons in a medium is ionisation, which can be simulated with GEANT4 taking into account also scattering along the path. Figure 4.3 shows the mean⁶ energy density deposited by a single 180 MeV proton in water. The proton enters the water at the origin of the coordinate system and propagates in positive z -direction.

Figure 4.3(a) shows that much energy is deposited towards the end of the track, in the so-called “Bragg peak” at $z = 22$ cm. But as can be seen in Fig. 4.3(b),

⁵<http://geant4.web.cern.ch/geant4/>

⁶Averaged over 10000 single protons.

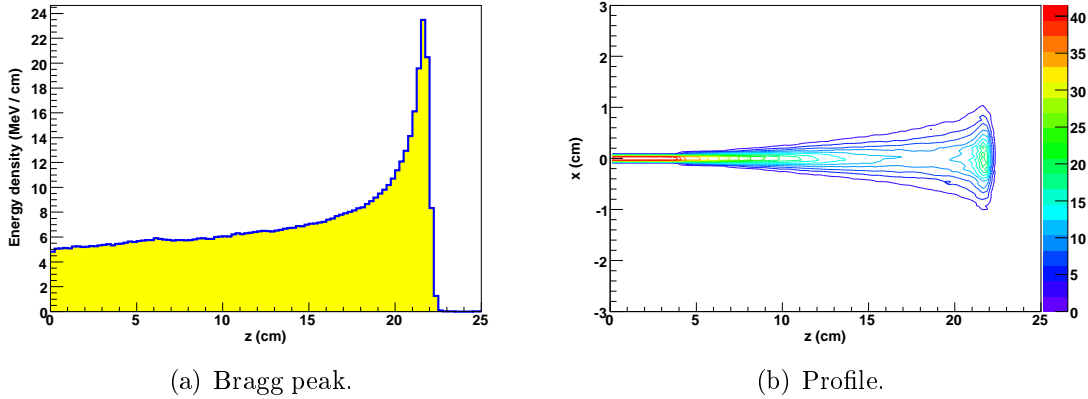


Figure 4.3: Energy density deposited by a 180 MeV proton in water: (a) Projection onto the direction of the proton shows dense energy deposition at the end of the track (Bragg peak), and (b) projection onto a plane containing the proton path (colour scale in MeV/cm^2).

which is rotationally symmetric around the beam axis, this energy is spread over a large volume, since scattering angles become larger⁷ in the lower energy part of the track. Thus, the energy density is highest in the first 5 cm of the track. We store the complete 3-D energy information in a histogram with $50 \times 50 \times 50$ bins.

Also, we used GEANT4 to study the influence of the 1.2 m of air and the 2 mm plastic foil which the protons have to traverse after leaving the beam line, and before entering the water. We found that these factors can be completely neglected. Further, we compared the results to the former gold standard simulation code Geant 3.21 and found excellent agreement.

The simulated energy deposition from a single proton is used to calculate the energy deposited by a proton bunch delivered from the accelerator. We assume, that there is no interaction between the protons within a bunch, and thus get the total energy deposition as a convolution between the single proton deposition and the proton flux in the bunch. A typical bunch used for this experiment is shown in Fig. 4.4.

The bunch width is variable, and typically a width of 2 cm FWHM was used. The temporal distribution of the protons is fixed by the accelerator and can be described as a Gaussian with $24 \mu\text{s}$ FWHM. The convolution leads to a set of 50 histograms $h(t_i)$ of $50 \times 50 \times 50$ bins, one for each time slice t_i . Each histogram contains the energy deposited in time slice i . Since all energy dissipation mechanisms are much slower than the energy deposition, the total energy deposited until time t_i can be

⁷The transversal momentum gained in each scattering process is fairly constant, but the longitudinal momentum of the proton decreases with energy, which leads to increasing scattering angles.

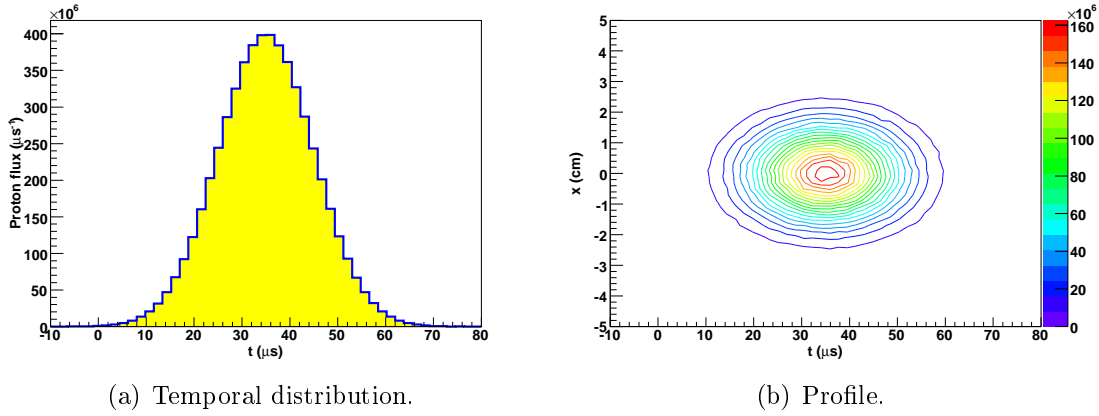


Figure 4.4: Profile of the bunch of $\approx 10^{10}$ protons (bunch energy 1.8 EeV) delivered by the cyclotron: (a) Temporal distribution of the protons and (b) profile of the proton bunch.

calculated as the sum over all histograms $\varepsilon(t_i) = \sum_{j \leq i} h(t_j)$.

Compared to the expected length of the pressure pulse of a few $10 \mu\text{s}$ the energy deposition of the proton bunch over $24 \mu\text{s}$ cannot be assumed instantaneous, and the full equation (4.2) has to be used to calculate the thermoacoustic signal. It is solved using a discrete version of (4.2) where the integration is replaced by a sum over histogram bins, and the time derivative is calculated as difference between histograms of the set at different times divided by the time step. Figure 4.5 shows the resulting pressure field.

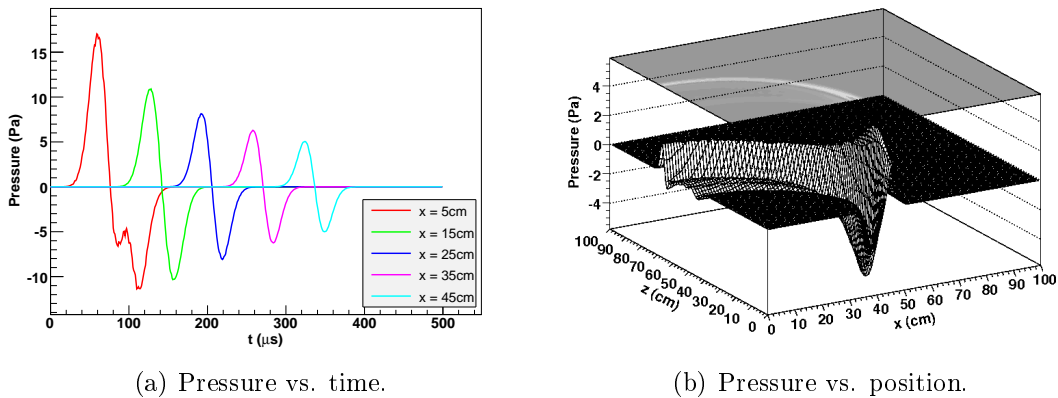


Figure 4.5: Simulated pressure pulses produced by the proton beam: (a) Pressure as a function of time for different distances x perpendicular to the proton beam (z fixed at 12 cm), and (b) pressure versus position at $t = 333 \mu\text{s}$ (the proton bunch starts to enter into the water at $t_0 = 0$ in positive z direction).

The bipolar acoustic pulse at different distances perpendicular to the proton beam can be seen in Fig. 4.5(a). The pressure field at a fixed time is shown in Fig. 4.5(b), where it is clearly visible, that the signal is highest perpendicular to the beam, leading to the expected disc shaped signature. The ringing of the signal which can be seen in Fig. 4.5(a) in the curve for $x = 5$ cm and in Fig. 4.5(b) is a near field effect caused by the different characteristic of different parts of the energy distribution. In contrast to a ultra high energy particle shower, which is a true line source as we will see, the proton beam signal is a superposition of a line source with the highest energy density in the first few centimetres of the track and a point source constituted by the Bragg peak.

We studied the contribution of the different parts by calculating the signal emitted from different regions of the energy deposition separately. The regions were chosen such that approximately the same total amount of energy is deposited in each of them. The investigated regions are $z < 10$ cm, $10 \text{ cm} \leq z < 20$ cm, and $z \geq 20$ cm. The contribution of these parts of the energy deposition to the signal can be seen in Fig. 4.6 showing the resulting acoustic pulses at different positions.

It can be seen that in the near field for small z the ringing comes from the later arriving signal of the Bragg peak, and for larger z it is determined by the late arriving signal from the line like part. In the far field all the signal contributions start to add coherently. This behaviour was also observed in the measured signals.

Results

For the analysis, signals averaged over 1000 proton bunches were used to suppress noise. Figure 4.7 shows a typical measured acoustic signal compared to the simulation (The simulated signal is rescaled to fit the amplitude of the measured signal).

The measured signal still includes the response of the hydrophone, nonetheless the bipolar structure is clearly visible, and the signal length matches the expectation. Thus, measured and simulated signals match reasonably well.

The plateau at the beginning of the measured signal, which is not of acoustic origin – the travel time of an acoustic signal for the 10 cm distance to the hydrophone is $67 \mu\text{s}$ – can be explained by a flow of charge from the proton bunch into the measurement system [44], since it has a fixed shape but its height is proportional to the proton bunch energy. The broadening of the first minimum as well as the ringing of the signal can be explained by a very early reflection of the signal at the proton beam entrance window into the tank, and by the response function of the hydrophone.

Further we could show [44], that in complete agreement with our expectations, the time of the first maximum of the signal is proportional to the distance of the hydrophone perpendicular to the proton tracks, and that the signal amplitude is proportional to the total bunch energy, whereas the signal length is energy independent.

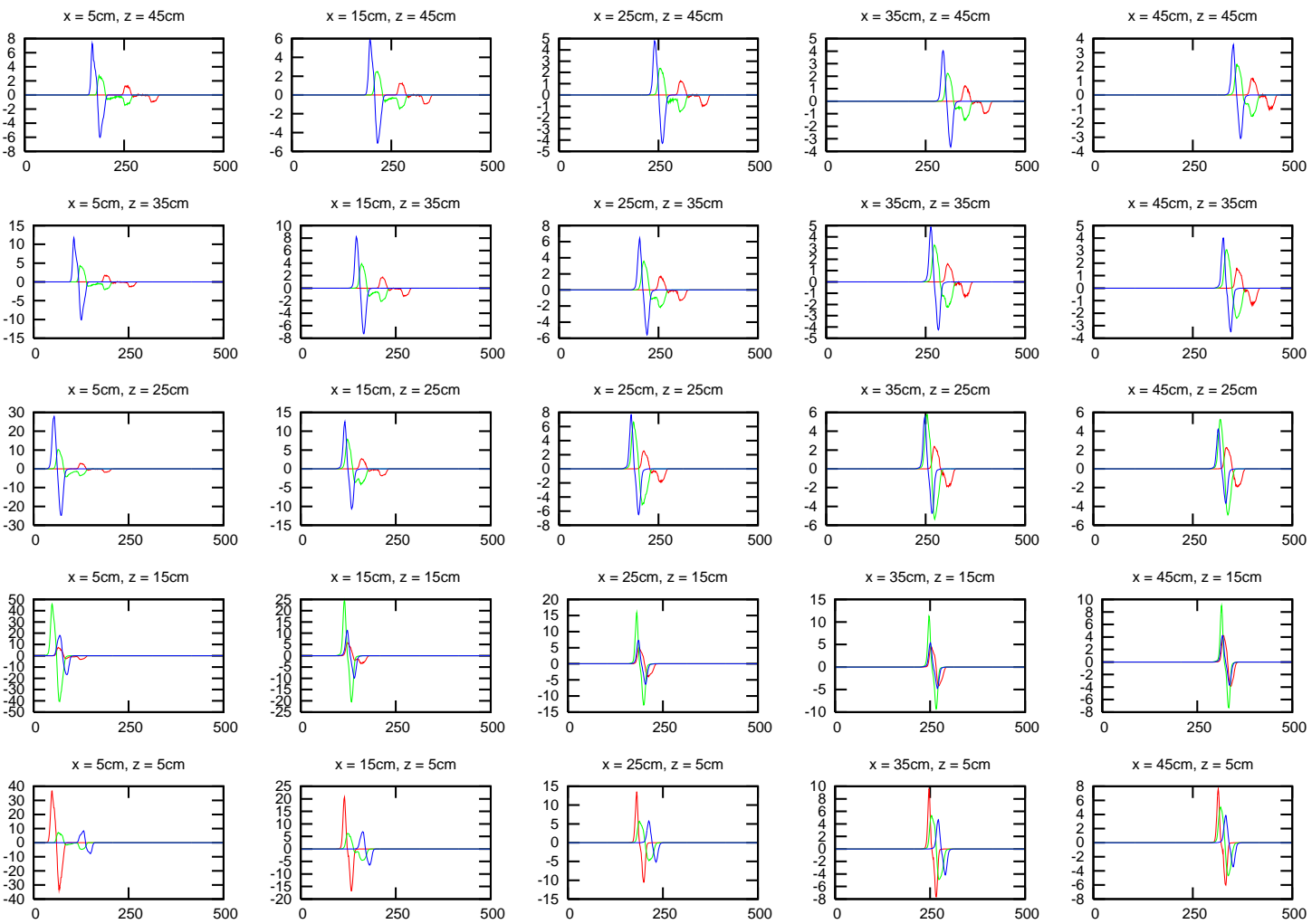


Figure 4.6: Contribution of different parts of the energy distribution to the acoustic signal. Red curves: $z < 10$ cm; green curves $10 \text{ cm} \leq z < 20$ cm; blue curves $z \geq 20$ cm (for each plot the abscissa is time in μs ; the ordinate is pressure in Pa).

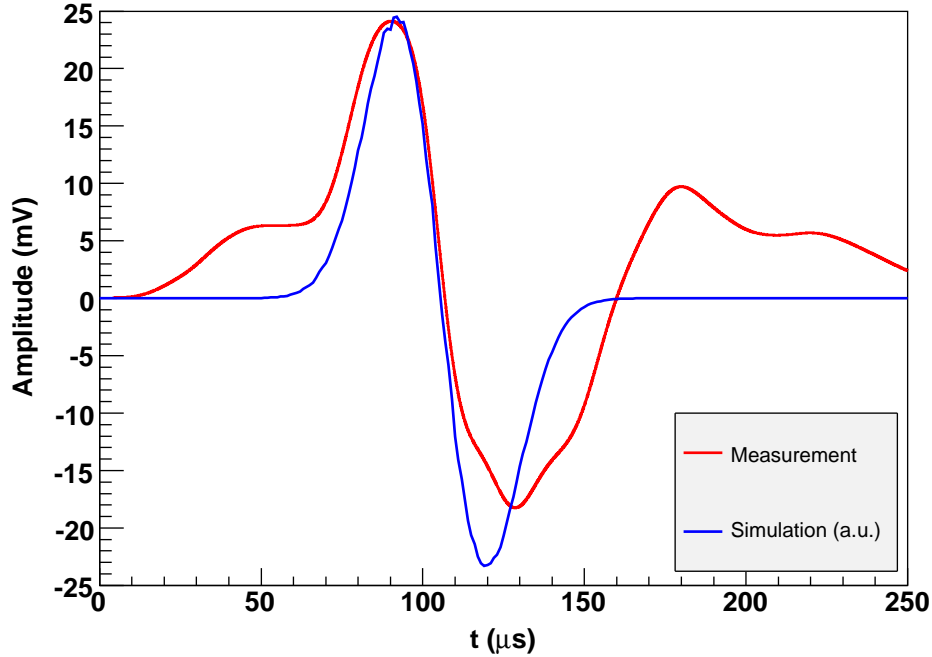


Figure 4.7: Comparison of measured and simulated signal at $x = 10$ cm and $z = 12$ cm. The bunch parameters are as in Fig. 4.4; the simulated signal is rescaled to fit the amplitude of the measured signal.

We determined the signal speed to be (1458 ± 4) m/s which is in excellent agreement with the textbook value for the speed of sound in fresh water ((1455 ± 1) m/s at the temperature considered).

An interesting feature to test the thermoacoustic model is the distance behaviour of the signal amplitude p_{\max} . The model predicts a disc-shaped signal where the symmetry axis is given by the line like energy deposition. Thus, in the near field region – compared to the size of the energy deposition region – we expect that the amplitude decreases as $1/\sqrt{r}$, where r is the distance perpendicular to the axis. In the far field region, where the energy deposition region can be assumed as point-like, the amplitude should decrease like $1/r$. For the proton beam experiment the transition region between near and far field lies within the water tank. Figure 4.8 shows the signal amplitude p_{\max} as a function of r for the simulation and the measurement.

The transition between the near field region and the far field region at $r \approx 26$ cm is clearly visible. The observed slopes agree well with the simple model prediction of a line like source in the near field, and a point source in the far field.

Further, we studied the dependence of the signal on the water temperature. A water temperature which is homogeneous over the whole tank was achieved by

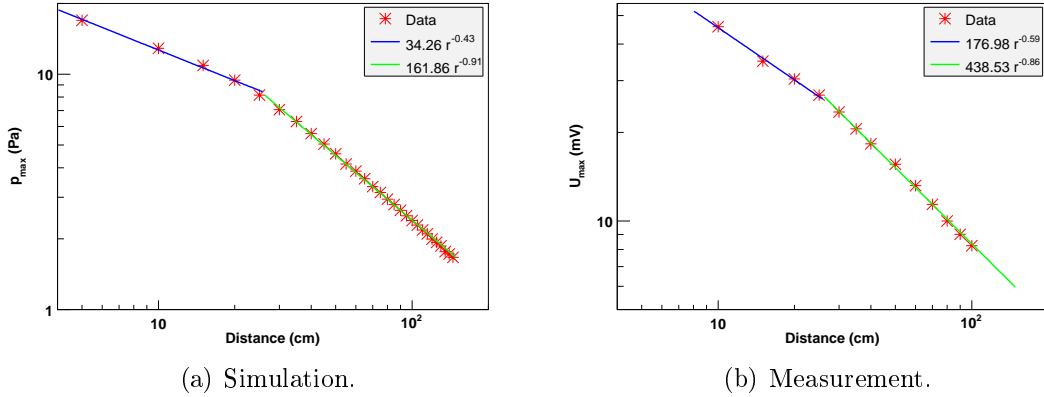


Figure 4.8: Dependency of the signal amplitude on the distance perpendicular to the proton beam ($z = 12$ cm). The solid lines are fit curves to the data. The transition between near and far field at $r \approx 26$ cm is clearly visible.

cooling the whole water volume and subsequent controlled reheating. Temperatures between 1°C and 15°C were set up with a precision of 0.1°C .

It was observed that, as expected, the pressure pulse is inverted at 4°C where the bulk expansion coefficient α changes its sign. Below 4°C heating of the water leads to a contraction, which propagates as an inverted bipolar pressure pulse from the energy deposition region. However, we found that the signal never vanishes completely as one would expect from the thermoacoustic model. At 4°C , there is a residual signal of the order of 1 mV (cf. scale in Fig. 4.7), which is obviously not of thermoacoustic origin. The exact nature of this residual signal is unclear, but the laser beam experiment (cf. Sec. 4.2.2) suggests, that it is a feature specific to the proton beam.

For the analysis of the data we subtracted the residual signal from all signals for the different temperatures. The resulting amplitude temperature relation is shown in Fig. 4.9.

Inverted signals below 4°C , where an increase of the temperature leads to a contraction of the water, are defined to have negative amplitudes. The measured values are in good agreement with the predictions from material properties represented by γ as defined in (4.5) and shown in Fig. 4.1.

Summarising, we could verify the thermoacoustic model with high accuracy. We showed that a rapid, line like energy deposition in a medium leads to a bipolar pressure pulse which mainly propagates perpendicular to the energy deposition region. The acoustic nature of the measured pulses could be proven by the determination of their velocity which is compatible with the speed of sound. The pulse variation with temperature is as expected from the model.

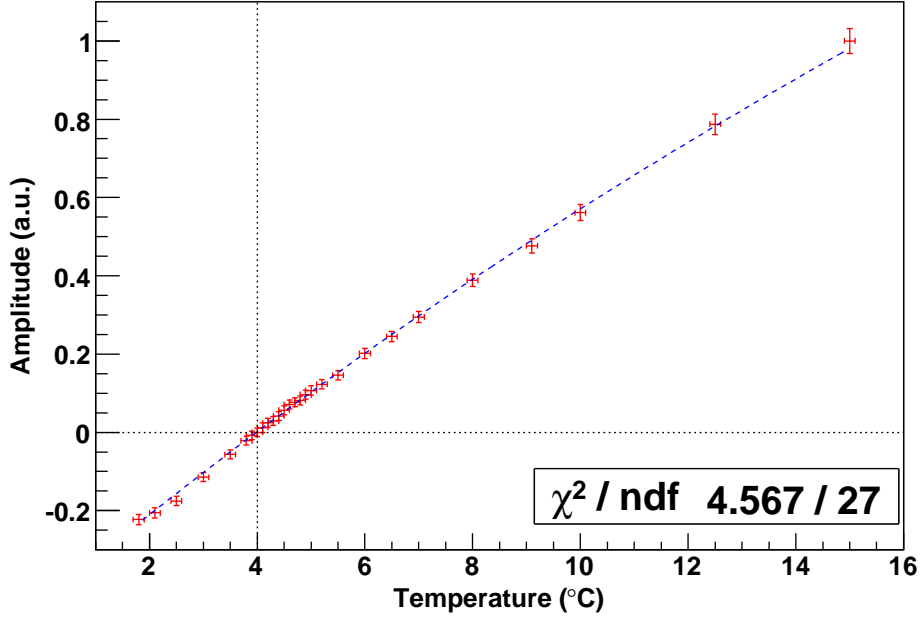


Figure 4.9: Amplitude of the proton beam signal at $x = 10$ cm and $z = 12$ cm as a function of the water temperature after subtraction of the residual signal at 4°C from all signals. The amplitude is normalised to unity at 15°C . The blue curve shows the γ factor from Fig. 4.1 fitted with an overall scaling factor.

4.2.2 The laser experiment

In order to address some questions left unanswered by the proton beam experiment presented in the previous section, especially the question for the nature of the residual signal observed at 4°C , we performed acoustic measurements with a laser beam dumped in water [47].

We used the same experimental setup as for the proton beam experiment which is shown in Fig. 4.2, only the beam entrance window was replaced by silica glass. An infrared, pulsed Nd:YAG laser with a wavelength of 1064 nm, a maximum pulse energy of 15 EeV, and a beam diameter of 1 cm is induced into the water, and the resulting bipolar pressure pulses are recorded by the position adjustable hydrophones. Since the laser has an absorption length of 7 cm in water, the tank is large enough that the laser beam is completely absorbed.

The main differences to the proton beam experiment are as follows:

- **Pulse length.** The laser we used can produce pulses with a length between 6 ns and 8 ns compared to the $24 \mu\text{s}$ bunch length of the proton pulse. Thus, for the laser beam an instantaneous energy deposition can be assumed which is comparable to the particle cascades induced by ultra high energy neutrinos,

and the time structure of the resulting acoustic signal is determined by the spatial extension of the energy deposition, and not by the bunch length as it was the case for the proton beam⁸.

- **Energy deposition mechanism.** The infrared laser beam is absorbed in water by exciting rotational and vibrational modes of the water molecules, whereas the protons transfer their energy to the water by ionisation and proton nucleus scattering. These completely different energy transfer mechanisms allow us to distinguish between thermoacoustic signals and contributions characteristic for the particular process of energy transfer, like the non acoustic plateau observed in the proton beam signals, which cannot be reproduced at the laser beam, and might thus well be an effect related to the transfer of electric charge.
- **Availability.** The availability of the laser setup in our laboratory in Erlangen allows us to repeat measurements at any time and to scrutinise effects which are not completely understood, being independent of the availability of an accelerator.

The simulation of the acoustic signals is done with the same methods as discussed for the proton beam experiment. The energy density deposited by the laser beam can be parameterised as a Gauss function with a width of 1 cm perpendicular to the axis, and has an exponential decay in the direction of the beam characterised by the absorption length of 7.1 cm. In contrast to the proton beam experiment the energy deposition can be assumed as instantaneous, and thus (4.4) can be used for the calculation of the signals.

We explored the dependence of the thermoacoustic signal on the sensor position and on the pulse energy, which are all in good agreement with the expectations from the simulations based on the thermoacoustic model [47]. Figure 4.10 shows signals measured at different temperatures around 4°C.

The first thing to notice is that the initial bipolar signal, which is followed by ringing in the hydrophone, has a length of approximately 30 μ s, and is much shorter than the proton beam induced signal which has a length of about 100 μ s. The reason is, as was previously discussed, that with an instantaneous energy deposition the signal length is defined by the extension of the energy deposition region, which is about 10 cm in length only. Further the signal vanishes completely at about 3.9°C. This supports the assumption, that the residual signal observed in the proton beam experiment is specific to this energy deposition mechanism, and that it is valid to

⁸With an instantaneous energy deposition mechanism, the resulting pressure pulse is a superposition of spheric waves emitted *simultaneously* from the whole deposition region; for the case of an energy deposition over a time window the acoustic signal is a superposition of spheric waves emitted in an interval of space and time.

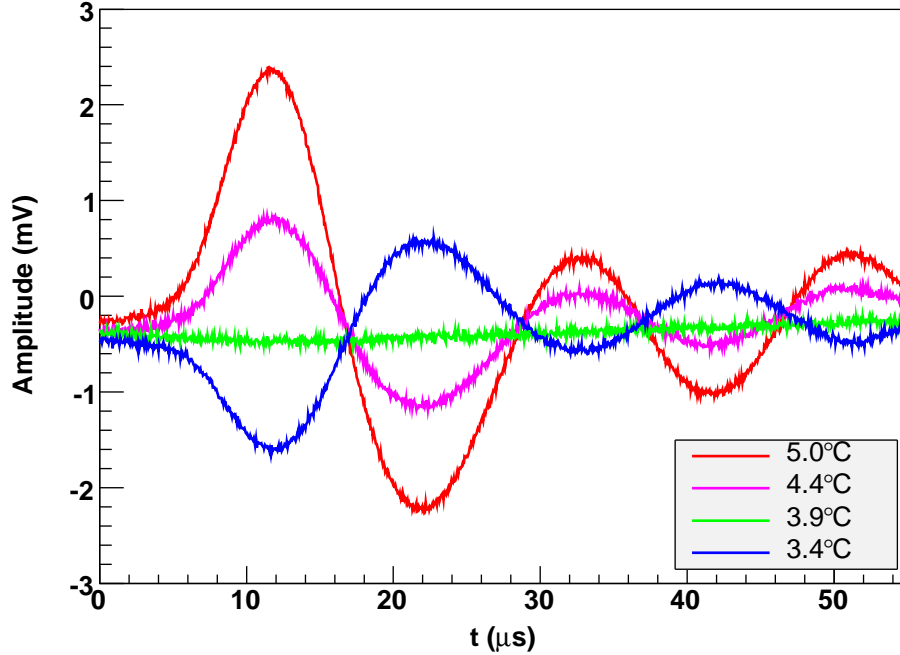


Figure 4.10: Laser induced pressure pulses measured at $x = 10$ cm and $z = 12$ cm at different water temperatures. The signal vanishes completely at 3.9°C , and changes its polarity below this temperature.

subtract this residual signal for the evaluation of the thermoacoustic model. The dependence of the pulse amplitude on the temperature is shown in Fig. 4.11.

The fit of the expected amplitude behaviour proportional to the γ factor (4.5), where an overall scaling factor and a temperature offset are left as free parameters, yields a zero crossing of the signal at $(3.85 \pm 0.06_{\text{stat.}} \pm 0.1_{\text{sys.}})^\circ\text{C}$, which is in excellent agreement with predictions based on the thermoacoustic model.

Since we have shown the validity of the thermoacoustic model, and that it is possible to simulate pressure pulses for a given energy deposition, we will continue in the next chapter with the investigation of acoustic pulses produced by neutrino induced particle cascades.

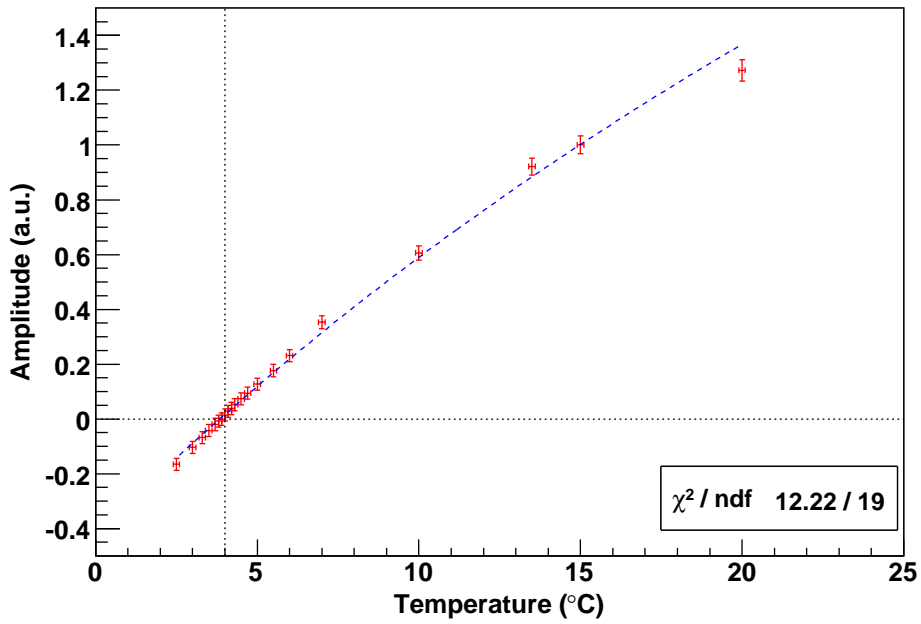


Figure 4.11: Amplitude of the laser induced signal at $x = 10$ cm and $z = 12$ cm as a function of the water temperature. The amplitude is normalised to unity at 15°C . The blue curve shows the γ factor from Fig. 4.1 fitted with an overall scaling factor and a temperature offset. The fit yields a zero crossing of the signal at 3.85°C .

Chapter 5

Acoustic signals from ultra high energy neutrinos

Contents

5.1	Propagation and interaction of ultra high energy neutrinos	41
5.2	Hadronic cascades	45
5.3	Electromagnetic cascades and the LPM effect	47

After we have shown the validity of the thermoacoustic model in the previous chapter and have established methods to calculate pressure signals produced by charged particles propagating through water, we will now discuss the production of acoustic signals by ultra high energy neutrinos. First we will review the propagation of the neutrinos to, and their interaction in the detector. Then we will investigate acoustic signals produced by ultra high energy hadronic and leptonic cascades induced by the neutrino.

5.1 Propagation and interaction of ultra high energy neutrinos

In the introduction to this work we stated that neutrinos are the ideal messengers from cosmological sources since, as only weakly interacting particles, they arrive at the Earth unperturbed. Further we pointed out that Water-Čerenkov neutrino telescopes are built to look downwards to use the Earth as a shielding for everything except neutrinos. These statements remain only partially valid when looking at neutrinos at highest energies. It is still true that these neutrinos can travel unperturbed through the void of the universe, but, since their cross section for interactions with nucleons increases with energy, already the Earth constitutes enough matter to completely shield neutrinos.

In this work we use the neutrino nucleon total cross section from [48]:

$$\sigma_{\text{tot}} = 1.2 \cdot 10^{-32} \text{ cm}^2 \left(\frac{E_\nu}{10^9 \text{ GeV}} \right)^{0.4} \quad (5.1)$$

Equation 5.1 is valid for $E_\nu \gtrsim 10^4 \text{ GeV}$, where E_ν is the energy of the incident neutrino in the rest frame of the nucleon. It is derived by extrapolating measured cross sections to higher energies under the assumption that the quark density in the nucleon follows a negative power law when going to smaller values of Bjorken x^1 . Further, (5.1) neglects the Glashow resonance at $6.7 \cdot 10^6 \text{ GeV}$, which describes the resonant production of W^- gauge bosons by electron anti-neutrinos interacting with electrons in the Earth. This resonance is narrow (width $\Gamma \approx 2.5 \cdot 10^5 \text{ GeV}$) and, as will be discussed later, at an energy well below the energies relevant for this work. Thus its neglect is well acceptable.

Using this cross section we can now calculate the mean free path L of neutrinos traversing the Earth,

$$L = \frac{m_n}{\rho \sigma_{\text{tot}}} \quad (5.2)$$

where m_n is the mass of the nucleon and $\rho = 5.52 \text{ g/cm}^3$ is the mean density of the Earth. Figure 5.1 shows L in Earth radii R_E as a function of the neutrino energy. The energies where L is one Earth radius and where L is one tenth of the Earth radius, and thus the energy range where the Earth becomes opaque to neutrinos, are indicated. Since we want to design a detector for neutrinos with energies $E_\nu \gtrsim 10^9 \text{ GeV}$ we will consider only neutrinos coming from above the horizon, i.e. with zenith angles $\theta < 90^\circ$.

On the other hand, if we consider an underwater neutrino telescope we have to ensure that the neutrinos can propagate freely through the water overburden down to the detector. Table 5.1 gives the mean free path of the neutrino in water ($\rho = 1.0 \text{ g/cm}^3$) and the zenith angle θ_{max} for which the neutrino path length is equal to the mean free path under the assumption that the ocean is flat and that the detector is at a depth of 2 km, a typical depth for existing neutrino telescopes.

Based on the presented data we will assume throughout this work for a first simulation of an acoustic neutrino telescope, that all neutrinos with $\theta < 90^\circ$ can propagate freely down to the detector, and that all neutrinos from below the horizon are absorbed inside the Earth².

¹The Bjorken x variable gives the momentum fraction of the quark in the nucleon. At higher energies the neutrino “sees” quarks with lower momentum, i.e. if the quark density is a negative power law function of x , it sees more quarks it can interact with, and the cross section rises accordingly.

²For an exact treatment of the neutrino propagation through the Earth one will especially have to take care of the tau neutrino since, in contrast to the muon which is stopped in the Earth, the tau lepton decays rapidly producing another high energy tau neutrino.

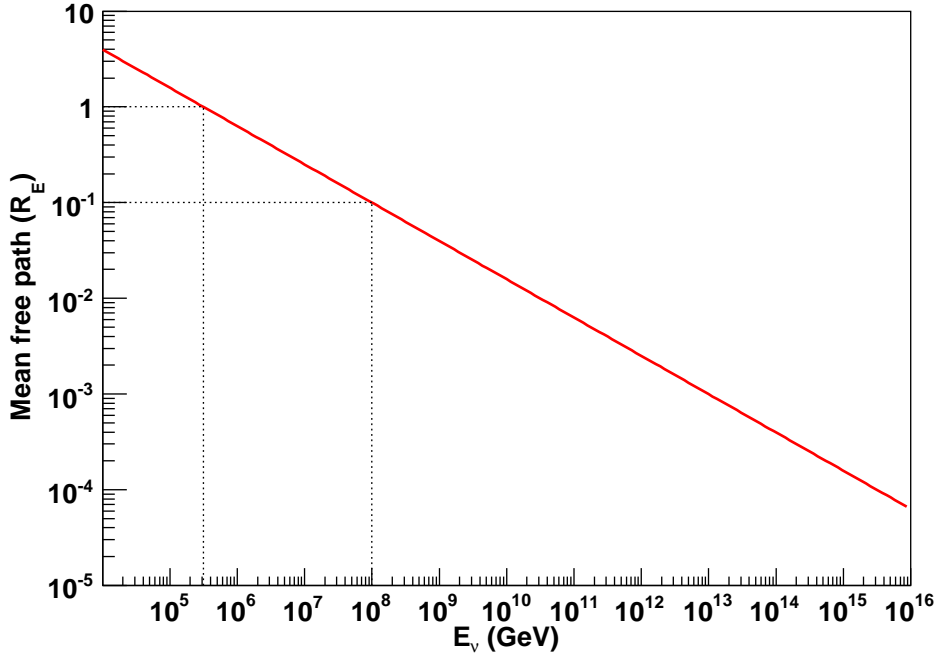


Figure 5.1: Mean free path length for neutrinos traversing the Earth in Earth radii. Indicated are the energies where the mean free path is one and one tenth of the Earth’s radius.

After the neutrino has reached the detector we need to study the neutrino interaction with a nucleon in the water. In this weak interaction an outgoing charged lepton (charged current interaction, CC) or an outgoing neutrino (neutral current interaction, NC) and a hadronic jet are produced. Here, as will become clear when we discuss the acoustic signals from hadronic and electromagnetic cascades in the following sections, it is especially interesting which fraction of the energy is transferred into these two channels.

We investigated this question by using the ANIS (All Neutrino Interaction Simulation) [49] simulation program. ANIS is an Open Source³ code written in C++ to simulate the propagation of ultra high energy neutrinos through the Earth to the detector and calculate the first interaction vertex in the detector. It can handle neutrino energies ranging from 10 GeV to 10^{12} GeV.

For our study we only investigated the kinematic parameter y which describes the energy transfer from the neutrino to the hadronic system:

$$y = 1 - \frac{E_\ell}{E_\nu} \quad (5.3)$$

³<http://www.ifh.de/nuastro/anis/anis.html>

Table 5.1: Mean free path length L of neutrinos in water and zenith angle θ_{\max} for which the neutrino path length is equal to L assuming a flat ocean and a detector depth of 2 km.

E_ν (GeV)	L (km)	θ_{\max}
10^9	1390	89.9°
10^{10}	553	89.8°
10^{11}	220	89.5°
10^{12}	88	88.7°
10^{13}	35	86.7°
10^{14}	14	81.7°

where E_ℓ is the energy of the outgoing lepton in the rest frame of the nucleon. We studied the distribution of y as a function of the energy E_ν of the incident neutrino, and found that the distribution is energy independent. It is shown in Fig. 5.2.

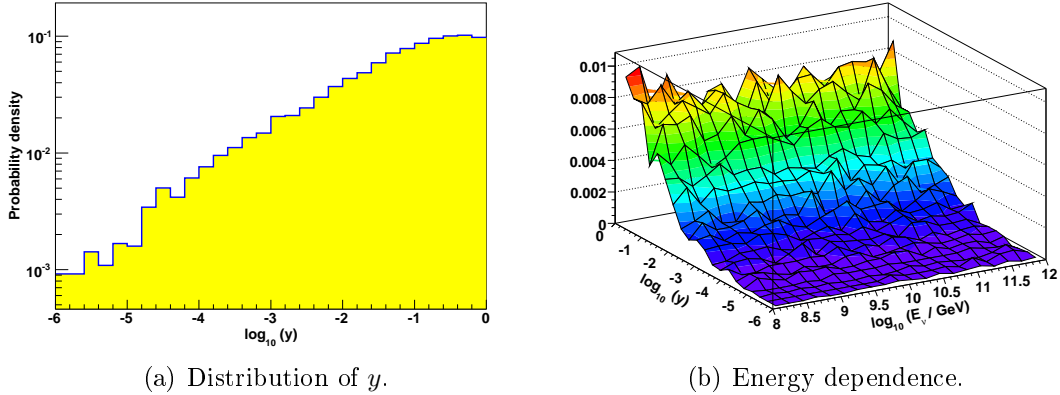


Figure 5.2: Distribution of the kinematic variable y which is the fraction of energy transferred in a neutrino nucleon interaction from the neutrino to the hadronic system in the rest frame of the nucleon. (a) shows the probability density function for $\log y$; (b) shows that this function is independent of the energy of the incident neutrino.

The energy independence can be seen in Fig. 5.2(b), and the resulting probability density function for $\log y$ is shown in Fig. 5.2(a). The median of this distribution is -1.1, i.e. in half of the neutrino interactions less than $10^{-1.1} = 8\%$ of the energy of the incident neutrino is transferred to the hadronic system.

5.2 Hadronic cascades

An ultra high energy hadronic jet produced in a neutrino interaction deposits its energy in a medium through subsequent strong interactions with the nuclei in the medium. Such hadronic cascades can be simulated with Monte Carlo packages. For example, GEANT4 can calculate hadronic cascades in water for primary energies up to 10^5 GeV.

The main problem in extrapolating shower simulations to higher energies is posed by the fact, that the development of particle cascades is governed by interactions with small transversal momentum p_T . But differential cross sections at small scattering angles, and thus small p_T , are not very well known since they are difficult to measure. Common particle detectors at accelerator experiments are designed cylindrically around the beam line to measure at high p_T . Their acceptance for small angles is naturally limited by the aperture of the beam line in the forward and backward directions. There are efforts⁴ to measure these low p_T cross sections at the LHC with “Roman Pots”: additional detectors far behind the interaction point and very near to the beam line.

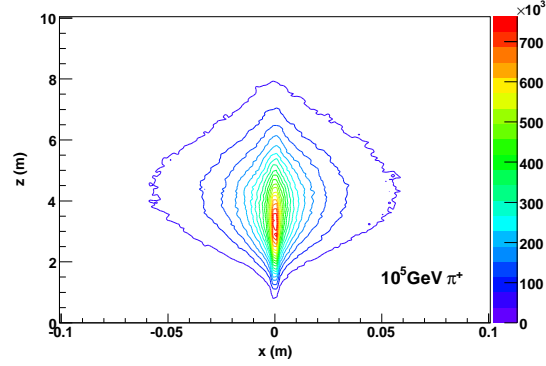
Due to this, we restrict ourselves to the simulation of showers with energies up to 10^5 GeV, and extrapolate the deposited energy density to higher primary energies. The profile of a typical hadronic cascade in water induced by a 10^5 GeV π^+ meson is shown in Figs. 5.3(a) and (b). The energy of the incident pion is deposited in a cylindrical volume with a length of about 5 m FWHM, and a diameter of approximately 2 cm FWHM. Systematic studies over two decades of energy from 10^3 GeV to 10^5 GeV, where GEANT4 delivers valid results, show that the *functional form* of the energy density is independent of the primary energy within about fifteen percent (cf. Figs. 5.3(b) and (c)). With increasing energy, the maximum of the longitudinal shower profile is at higher z values (deeper inside the medium). The shower length⁵ and the shower width slightly decrease with energy.

In this work we will assume, that for *all* energies the shape, i.e. the functional form, of the energy deposition density is given by Figs. 5.3(a) and (b), and that the magnitude of the histograms presented scales linearly with the energy of the hadronic system.

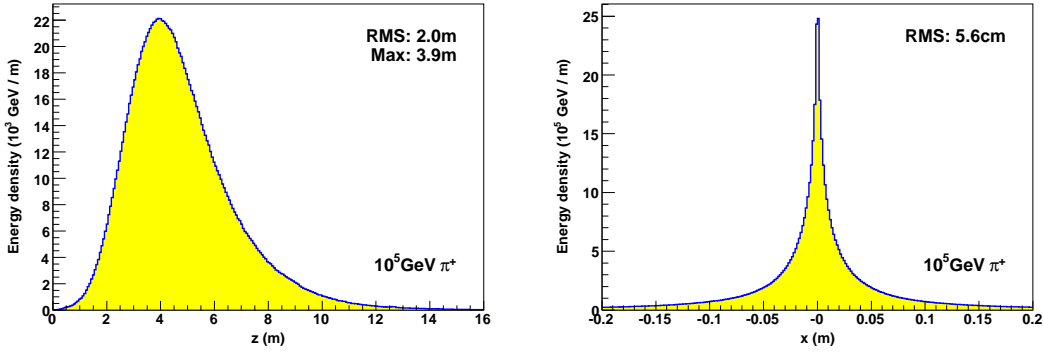
Using this energy deposition density we are now in a position to calculate acoustic pulses emitted from hadronic cascades. Since we look at cascades with ultra high energies, these cascades develop with the speed of light in vacuum and we can assume the energy deposition to be instantaneous and use (4.4) to determine the acoustic signal. A typical acoustic signal is shown in Fig. 5.4.

⁴see e.g. <http://totem.web.cern.ch/Totem/>

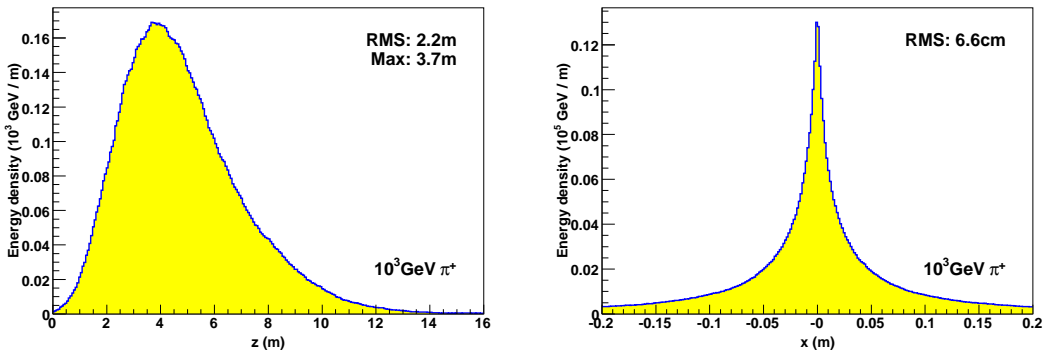
⁵The shower length is defined as the interval of the longitudinal projection of the energy density where 90% of the energy are deposited. It is calculated as the difference of the longitudinal coordinates below which 5% and 95% of the total energy are deposited respectively.



(a) 10^5 GeV π^+ energy distribution.



(b) 10^5 GeV π^+ longitudinal and transversal profile.



(c) 10^3 GeV π^+ longitudinal and transversal profile.

Figure 5.3: Energy density deposited by π^+ mesons in water. (a) projection onto a plane containing the direction of the incident pion; the colour scale gives the energy density in GeV / m^2 . (b) and (c) comparison of the energy density deposited by a 10^5 GeV and a 10^3 GeV π^+ respectively.

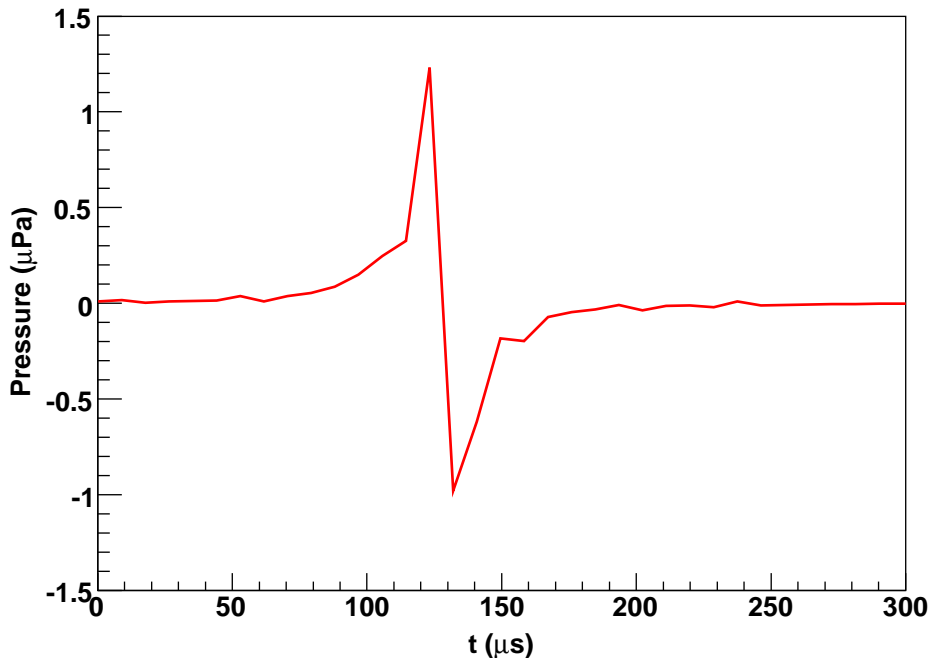


Figure 5.4: Bipolar acoustic signal produced by a 10^5 GeV π^+ meson in water calculated in a distance of 400 m from the shower centre perpendicular to the shower axis. The cascade was produced at time $t = -266.5$ ms, which corresponds to a sound travel path of 400 m.

It is calculated at a position 400 m away from the cascade centre perpendicular to its axis, the direction where the amplitude is expected to be highest. The rather coarse time resolution of the signal is caused by the bin width with which the energy deposition density of the cascade was recorded – a histogram with $250 \times 250 \times 250$ bins, which is already at the upper limit of what can be stored on common computers. However, we have confirmed that the maximum amplitude of the signal, which is the parameter important for the simulations of an acoustic neutrino telescope as presented in Chap. 7, is stable with respect to variations of the number of bins.

In the simulations resulting in Fig. 5.4 no absorption of the signal during the propagation through the water is included, yet. The properties of the signal, including the attenuation of sound in water will be discussed in detail in Chap. 6.

5.3 Electromagnetic cascades and the LPM effect

Electromagnetic cascades originate from high energy photons or electrons and develop in matter, above approximately 100 MeV, mainly through bremsstrahlung and

pair production. They solely consist of photons, electrons, and positrons, and thus show less variations than hadronic cascades. Further, their transversal extension is smaller than for hadronic showers, so that at a comparable shower length the energy density in an electromagnetic cascade is higher than in a hadronic cascade, and the acoustic signal produced has a higher amplitude.

Unfortunately, this is not true for electromagnetic showers at highest energies. It was first noted by Landau, Pomeranchuk [50, 51], and Migdal [52], that above some threshold energy the cross sections for bremsstrahlung and pair production would decrease rapidly with energy (*LPM effect*), which leads to strong elongation of the cascade, and a decrease of the energy density, and thus of the amplitude of the acoustic pulse.

Usually the cross sections for bremsstrahlung and pair production are calculated by assuming momentum transfer to a single scattering centre (i.e. nucleus in the medium). At ultra high energies, there arise destructive quantum mechanical interferences between amplitudes from different scattering centres [53], which reduce the cross sections. For the case of bremsstrahlung one can picture the photon as being emitted over a certain interaction length, which is set by the temporal length of the wave train and the path length the electron propagates during this time. If this interaction length becomes comparable to the inter-atom distance in the medium, screening effects and multiple scattering during the interaction start to play a significant role.

Detailed calculations in the framework of QED (e.g. [52]) result in the cross sections presented in Figs. 5.5 and 5.6. Differential cross sections for various electron and photon energies are shown, normalised to eliminate the material properties. The parameters and their values for water are as follows: Radiation length $X_0 = 36 \text{ g/cm}^2$, atomic mass $A = 18 \text{ g/mol}$, and Avogadro's number N_A , resulting in the following scaling factor for the cross section:

$$\frac{A}{X_0 N_A} = 8.3 \cdot 10^{-25} \text{ cm}^2$$

Obviously, the total cross sections decrease with an increasing energy of the incident particle or photon.

Simulations of electromagnetic cascades using the LPM cross sections yield the following results [54]:

- The shower length increases dramatically (between one and two orders of magnitude). Thus, assuming a constant shower width, the energy deposition region is increased, and the energy deposition density in the medium is reduced by the same factor. The resulting thermoacoustic signals, which scale linearly with the energy density, are strongly suppressed compared to signals from hadronic cascades with the same total energy. Simulations of acoustic signals from a 10^{11} GeV hadronic cascade and a 10^{11} GeV electromagnetic

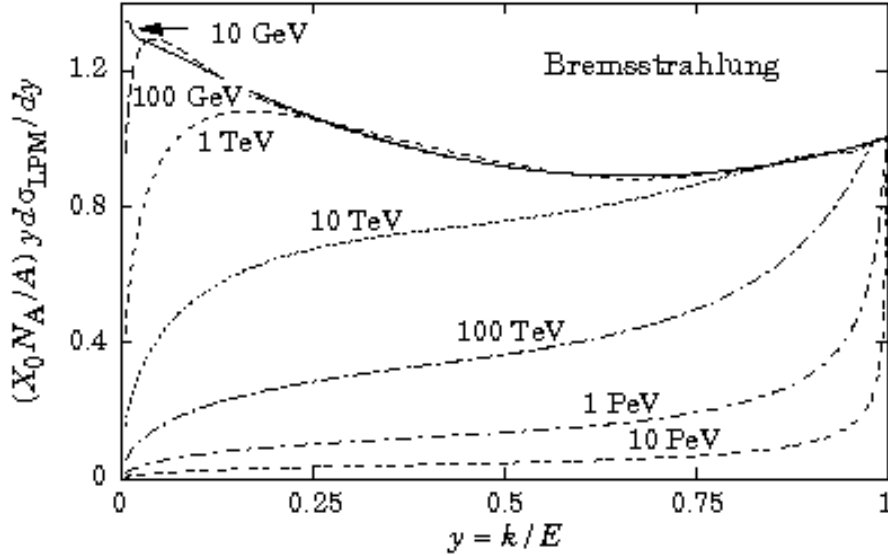


Figure 5.5: Normalised cross section for bremsstrahlung for different electron energies E . The energy of the emitted photon is denoted by k . The decrease of the total cross section, which is given by the area under the corresponding curves, with increasing energy is clearly visible (from [53]).

LPM cascade have shown, that the amplitude of the acoustic signal from the hadronic cascade has five times the amplitude of the pulse produced by the electromagnetic cascade [37].

- LPM cascades show large variations, since they develop sub-showers at various distances along the cascades when particles from the main shower drop below the LPM threshold energy. Thus a parameterisation of LPM cascades is impossible, and a simulation on an event-by-event basis is necessary.

In summary, we get the following conditions for the simulation of acoustic signals in an acoustic neutrino telescope: Even if generally electromagnetic cascades are easier to treat numerically since they are dominated by two types of interactions only, bremsstrahlung and pair production, this is not longer true at highest energies due to the LPM effect. There are simulation codes to assess the longitudinal profile of LPM showers⁶ also in water, but no fully 3-D simulation is known to the author. But this full 3-D energy profile is required to scrutinise the acoustic signal produced by such a cascade since the signal is very sensitive to the transversal energy profile. Although we have shown in Sec. 5.1 that on average about 80% of the

⁶These simulation codes are mostly developed by EAS experiments like Pierre Auger looking at the fluorescence light from air showers. The output of fluorescence light can completely be determined from the longitudinal profile, since, due to the much shorter wavelengths involved, there is no interference expected from contributions in the transversal shower extension.

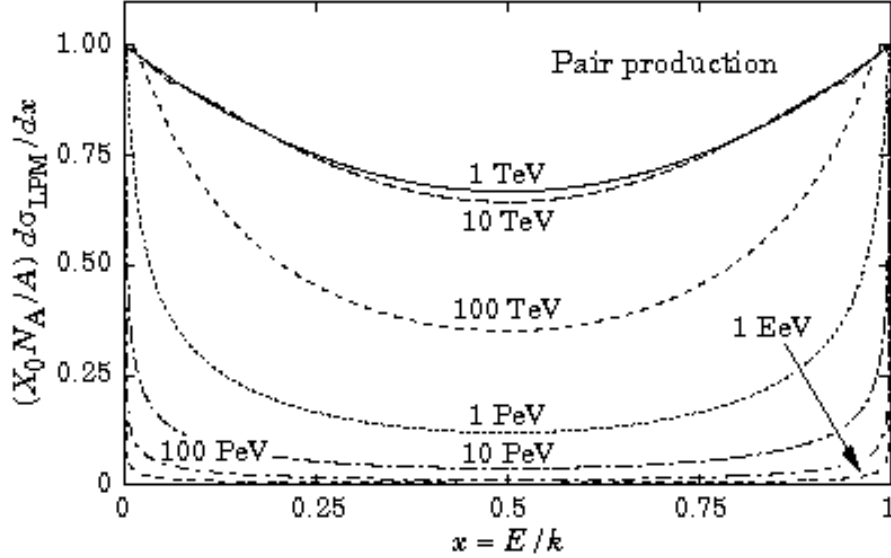


Figure 5.6: Normalised cross section for pair production for different photon energies k . The energy of the emitted electron (or positron) is denoted by E . The decrease of the total cross section with energy is again clearly visible (from [53]).

neutrino energy is transferred into the electromagnetic cascade, estimations of the acoustic signals [37] predict that, for equal energies, the pressure amplitude from the electromagnetic cascade is only about 20% of the amplitude of the hadronic cascade. Thus, we expect for ultra high energy neutrino interactions on average pressure amplitudes of the same order of magnitude from the electromagnetic and the hadronic cascade.

Since in the case of ultra high energies, hadronic cascades are expected to show less variations than electromagnetic LPM showers, we decided to completely neglect electromagnetic cascades in our study, and only utilise the acoustic signals emitted from the hadronic shower. So all limits derived for the diffuse neutrino flux are solid upper limits and should be improved by the inclusion of the electromagnetic cascades into the study.

Chapter 6

Sound propagation and detection in water

Contents

6.1	Attenuation in fresh water and sea water	51
6.2	Refraction and Reflection	54
6.3	Background noise and signal extraction	57
6.3.1	Properties of the background noise	57
6.3.2	Filtering in the time domain	59
6.3.3	Filtering in the frequency domain	60
6.4	Parameterisation of the acoustic signal	60

In this chapter we discuss the propagation of the acoustic signal from the cascade to the sensors and develop a parameterisation of the signal amplitude for any sensor position. Possibilities to extract the signal out of the background noise are discussed and sensitivity estimates for single sensors are presented.

6.1 Attenuation in fresh water and sea water

The main cause for the degradation of the acoustic signal between the place of production at the hadronic cascade and a sensor is attenuation. There are two types of attenuation which have to be taken into account.

The first type is due to dispersion of the signal during propagation and has already been discussed for the proton beam experiment (cf. Fig. 4.8) where we have shown that in the near field – compared to the extension of the cascade producing the signal – the pressure field has a disc-like shape around the shower axis, and the pressure amplitude thus decreases like $1/\sqrt{r}$ when r is the distance from the cascade. In the far field the cascade can be assumed as a point source, and the signal amplitude drops like $1/r$.

The second type of attenuation, which has to be accounted for, is the absorption in the water, which is strongly frequency dependent and very different for fresh water and sea water. Figure 6.1 shows the absorption length for both media as a function of frequency. The absorption length is defined as the distance after which the *energy* in the acoustic wave has decreased by a factor $1/e$, i.e. the pressure amplitude has dropped by a factor $1/\sqrt{e}$.

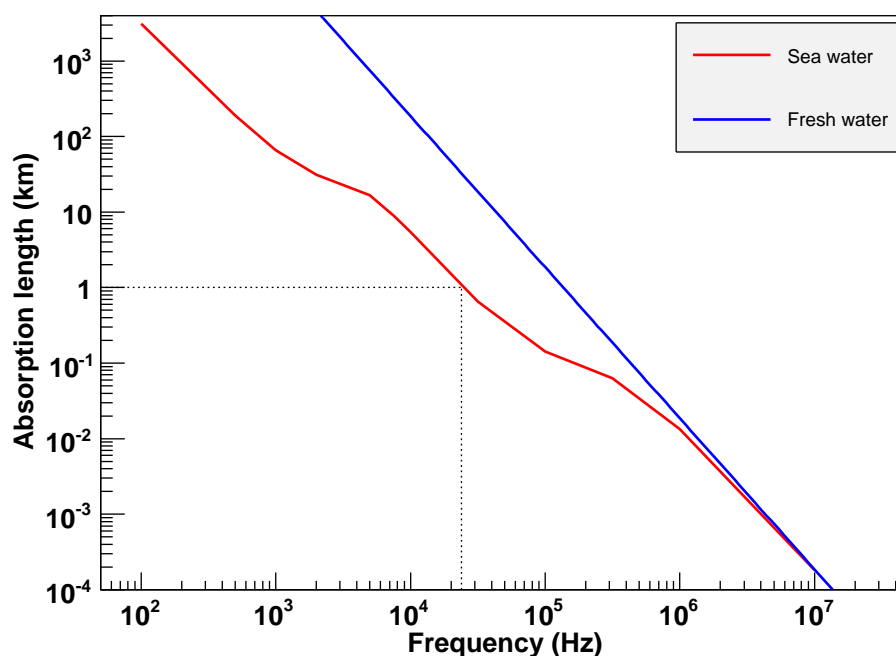


Figure 6.1: Sonic absorption length in sea water and fresh water as a function of frequency (data from [55]).

In fresh water the absorption is due to the viscosity of the water, which means that energy is transferred from the sonic wave into the water when the water molecules are displaced against each other under the inhomogeneously changing pressure. Let $\mu = 0.01$ P be the viscosity of the water¹. Then the absorption length L is given by [55]:

$$L = \frac{10}{\ln 10} \frac{3\rho c^3}{16\pi^2\mu} \frac{1}{f^2} \quad (6.1)$$

where ρ is the density of the water, c is the speed of sound, and f is the frequency of the acoustic signal.

¹The SI unit for viscosity is the Poise, named after J.L. Poiseuille (1799 - 1869): 1 P = 1 Ns/m².

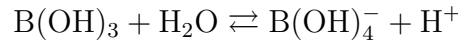
For frequencies above 1 MHz the absorption in fresh water and sea water are nearly the same. Below 1 MHz the absorption in sea water increases rapidly due to ionic relaxation processes. The decrease of the absorption length between about 5 kHz and 1 MHz, the range important for acoustic particle detection, is caused by MgSO_4 dissolved in the sea water (see [56] for a review of sound absorption due to ionic relaxation).

In the unperturbed sea there is an equilibrium between the molecular and the ionic system:



The equilibrium concentration of the components is pressure dependent, and a perturbation of the equilibrium state through the pressure of the acoustic wave leads to a dissociation of MgSO_4 molecules. The energy for this decomposition is deprived from the sonic wave. This energy is released only after some relaxation time τ mainly as thermal energy, thus degrading the acoustic signal. Although MgSO_4 amounts to only 4.7% of the weight of all salts dissolved in the sea [55], this effect causes the absorption length to decrease by a factor of 30 compared to fresh water in the frequency range considered.

Below 5 kHz, a frequency range of minor importance for acoustic neutrino detection, the sonic absorption length drops by about another factor of 10. This is caused by an ionic relaxation process involving boric acid



which is very complicated since the equilibrium state strongly depends on the pH and on other ions dissolved in the water [55].

At a frequency of about 20 kHz, which is the central frequency of the bipolar pressure pulse expected from a neutrino induced particle shower, the sonic absorption length in sea water is 1 km. This is about a factor of 15 larger than the absorption length of Čerenkov light which is around 60 m in both sea water [57] and ice [58]. This distance governs the spacing between the photomultiplier tubes in today's water Čerenkov neutrino telescopes (cf. Sec. 3.1). Thus, the inter-sensor spacing in an acoustic neutrino telescope could be larger by a factor of 10 than in an optical neutrino telescope, which allows to instrument much larger target masses with the same number of sensors.

We will use the presented attenuation of sound in water in Sec. 6.4 to develop a parameterisation of neutrino induced acoustic pulses for any sensor position, which is a prerequisite for the implementation of a simulation of an acoustic neutrino telescope.

6.2 Refraction and Reflection

Two other mechanisms leading to a degradation of an acoustic pulse propagating through the sea are refraction and reflection of the signal on the sea surface and bottom.

The refraction of the signal is caused by the fact, that the speed of sound in the sea is not constant, but varies slightly with depth. The sound velocity is a function of temperature and pressure. A typical deep sea sound velocity profile is shown in Fig. 6.2.

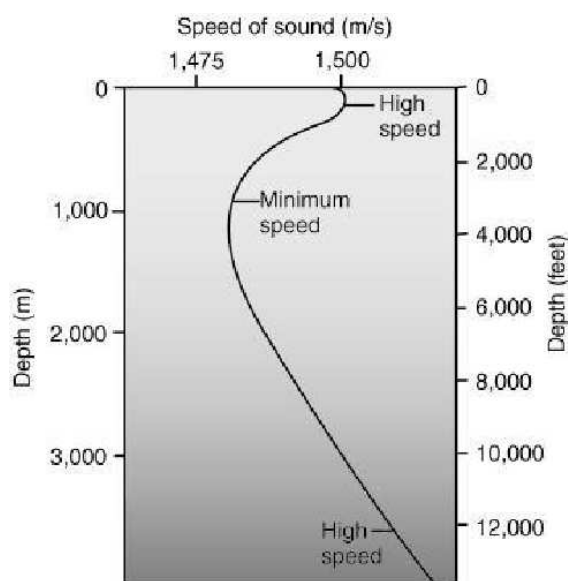


Figure 6.2: Typical deep sea sound velocity profile (<http://www.punaridge.org/>).

In the first few ten metres beneath the surface the sound velocity undergoes strong seasonal variations due to the varying water temperature. Below this, down to about 1000 m, the speed of sound decreases with the water temperature. Further below the temperature remains fairly constant and the sound velocity starts to increase again, following the water pressure linearly.

We will now show that a wave in a medium, in which its velocity changes linearly in one direction, propagates on a circular path [55]. We will use the geometry and the symbols defined in Fig. 6.3.

The sound velocity is supposed to increase linearly from top to bottom with some rate k so that $c_i = c_0 - kd_i$ ($k > 0$), where c_0 is the speed of sound at some reference depth where the “sonic ray” would be perpendicular to the velocity gradient (cf. Fig. 6.3). Let us consider a sonic ray at an arbitrary point $P1$ with an angle of incidence ϕ_1 which propagates to $P2$ where its incident angle is ϕ_2 . Then we know from the law of refraction that $n_i \sin \phi_i = n_i \cos \theta_i = \text{const.}$, where the index of

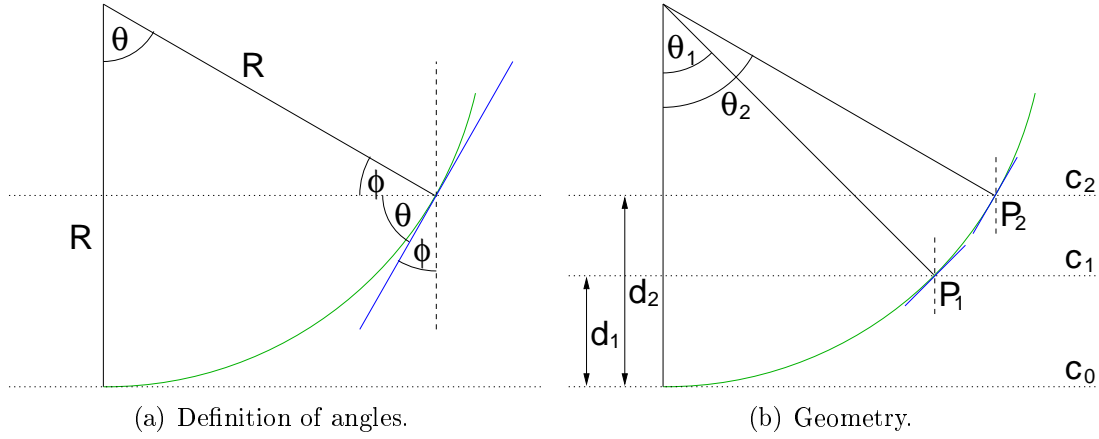


Figure 6.3: Refraction in a medium with a linear velocity gradient.

refraction n_i is proportional to the inverse of the wave velocity c_i :

$$\frac{1}{c_0} = \frac{\cos \theta_1}{c_1} = \frac{\cos \theta_2}{c_2}$$

Here, we have used our prerequisite that in the depth where $\theta = 0$ the speed of sound is c_0 . Thus, from the law of refraction follows:

$$c_1 - c_2 = c_0 \cos \theta_1 - c_0 \cos \theta_2 \quad (6.2)$$

From the definition of the gradient in the sound velocity we get:

$$c_1 - c_2 = -k(d_1 - d_2) \quad (6.3)$$

Combining (6.2) and (6.3) we get the following equation, where we have made no assumptions in the shape of the sonic ray, yet:

$$d_1 - d_2 = -\frac{c_0}{k} \cos \theta_1 + \frac{c_0}{k} \cos \theta_2 \quad (6.4)$$

If we now only consider the geometry as it is sketched in Fig. 6.3(b), which assumes a circular trajectory, we get:

$$R - d_i = R \cos \theta_i$$

or

$$d_1 - d_2 = -R \cos \theta_1 + R \cos \theta_2 \quad (6.5)$$

Since we have not made any assumptions about the points P_1 and P_2 we can deduce from comparing (6.4) and (6.5), where the first equation was derived only

from basic physics without making any assumptions on the trajectory, and the second equation was deduced from the geometry only, that all points a ray passes in a linear velocity gradient lie on a circle with radius $R = c_0/k$. For example for the Mediterranean Sea the velocity gradient $k = 16.5 \text{ ms}^{-1}/\text{km}$ [59], and thus the radius of the sonic rays is $R = 91 \text{ km}$.

This has a great impact on the design of an acoustic neutrino telescope. Let us assume a water depth of 2500 m, which is a typical value for the Mediterranean Sea, and a neutrino telescope built on the sea bed with an instrumented volume reaching 1 km above the sea floor. We define Δx as the horizontal distance a sonic ray, which is emitted horizontally near the bottom of the sea, has to travel to gain the vertical distance Δy :

$$\Delta x = \sqrt{R^2 - (R - \Delta y)^2} \quad (6.6)$$

Figure 6.4 shows that after a distance of 13.5 km a ray emitted horizontally at the sea floor will no longer pass a detector of 1 km height. Further it can be seen, that for distances greater than $2 \cdot 13.5 \text{ km}$ there practically do not exist any rays which will pass the detector. All rays emitted inside the volume indicated in red will be bent above the detector. This introduces a natural cutoff to the water volume observable with a single sensor².

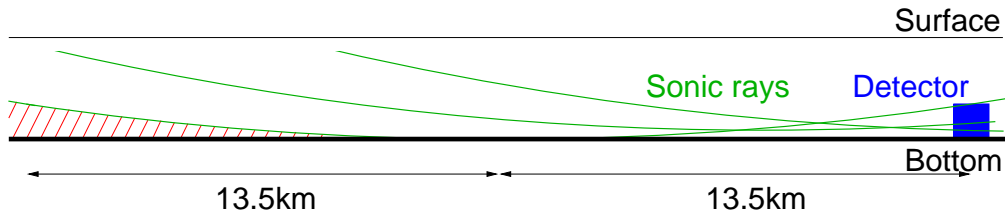


Figure 6.4: Geometrically accessible detection volume. The inaccessible volume is indicated in red.

For the simulation of an acoustic neutrino telescope, which we will present in Chap. 7, we will assume that the sound propagates on straight lines, since developing a dedicated ray-tracing algorithm³ is not part of this work. We introduce the effects of refraction into the simulation by assuming, that no acoustic signal from neutrino interactions taking place more than 27 km ($2 \cdot 13.5 \text{ km}$) away from

²Not taking this effect into account would allow to detect pressure pulses produced by highest energy neutrinos ($E_\nu \gtrsim 10^{14} \text{ GeV}$) from distances even greater than 500 km, i.e. from practically everywhere in the Mediterranean Sea.

³Detailed treatment of the sound propagation requires ray tracing, since the complicated sound velocity profile in the upper water layers leads to deviations from the circular path. Especially the minimum of the sound velocity below the surface leads to channelling of acoustic waves which is completely neglected in this work.

the instrumented volume can reach the detector. Further, we neglect any signals that are reflected at the sea surface or bottom. There is no information whether a neutrino induced bipolar acoustic pulse, which will be degraded when reflected at those uneven surfaces, can still be extracted from the background noise. By assuming straight line propagation, signals crossing the sea surface or bottom simply do not further contribute to the simulation. The influence of reflection on short acoustic pulses on rough surfaces will have to be investigated in a separate study.

By using straight line propagation, the zenith distribution of the signals reaching the detector is slightly changed towards vertically downward going neutrinos. In the straight line case mostly acoustic signals produced by vertical cascades will reach the detector, whereas in the case of refracted trajectories those signals will be bent above the detector. This is balanced by a contribution of inclined cascades, whose signals are absorbed at the bottom when assuming straight line propagation, and which will otherwise be refracted over the seabed and back into the detector. In this work we *assume* that for an isotropic neutrino flux from the upper hemisphere the total number of signals reaching the detector is equal for both cases.

6.3 Background noise and signal extraction

We will now discuss the acoustic background noise which is always present in the sea, and out of which a neutrino induced bipolar pressure pulse has to be extracted in an acoustic neutrino telescope.

6.3.1 Properties of the background noise

Acoustic noise in the sea has been studied extensively in the 20th century (cf. [60] for a review), mostly during World War II for the development and tracking down of submarines. The noise can be divided into three frequency bands:

- **below 200 Hz.** This frequency range, which is unimportant with respect to acoustic particle detection, is dominated by shipping and similar anthropogenic noise, and thus shows a high variability.
- **200 Hz to 50 kHz.** In this frequency band neutrino induced acoustic signals are expected. The noise in this band strongly depends on the wind speed at the sea surface, even for deep sea measurements. The main sources of noise are wind turbulence on the rough sea surface, the motion of the sea surface, interactions of surface waves travelling in different directions, and spray and cavitation, i.e. air bubbles trapped in the water near the surface [60].
- **above 50 kHz.** Here, the noise spectrum is dominated by thermal noise. It is caused by the thermal motion of the water molecules which collide with the sensor.

Typical deep sea acoustic noise spectra measured with the AUTECH hydrophone array [37] near the Bahamas at different wind speeds are shown in Fig. 6.5.

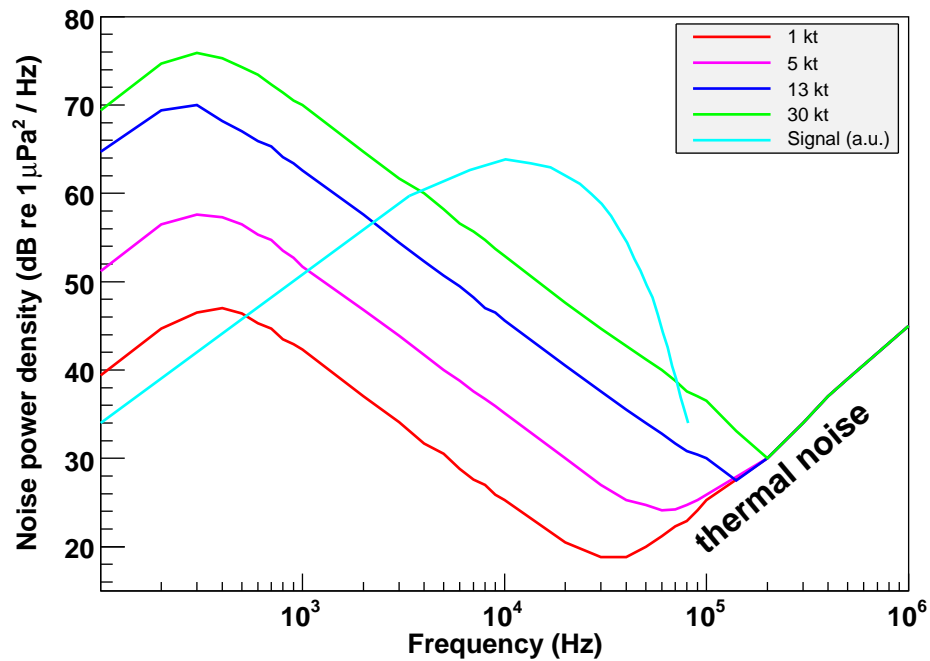


Figure 6.5: Acoustic noise power density in the sea for different wind speeds [37] (1 kt = 1.852 km/h). Imposed is the spectrum of the acoustic signal produced by a hadronic cascade at a distance of 1000 m perpendicular to the shower axis. The absolute amplitude of the signal spectrum depends on the cascade energy.

The wind noise has a maximum at around 300 Hz, and decreases for higher frequencies until the thermal noise, which increases linearly with frequency, starts to dominate the spectrum. This leads to a minimum in the noise spectrum between 30 kHz and 200 kHz, depending on the wind speed. Also shown is the shape of the frequency spectrum of a neutrino induced bipolar pressure pulse. The absolute amplitude of this spectrum depends, of course, on the energy of the particle cascade and its distance to the sensor. It is noteworthy, that the maximum of the signal spectrum at about 20 kHz falls into the decreasing part of the noise spectrum, and even close to its minimum for low wind speeds. This leads to an improved signal-to-noise ratio in an appropriate frequency band around 20 kHz, and thus increases the detectability of neutrino induced pressure pulses.

Table 6.1 gives the RMS values of the noise calculated from the presented spectra in different frequency bands, and also, as a rough guide, the cumulative probability w to find the indicated weather conditions.

Table 6.1: RMS of acoustic noise in the sea in mPa for different wind speeds and frequency bands (1 kt = 1.852 km/h). The probability w to have the indicated or better conditions is taken from [37], and is valid for the AUTEK site near the Bahamas.

	0 – 500 kHz	0 – 100 kHz	3 – 100 kHz	w
1 kt	36.0	7.9	4.5	0.01
5 kt	42.0	23.1	9.9	0.2
13 kt	90.3	83.2	41.4	0.6
30 kt	188.0	184.0	82.0	1

These values now allow us to develop a single sensor trigger for bipolar pulses, and to estimate the sensitivity of a single sensor system to neutrino induced pressure pulses.

6.3.2 Filtering in the time domain

The most simple trigger algorithm is to use a threshold trigger. The pressure signal in the sensor is monitored, and when the pressure rises above some threshold pressure p_{th} the time and the maximum amplitude of the signal are recorded.

The distribution of wind speeds, and thus the temporal variation of the noise is known (e.g. [37]). It can be calculated, that, if one uses single hydrophones and an appropriate bandpass filter to eliminate the noise in the frequency bands where no signal contribution is expected, a threshold $p_{\text{th}} = 35$ mPa has to be used if one allows for one event triggered only from background in 10 years with a five fold coincidence [61].

Since especially the thermal noise is expected to have a very short correlation length⁴ it will be possible to further increase the signal-to-noise ratio, and correspondingly decrease the threshold pressure p_{th} by using sensor clusters where the signals from the single sensors are summed up coherently. For completely uncorrelated noise the signal-to-noise ratio in a sensor cluster of N sensors is expected to increase by \sqrt{N} .

For the simulation study presented in this work we will use such a threshold trigger, and assume that, with appropriate techniques, the detection threshold for neutrino induced bipolar acoustic pulses can be lowered down to $p_{\text{th}} = 5$ mPa. The dependence of the detector sensitivity on p_{th} will be discussed in Sec. 7.4.

More sophisticated filtering techniques like the usage of correlation functions between the measured data stream and the expected bipolar signal shape are under

⁴The Erlangen ANTARES group will equip two sectors of the ANTARES detector with acoustic sensors to study the properties of the noise at the ANTARES site in the Mediterranean Sea, especially the correlation lengths at different frequencies, in-situ. The arrangement of the sensors will allow to measure correlations over two orders of magnitude in length, from 1 m to 100 m.

study in Erlangen.

6.3.3 Filtering in the frequency domain

A common method is to analyse time slices with a length, which is a few times the length of the expected signal. Calculating the total energy in a frequency band between for example 3 kHz and 100 kHz where the signal is expected to dominate over the noise will allow to distinguish between time slices that contain a signal and those that contain no signal. The advantage of this method is, that neither the exact position of the signal in the time slice has to be known to identify it, nor the exact shape of the signal, since the energy can be distributed over the considered frequency band. If a time slice is identified to contain a signal, more sophisticated algorithms with higher CPU time requirements can be used to determine the exact time and amplitude of the signal.

In the following we will restrict ourselves to detectors where the problem of signal extraction out of the noise is already solved. We define the *acoustic module* (AM) to be the basic element of our acoustic neutrino telescope:

An acoustic module (AM) is a device that can unambiguously trigger on bipolar acoustic pulses, as they are for example produced by neutrino induced particle cascades, which have a maximum pressure amplitude greater than some threshold pressure p_{th} , and can measure and transmit to shore their arrival time and amplitude.

An acoustic module will most probably be some local array of acoustic sensors like hydrophones or naked piezo ceramics mounted into a pressure tight vessel [62] combined with a dedicated filtering algorithm for bipolar pulses.

6.4 Parameterisation of the acoustic signal

In this section we will develop a parameterisation of the maximum amplitude of neutrino induced bipolar pressure pulses as a function of the sensor position, which is a prerequisite for the simulation of an acoustic neutrino telescope presented in Chap. 7. We utilise the fact, that the pressure field is rotationally symmetric around the axis of the cascade. Thus, the pressure field can be described by the two coordinates distance r from the centre of the shower to the acoustic module and the angle ϑ between the shower axis and the vector pointing to the AM. The coordinate system used is shown in Fig. 6.6.

We have simulated acoustic pressure pulses produced by a 10^5 GeV hadronic cascade for various sensor positions using the methods described in Secs. 4.2.1 and 5.2.

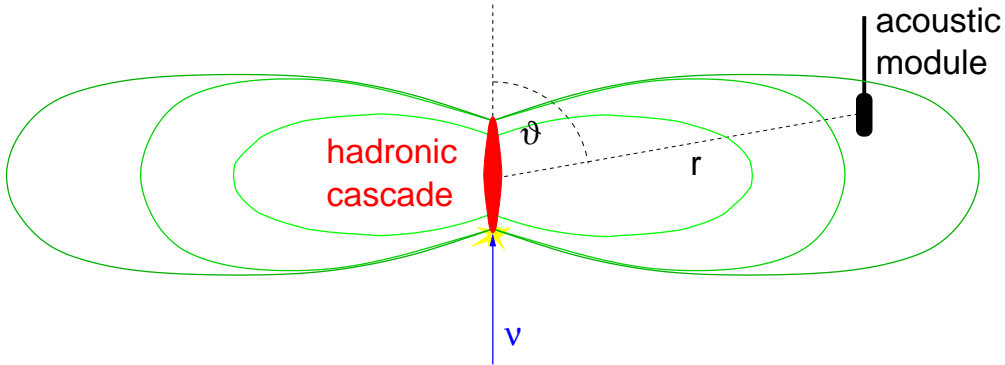


Figure 6.6: Coordinate system used for the parameterisation of the pressure field. The relevant coordinates are the distance from the shower centre and the angle to its axis. The system is rotationally symmetric around the cascade axis.

Attenuation of the signal due to the geometric spread is included in a natural way in the wave equation (4.1) from which the signals are calculated. Absorption of the signal is introduced into the simulation by first calculating the signal at the sensor position without absorption, and then using a Discrete Fourier Transform to determine its frequency components. Each frequency f is then attenuated by the frequency dependent absorption length presented in Fig. 6.1. The signal is then transformed back into the time domain.

For every signal the peak pressure amplitude p_{\max} and the corresponding arrival time t_{\max} were determined. To minimise the influence of binning effects of the energy deposition density by the hadronic cascade and of numerical errors of the integration of this density, all signals were calculated at 20 positions with constant r and ϑ , distributed at equal distances around the cascade axis. For the parameterisation the average values from these 20 signals were used.

We discovered that the most simple⁵ parameterisation can be achieved by calculating p_{\max} and t_{\max} as a function of r at a fixed angle ϑ , and repeat this procedure for different ϑ . Figure 6.7 shows a compilation of the results obtained. The error bars indicate the RMS of the 20 values calculated at positions around the shower axis.

As is expected for a disc-shaped signal propagation, the signal is highest perpendicular to the shower axis ($\vartheta = 90^\circ$) and decreases rapidly in other directions. Further it can be seen, that the distance dependence can roughly be divided into three sections: A near field region $r < 15$ m (I) where the signal behaviour strongly depends on the source distribution, and thus on the direction where the measurement is performed, an intermediate transition region $15 \text{ m} < r < 100$ m (II), and a far field region $r > 100$ m (III) where the amplitude decreases like $1/r$ as expected

⁵Here, *simple* is meant in the sense that a simple functional form can be found and fitted to the derived values.

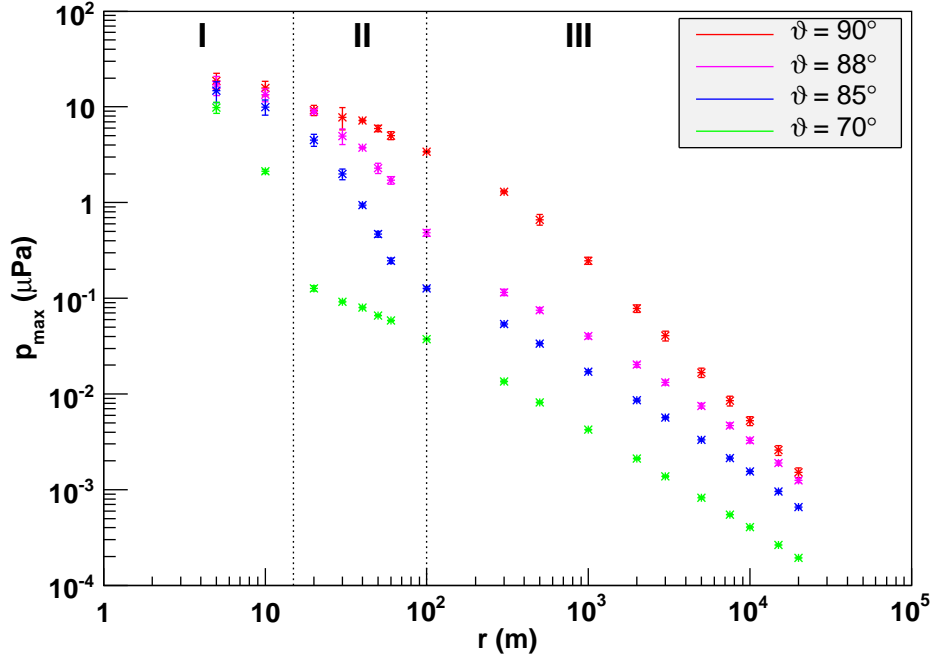


Figure 6.7: Dependence of the signal amplitude on the distance from the shower centre. The values are calculated for the 10^5 GeV hadronic cascade shown in Fig. 5.3. The different sets of data points are for different angles relative to the shower axis.

from a point source. Each of these sections shows a nearly linear behaviour in the double logarithmic plot. We use this to introduce the following parameterisation of the signal amplitude:

$$p_{\max}(r, \vartheta) = p_{0,i}(\vartheta) \left(\frac{r}{1 \text{ m}} \right)^{a_i(\vartheta)} \quad i \in \{\text{I, II, III}\} \quad (6.7)$$

We obtain the parameters $p_{0,i}(\vartheta)$ and $a_i(\vartheta)$ from linear fits in the double logarithmic plot for the three regions discussed. The fit results are presented in Fig. 6.8.

In the far field (region III, blue symbols), where the energy distribution can be assumed as point-like, the amplitude drops like $1/r$ ($a = -1$) for nearly all angles, whereas the scaling factor p_0 decreases strongly in the forward and backward directions where only very small signals are expected for a line-like source. In a narrow window around $\vartheta = 90^\circ$ the signal drops more steeply, but p_0 is at least three orders of magnitude higher compared to other directions. Thus the main signal contribution propagates perpendicular to the shower axis, but the steeper decrease around $\vartheta = 90^\circ$ leads to a widening of the sonic disc for large distances.

It is noteworthy, that for intermediate distances (region II, magenta symbols) the amplitude drops like $1/r$ except for the narrow window around $\vartheta = 90^\circ$ where

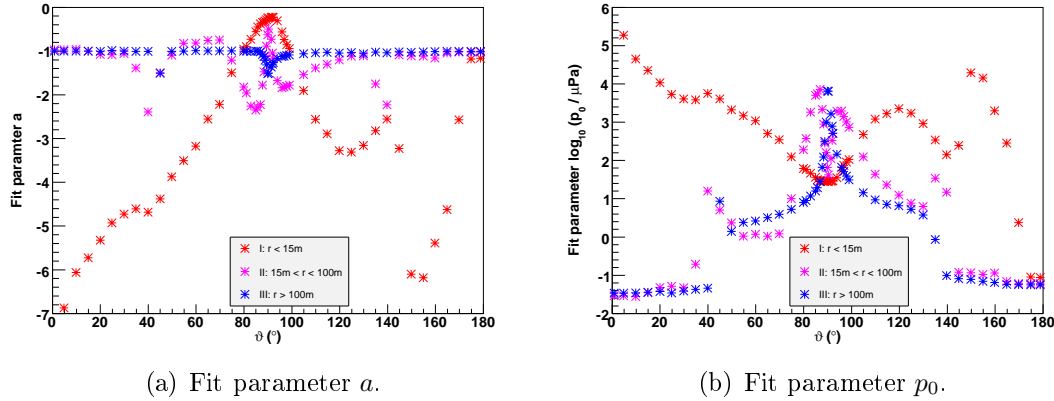


Figure 6.8: Parameter set to describe the pressure field. The values are obtained from fits $p_{\max}(r) = p_0 (r/1\text{ m})^a$ at fixed angle to the data shown in extracts in Fig. 6.7.

it decreases like $1/\sqrt{r}$ ($a = -1/2$) as expected for a line source. This leads to the very pronounced disc-shape of the sonic field.

In the forward and backward directions we expect no signal from the disc-shape model. In the near field (region I, red symbols) we get high p_0 in the forward direction, but the signal decreases like r^{-7} which leads to a strong suppression of the signal. In the backward direction the signal decreases only like $1/r$, but p_0 is suppressed by at least three orders of magnitude compared to all other directions, so that also in the backward direction no significant signal contribution is expected.

Despite of apparent fluctuations in the fit parameters, the variation with the angle ϑ is smooth around $\vartheta = 90^\circ$ where the signal is highest, which leads to reliable predictions of the signal amplitude.

We can now calculate p_{\max} for every sensor position from these 312 parameters⁶ stored in a lookup-table. For a given AM position we determine the distance r to the shower centre which sets the required region. Then, the angle ϑ is determined, and the corresponding parameters p_0 and a are calculated by linear interpolation in the ϑ interval the required angle is included. In a last step the absolute amplitude of the signal is calculated from the energy of the cascade, since we assume, as was discussed in Sec. 5.2, that the amplitude scales linearly with the cascade energy. The resulting pressure field can be seen in Fig. 6.9.

The plot shows lines of constant pressure produced by a hadronic cascade centred at the origin and developing in the positive z direction. The lobes perpendicular to the cascade axis, which form the characteristic disc-shape since the plot is rotationally symmetric around the z axis, are clearly visible. Also the widening of the

⁶52 angles times three regions times two parameters (p_0 and a). The angular resolution of the lookup-table varies between 5° in the forward and backward directions and 0.5° perpendicular to the shower, where the main signal contribution is expected.

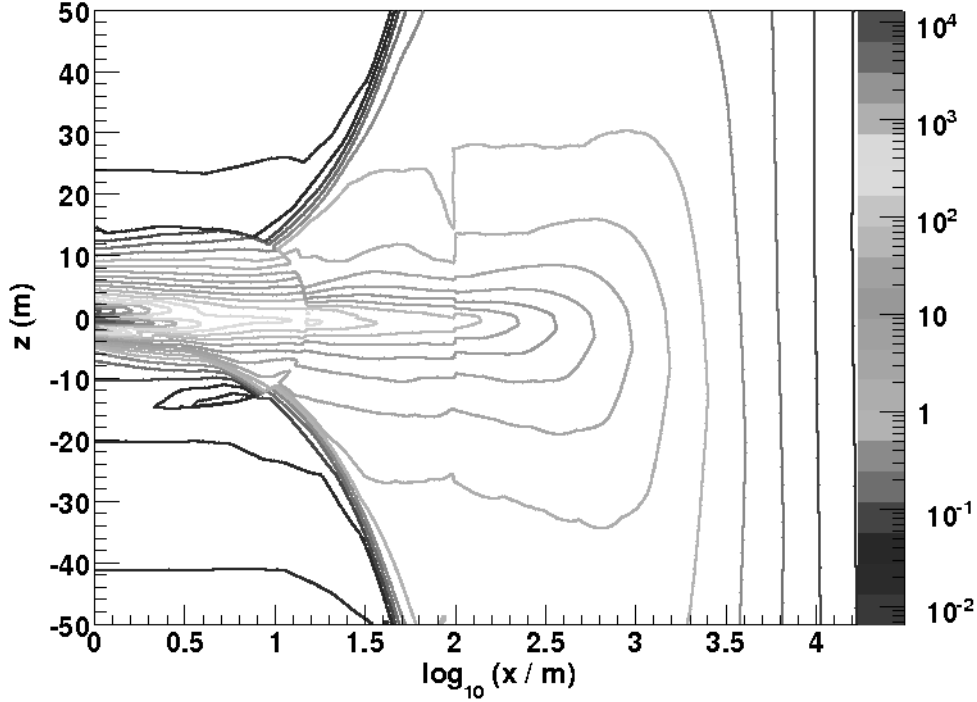


Figure 6.9: Parameterisation of the pressure amplitude p_{\max} produced by a hadronic cascade. The shower is centred at the origin and develops in positive z direction. The colour scale gives the pressure in $\text{mPa} / 10^9 \text{ GeV}$. The discontinuities at $r = 15 \text{ m}$ and $r = 100 \text{ m}$ result from the parameterisation method described in the text.

disc in the far field which was discussed previously can be seen nicely.

The second parameter of importance is the arrival time t_{\max} of the pressure peak at the acoustic module. It was calculated together with p_{\max} for all distances r and angles ϑ , and it turns out that the spatial extension of the energy deposition region is not important for the arrival times, which have to be determined with a precision of $10 \mu\text{s}$. The time can simply be calculated from:

$$t_{\max}(r, \vartheta) = \frac{r}{c} \quad (6.8)$$

where c is the speed of sound in water.

Chapter 7

Simulation study of an acoustic neutrino telescope

Contents

7.1	Detector simulation	65
7.2	Event reconstruction and selection cuts	69
7.3	Separation of background	76
7.4	Sensitivity of an acoustic neutrino telescope	77
7.5	Comparison with other simulations	84

In this chapter, the knowledge of acoustic pulses produced by ultra high energy neutrinos gathered in the previous sections is used to study the properties of an acoustic neutrino telescope. First, the detector simulation is presented, then a reconstruction algorithm for the direction and energy of the neutrino induced cascades is discussed. In the last section the sensitivity of different detector setups to an diffuse neutrino flux is derived.

7.1 Detector simulation

Figure 7.1 shows a schematic view of the detector simulation setup used for this study.

The simulation consists of a cylindrical can volume and a detection volume instrumented with acoustic modules (AMs, cf. Sec. 6.3). In the first three sections of this chapter an instrumented volume of $1 \times 1 \times 1 \text{ km}^3$ is chosen. To avoid any bias on the simulation from the configuration of the AMs inside the detection volume, we use 200 AMs distributed homogeneously, but randomly over the instrumented volume. The influence of the size of the instrumented volume and of the density of the acoustic modules on the sensitivity of the neutrino telescope will be discussed in Sec. 7.4.

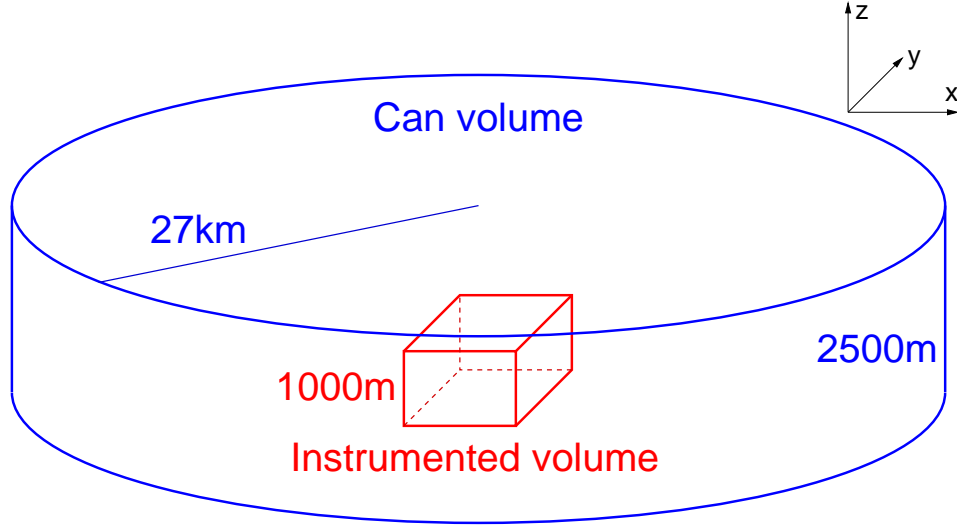


Figure 7.1: Schematic of the detector simulation setup.

An isotropic flux of downward going ultra high energy neutrinos interacting inside the can volume is generated. The can has a height of 2500 m which is a typical depth in the Mediterranean Sea, and, for the 1 km^3 size detector, a radius of 27 km since we assume that no signal from neutrino interactions farther away can reach the detector due to refraction in the water (cf. Sec. 6.2). The detection volume is horizontally centred inside the can volume, 100 m to 1100 m above the sea floor. Later, when larger instrumented volumes will be considered, only the area of the instrumented volume will be increased at a constant height of 1 km, since we know from the water Čerenkov telescopes being built in the Mediterranean Sea that it is difficult from an engineering point of view to deploy structures higher than about 1 km.

A complete simulation code was developed during this work in C++, which generates events in an acoustic neutrino telescope from the following input:

- Detector description (A file containing the positions of the AMs; the AMs are assumed to have isotropic sensitivity, so no orientation of the AMs needs to be stored).
- Height and radius of the can volume, and position of the detection volume relative to the can volume.
- Number N of neutrino interactions to be generated.
- Neutrino energy range $[E_{\min}, E_{\max}]$.
- Detection threshold p_{th} of the individual AMs.

- Amplitude resolution σ_p , time resolution σ_t , and position resolution for the AMs σ_{AM} (see below).
- Trigger threshold N_t of the detector (see below).

For each of the N neutrino interactions the following steps are performed during the simulation:

1. The energy E_ν of the neutrino is determined randomly in the predefined energy range $[E_{\min}, E_{\max}]$ from an energy distribution which is flat in $\log E_\nu$ (cf. Fig. 7.2):

$$\frac{dN}{d(\log E_\nu)} = \text{const.} \quad \Leftrightarrow \quad \frac{dN}{dE_\nu} \propto E_\nu^{-1}$$

2. The position of the neutrino interaction vertex is chosen randomly such that the interactions are distributed homogeneously over the can volume.
3. The direction of the hadronic cascade, which is assumed to coincide with the direction of the neutrino and thus is down-going (cf. Sec. 5.1), is determined randomly to guarantee an isotropic flux of down-going neutrinos (i.e. flat distribution of the azimuth $\varphi \in [0, 2\pi[$, and flat distribution of the cosine of the zenith $\cos \theta \in [0, 1]$).
4. The energy E_{had} of the hadronic cascade produced in the interaction is drawn randomly using E_ν and the distribution of the kinematic energy variable y shown in Fig. 5.2(a) which describes the energy transfer to the hadronic system.
5. For all acoustic modules in the detector description:
 - a) Each of the three position coordinates of the AM is smeared out using a Gaussian probability density function with a width given by the position resolution σ_{AM} of the detector. This accommodates the fact that for a submarine structure extending over several cubic kilometres the position of the individual components can only be fixed with a precision of approximately σ_{AM} . We use $\sigma_{\text{AM}} = 10$ cm for our simulation which is the value the ANTARES neutrino telescope will achieve for the positioning precision of its photomultiplier tubes.
 - b) For the new AM position the amplitude p_{max} and arrival time t_{max} of the acoustic signal are calculated according to the parameterisation presented in the previous section.
 - c) The amplitude and arrival time are smeared by the amplitude resolution σ_p and the time resolution σ_t of the acoustic module. We use $\sigma_p = 2$ mPa and $\sigma_t = 10$ μs which corresponds to a sampling frequency of 100 kHz in the AM.

- d) If the smeared amplitude is larger than the detection threshold p_{th} of the AM, amplitude and arrival time are stored together with the ID of the acoustic module as a *hit*.
6. If the number of hits is larger than or equal to the trigger threshold N_t of the detector the set of hits is written to disc as an *event*.

Figure 7.2 shows the energy spectra of the neutrinos (yellow), the hadronic cascades (red), and the triggered events (green) for the 1 km^3 detector with 200 AMs, and $p_{\text{th}} = 5 \text{ mPa}$ and $N_t = 5$ which is the minimum number of hits to reconstruct the position and absolute time of the neutrino interaction vertex.

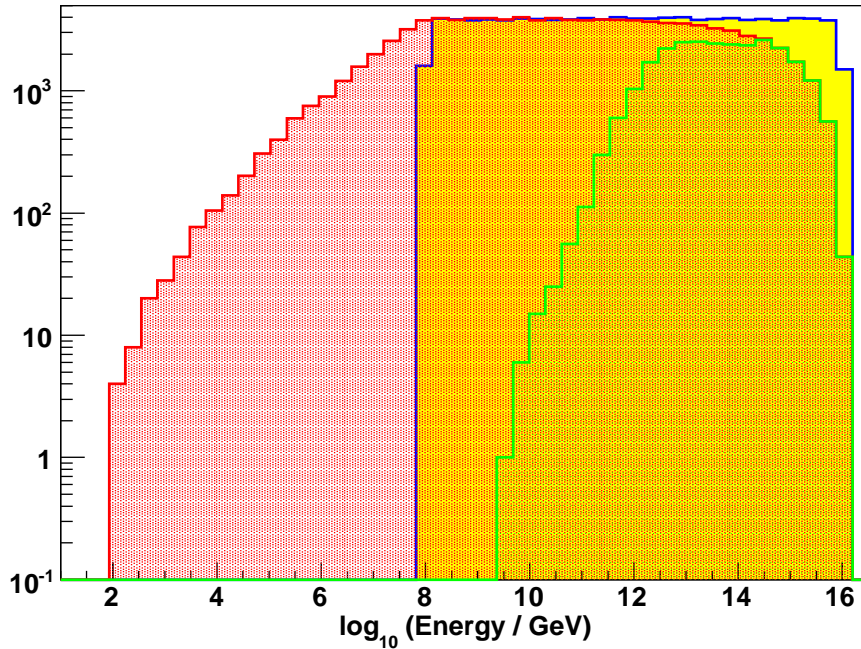


Figure 7.2: Simulated energy spectra of the 10^5 neutrinos injected into the can (yellow), the hadronic cascades produced (red), and the events fulfilling the trigger condition (green).

We generated 10^5 neutrinos with energies between 10^8 GeV and 10^{16} GeV . The energy spectrum of the hadronic cascades produced in the interactions is shifted to lower energies since a significant part of the energy is taken away by the lepton. 27% of all showers fulfilled the condition to produce a pressure amplitude $> 5 \text{ mPa}$ in ≥ 5 AMs. It can be seen easily, that the lower energy threshold of an acoustic neutrino telescope will be around 10^9 GeV .

In the next section we will present an algorithm to reconstruct the cascade direction and energy from a set of hits.

7.2 Event reconstruction and selection cuts

A two step reconstruction algorithm to determine the cascade direction and energy was developed for this thesis. In the first step, the position \vec{r}_0 and absolute time t_0 of the interaction vertex are estimated, in a second step the direction (θ, φ) and the energy E_{had} of the shower are fitted.

For the determination of \vec{r}_0 and t_0 we assume that the cascade is an isotropic point source, and minimise the sum Δ_t of the residuals of the arrival times. If N_h is the number of hits in an event, t_i is the arrival time measured at AM i , and \vec{r}_i is the position of this acoustic module, then

$$\Delta_t(\vec{r}_0, t_0) = \sum_{i=1}^{N_h} \frac{(|\vec{r}_i - \vec{r}_0|/c - (t_i - t_0))^2}{\sigma_t^2} \quad (7.1)$$

where c is the sound velocity in water. The function $\Delta_t(\vec{r}_0, t_0)$ is not a χ^2 function as known from statistics because the errors are systematically underestimated. To come to a real χ^2 fit one would also have to include the error introduced by the positioning uncertainty σ_{AM} into the measurement of the arrival times.

For the minimisation we use the C++ implementation of the Minuit¹ minimisation package that comes with the ROOT² data analysis framework. As a starting point for the minimisation we initialise the variable \vec{r}_0 with the centre of gravity of all AMs that have been hit and t_0 with the time of the first hit.

After the position of the vertex has been found we reconstruct the direction and energy of the cascade by minimising the sum Δ_p of the residuals between the measured amplitudes p_i and the amplitudes p_{exp} expected for a given set of $(\theta, \phi, E_{\text{had}})$ at the position \vec{r}_0 which is now fixed.

$$\Delta_p(\theta, \phi, \ln E_{\text{had}}) = \ln \left(\ln \sum_{i=1}^{N_h} \frac{(p_i - p_{\text{exp}}(\vec{r}_i, \vec{r}_0, \theta, \phi, E_{\text{had}}))^2}{\sigma_p^2} \right) \quad (7.2)$$

The expected amplitude p_{exp} is calculated by using the parameterisation of the pressure field presented in Sec. 6.4. Taking the logarithm of the sum twice is necessary for numerical reasons, since the values for p_{exp} fluctuate by several orders of magnitude depending whether the considered AM is inside or outside the sonic disc when varying the direction, and thus the sum over the residuals becomes very large. The minimisation is again carried out by using Minuit, whereby $\ln E_{\text{had}}$ is used instead of E_{had} as variable in the minimisation algorithm. The latter one would produce too large numerical uncertainties since it can vary over at least ten orders of magnitude.

¹<http://wwwasdoc.web.cern.ch/wwwasdoc/minuit/minmain.html>

²<http://root.cern.ch/>

We initialise the direction variables to start the minimisation with the normal of a plane through the three AMs that measured the highest amplitude and do not lie on a straight line, since they are expected to lie inside the sonic disc. The energy variable is initialised by a simple energy estimator assuming a $1/\sqrt{r}$ decrease of the amplitude in all directions from the fixed position \vec{r}_0 .

For 78% of all events which have produced a hit with an amplitude > 5 mPa in at least 5 AMs (21% of all hadronic cascades) the reconstruction algorithm finds a minimum. The errors of the reconstructed values compared to the Monte Carlo truth are shown in Fig. 7.3.

The reconstruction of the position and the time (upper two rows in Fig. 7.3) are very accurate. This is a prerequisite for the determination of the direction and the energy for which this information is required. In the horizontal plane, where the distance from the vertex to the detector extends up to 27 km, the vertex position can be reconstructed with an accuracy of 1.93 m. In the vertical direction, where the distances to the detector are much smaller – the can height is only 2.5 km – the position can be fixed much more precisely, up to 37 cm.

The direction error is the angle between the true direction of the hadronic cascade and the reconstructed direction. Due to the pancake-like shape of the pressure field, there is a 180° ambiguity in the reconstructed direction, i.e. if we look at the signature of some hadronic cascade in the detector, a hadronic cascade at the same position, but developing in the exact opposite direction, would produce the same hit pattern in the detector. Further, we do not expect any neutrinos from below the horizon. So we define the direction error $\Delta\alpha$ to be $180^\circ - \Delta\alpha$ for $\Delta\alpha > 90^\circ$.

There are events for which the direction is reconstructed very well, superimposed by a nearly flat distribution of events for which the direction reconstruction seems to fail completely. The mean error in $\log(E_{\text{had, reco}}/E_{\text{had, true}})$ is about -1, i.e. the algorithm tends to systematically underestimate the energy of the hadronic system by a factor of 10, which can be corrected for afterwards. The width of the distribution is 0.96. That means, that the energy of the hadronic cascade can on average be determined up to a factor of $10^{0.96} = 9.1$. In addition, there is a peak at -3, which indicates that there are events for which the energy is underestimated by a factor of 1000.

Further analysis of the misreconstructed events revealed, that mostly events produced from cascades with large zenith angles account for the badly reconstructed events, which is not very surprising because for an event with large θ_{true} produced far from the detector the core of the sonic disc will not transverse the detector and hits are only produced from the remainder of the pressure field which has only low direction characteristics. Figure 7.4 shows the errors in the direction and energy reconstruction as a function of the zenith angle of the cascade producing the event.

Obviously, the direction reconstruction becomes worse for the reasons discussed above the more inclined the shower is. It is further visible, that for cascades with zenith angles larger than about 20° , where only small parts of the core of the sonic

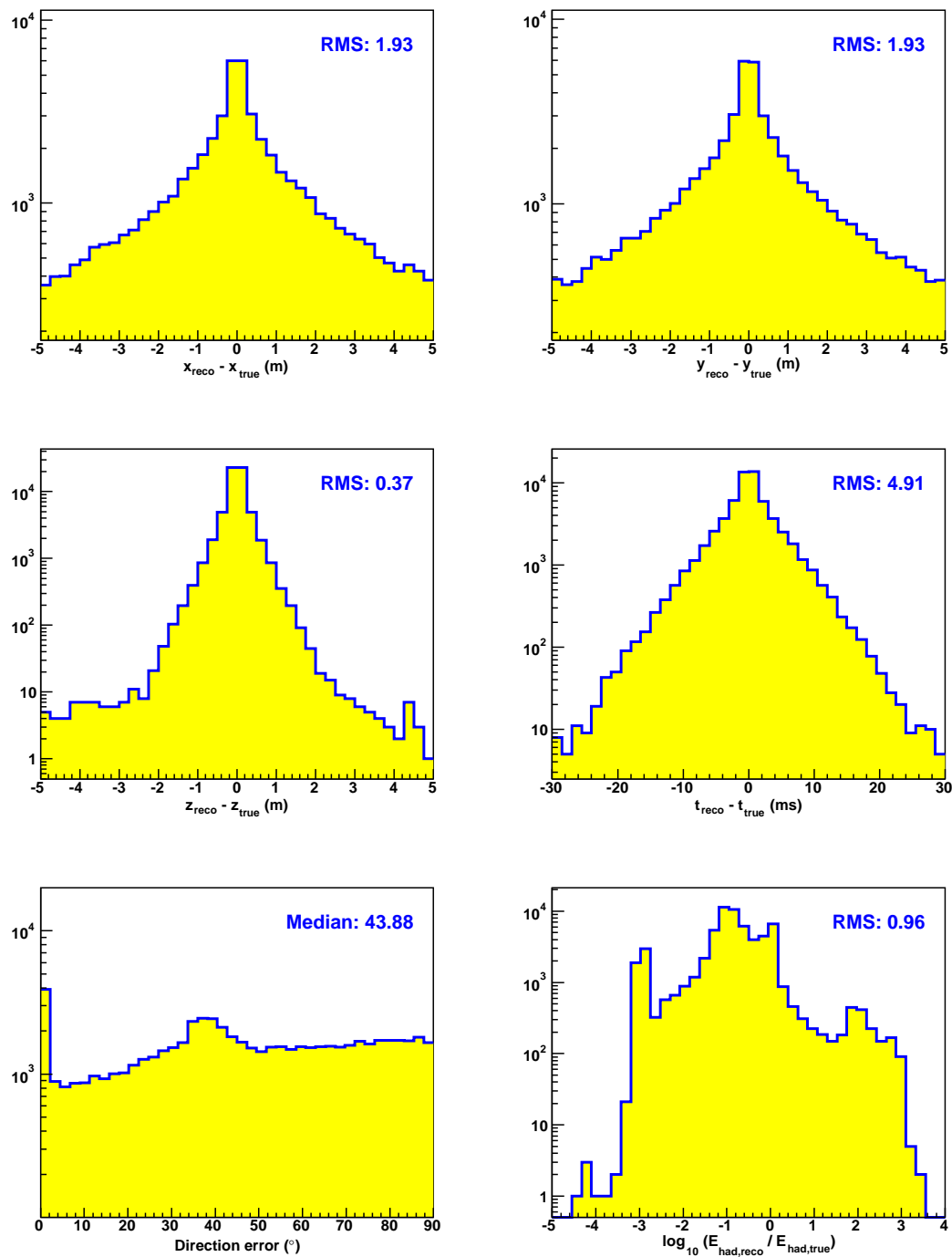


Figure 7.3: Reconstruction errors for hadronic cascades.

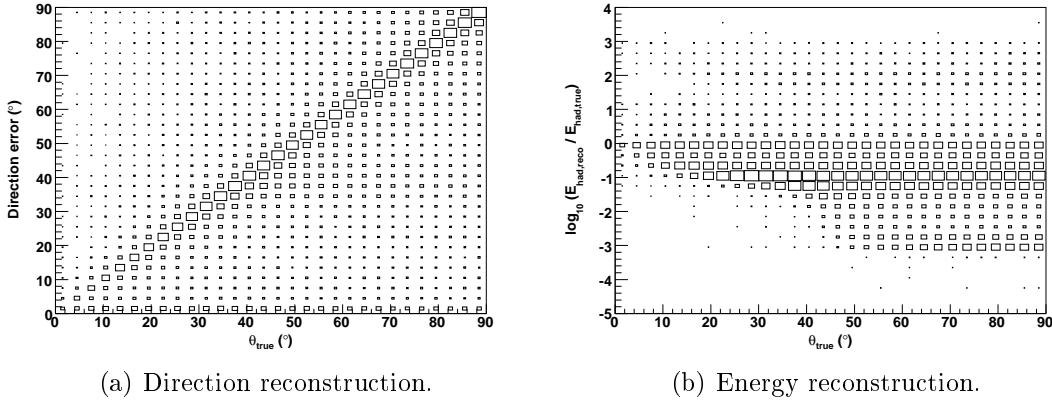


Figure 7.4: Reconstruction errors as a function of the true zenith angle of the cascade.

disc are inside the detector, the reconstruction algorithm starts to systematically underestimate the cascade energy. For very inclined showers ($\theta_{\text{true}} > 50^\circ$) the reconstruction algorithm starts to underestimate the energy by several orders of magnitude. Close inspection of those events reveals that they are produced by cascades with energies above approximately 10^{13} GeV, where even the small pressure pulses emitted in the forward and backward directions start to contribute to the measured hits.

The large uncertainty in the direction reconstruction poses no problem when only a diffuse neutrino flux is measured, which is expected for many of the cosmological models presented in Chap. 2. They predict a large number of similar sources at cosmological distances, so that only a few neutrinos from each individual source will be detected. Then, the distribution of the incident neutrinos will be isotropic and the direction of individual neutrinos is not of particular interest since we do not expect the discovery of any point sources of neutrinos. In this case only the energy resolution is of interest since one usually wants to measure the neutrino flux as a function of energy. Nevertheless, we investigated whether the resolution of an acoustic neutrino telescope can be improved by using selection cuts³. It turns out that there are three quantities which are suitable to cut on. Figure 7.5 shows in the left column the direction error and in the right column the error in the energy reconstruction as a function of the final value of the minimisation function Δ_p , of the reconstructed zenith angle θ_{reco} , and of the reconstructed azimuth φ_{reco} .

Badly reconstructed events have a tendency to have large values of Δ_p , which is related to the statistical χ^2 of the direction and energy fit. A good cut value for keeping well reconstructed events is $\Delta_p < 1.7$, where we tried to find a compromise

³A selection cut is a criteria to decide from quantities which are *measured* or calculated from measured quantities only, whether a particular event was well reconstructed.

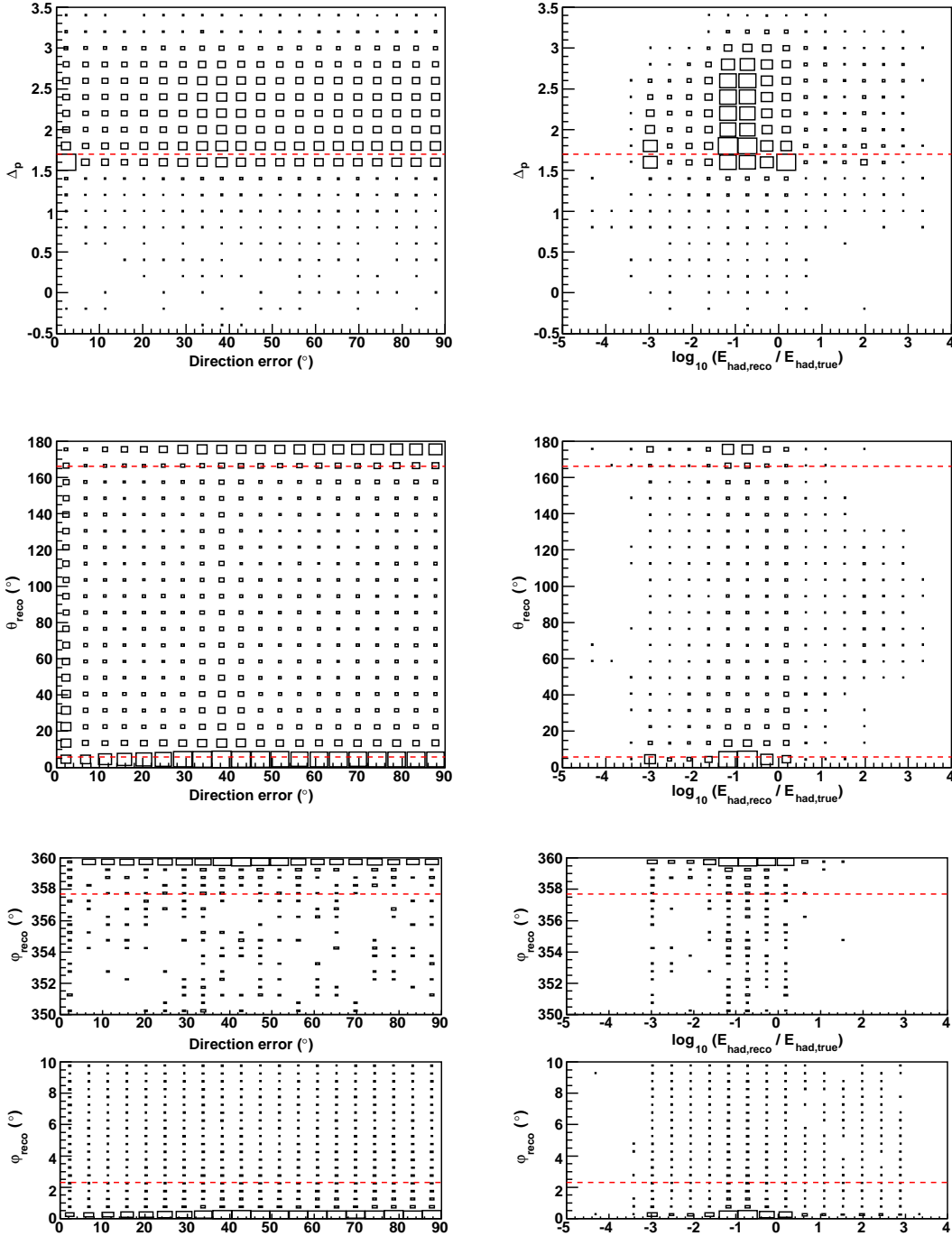


Figure 7.5: Errors in the direction and energy reconstruction as a function of the final value of the minimisation function Δ_p , of the reconstructed zenith angle θ_{reco} , and of the reconstructed azimuth φ_{reco} (For the latter only the boundaries around 0 and 360° are shown for better visibility of the effects of the cut). The dashed lines indicate possible selection cuts.

between improving the resolution and reducing the gathered set of events not too much.

Further, the reconstruction algorithm tends to drive the angles towards the boundary values 0 and 180° or 360° respectively, so that badly reconstructed events have values of θ_{reco} and φ_{reco} near these boundaries and can be conveniently cut. The only delicate cut is at the lower bound for θ_{reco} , since we have seen that down going cascades ($\theta_{\text{true}} = 0$) contribute most to the well reconstructed events. Convenient cut values are $5.7^\circ < \theta_{\text{reco}} < 166^\circ$, which does not eliminate too many good events since the solid angle with $\theta < 5.7^\circ$ is very small ($31 \cdot 10^{-3}$ sr), and $2.3^\circ < \varphi_{\text{reco}} < 357.7^\circ$. The influence of these cuts on the reconstruction accuracy is summarised in Tab. 7.1.

Table 7.1: Influence of the different selection cuts on the number of events, the median of the direction error $\Delta\alpha_{\text{med}}$, and the energy resolution.

Cut	# Events	$\Delta\alpha_{\text{med}}$	$\log \frac{E_{\text{reco}}}{E_{\text{true}}}$
none	63049 (100%)	43.88°	0.96
Δ_p	13585 (22%)	37.12°	1.13
θ_{reco}	29952 (48%)	37.12°	1.09
φ_{reco}	40257 (64%)	39.38°	0.94
all	5982 (9.5%)	12.38°	1.04

Obviously, only all three cuts together lead to a significant improvement of the direction resolution, whereas the energy resolution remains nearly unaffected. Figure 7.6 shows the distribution of the errors after the cuts are applied. The resulting energy spectrum of the events can be seen in Fig. 7.7.

The selection cuts mostly discard events with highest energies above 10^{13} GeV for which the reconstruction fails for the reasons elaborated before, namely that at these energies inclined showers produced far from the detector emit pressure amplitudes in the forward and backward directions sufficiently high to trigger the detector.

In summary we can say, that it is possible with an acoustic neutrino telescope to reconstruct the energy of neutrino induced hadronic cascade up to a factor of ten, which is sufficient to scrutinise cosmological models which predict neutrino fluxes extending over several orders of magnitude in energy. Since these hypothetical sources are expected to be distributed isotropically over the sky at cosmological distances, only a diffuse flux of neutrinos is expected at Earth, so that the low direction resolution of the telescope is acceptable. The direction resolution can be significantly improved up to 12° in the lower energy range (10^9 GeV to 10^{13} GeV) at the expense of a reduced statistics by using selection cuts.

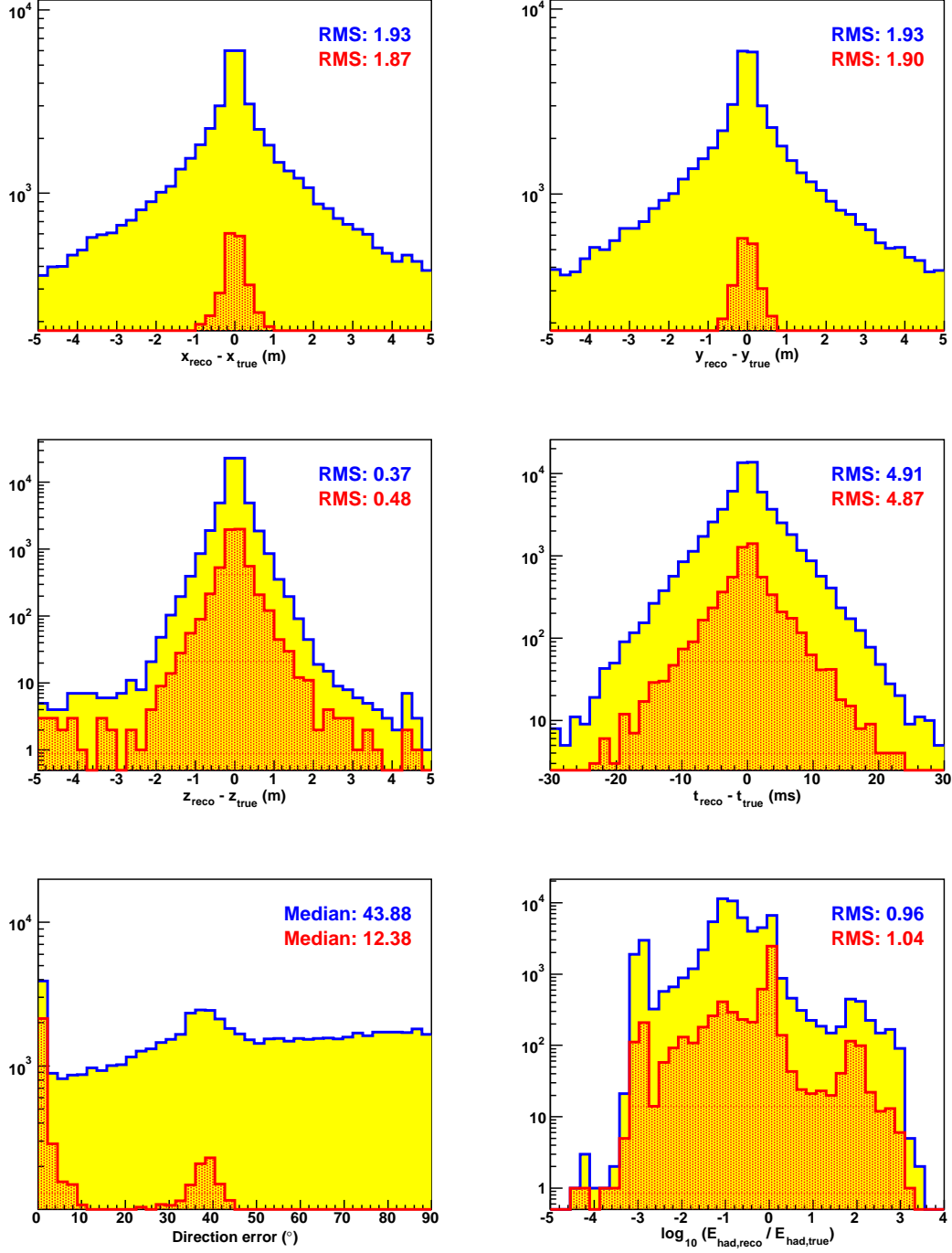


Figure 7.6: Reconstruction errors for hadronic cascades before (yellow) and after (red) the selection cuts are applied.

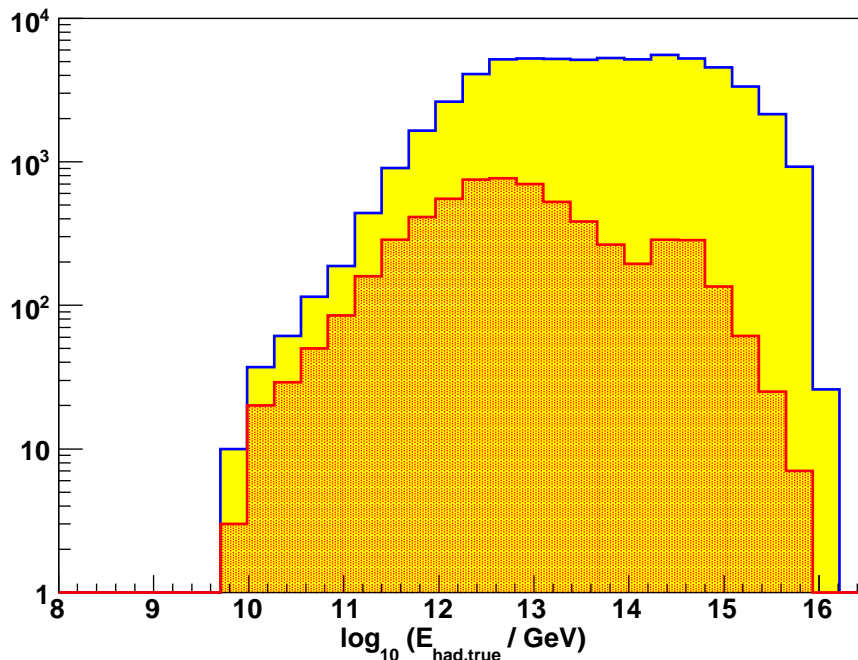


Figure 7.7: Energy spectrum of the events for which the reconstruction algorithm converged (yellow) and for the events which passed the selection cuts (red).

7.3 Separation of background

Another important topic which needs to be studied towards an acoustic neutrino telescope is the existence of background sources, i.e. of sound sources which might wrongly be identified as neutrinos. It is completely unknown whether there are any natural or anthropogenic sources which emit bipolar acoustic pulses that can be detected coherently over large distances. The Erlangen ANTARES group works towards instrumenting several structures of the ANTARES neutrino telescope with acoustic sensors [63] to measure the rate with which such background events occur.

In this section we will discuss the consequences of the existence of such hypothetical background sources for the development of an acoustic neutrino telescope. We implemented point sources which emit spherical waves into the simulation code. Their signal amplitude decreases like $1/r$, where r is the distance from the source. Absorption was neglected completely for the point source study. To have some energy measure for the point sources for comparison with hadronic cascades, we introduce an effective energy for the point sources: A point source is defined to have energy E if it produces, in a distance of 400 m from the source, a pressure amplitude equal to the amplitude produced by a hadronic cascade of energy E at this distance perpendicular to the cascade axis.

We simulated $3 \cdot 10^5$ point sources with the same energy spectrum used for the neutrino-like events (Fig. 7.2). From these $3 \cdot 10^5$ point sources 52% (154965) fulfilled the trigger condition to produce an amplitude ≥ 5 mPa in five or more acoustic modules (neutrino-like events: 27%). The reconstruction algorithm converged for 44% (132279) of all point sources generated (neutrino-like events: 21%), whereby the vertex position and energy of the point sources are reconstructed with the same accuracy as for neutrino-like events, and the direction reconstruction naturally fails completely. The selection cuts presented in the previous section are survived by 1.6% (4811) of the point sources (neutrino-like events: 2.0%).

This means, that the presented reconstruction algorithm is not capable to distinguish between point sources and the more disc-like neutrino induced events. Nonetheless, the two event classes produce different hit patterns in the detector which, if it should prove necessary, could be used to distinguish between them. To see this, we define the variable f_n to be the fraction of hits in an event which have an amplitude of $n/100$ or more of the maximum amplitude measured in an event. For neutrino-like events we expect only few high amplitude hits around the sonic disc, whereas for point sources the wave front is expected to propagate through the entire detector, producing similar amplitudes in large parts of it. The distribution of f_{10} , f_{50} , and f_{90} for neutrino-like events and point sources is shown in Fig. 7.8.

The distributions of f_{10} and f_{50} show, that for point sources, in contrary to neutrino induced events, there are practically no hits which have an amplitude lower than 10% of the maximum amplitude and only a few hits with an amplitude lower than 50% of the maximum amplitude. Further, neutrino-like events contain only a few hits with an amplitude larger than 90% of the maximum amplitude measured in the event.

These distributions might allow to separate point sources from neutrino like events if the rate of point sources is lower or of the same order of magnitude as the rate of neutrino induced events. Thus, it is crucial to measure the rate and properties of acoustic background with long correlation length, as we plan to do within the ANTARES experiment, before deducing the feasibility of building an acoustic neutrino telescope. For the remainder of this work we will assume, that there is no such background.

7.4 Sensitivity of an acoustic neutrino telescope

In this final section we will derive the sensitivity of an acoustic neutrino telescope to a diffuse flux of ultra high energy neutrinos. A general introduction to the calculation of flux limits is given in Appendix B.

For the simulated acoustic neutrino telescope we define the effective volume V_{eff} as

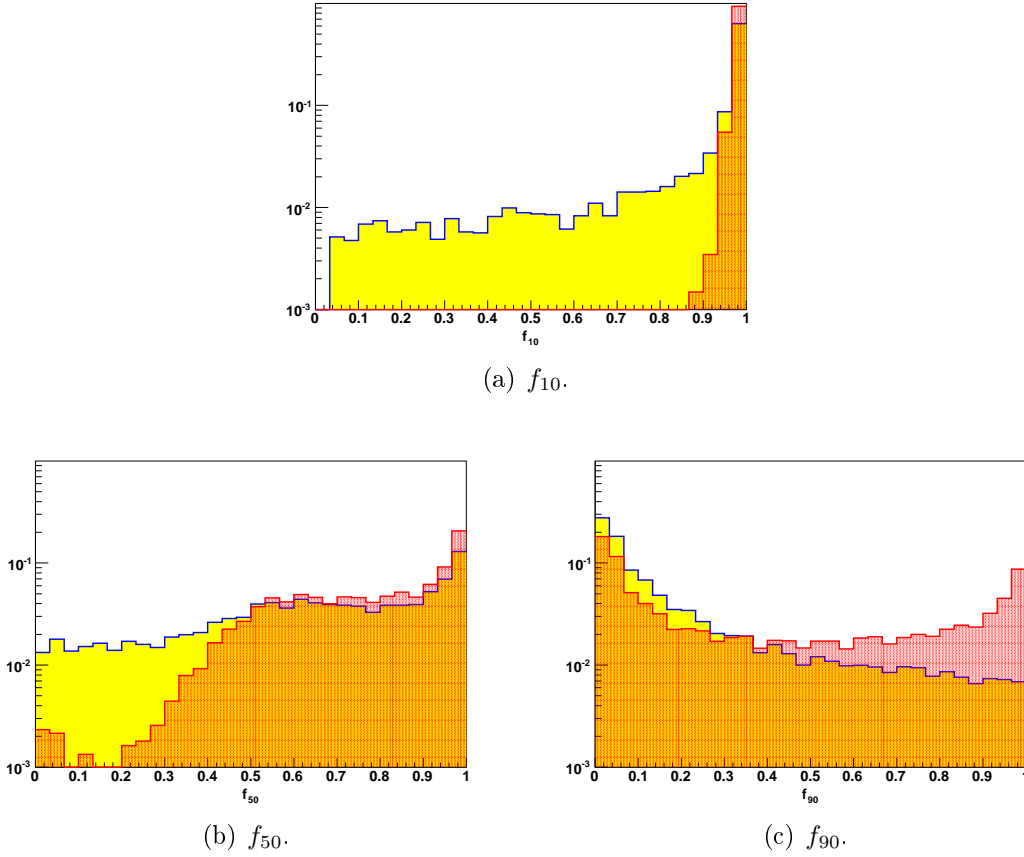


Figure 7.8: Distribution of the variables f_{10} , f_{50} , and f_{90} for neutrino-like events (yellow) and point sources (red) which pass the reconstruction algorithm, but without any selection cuts applied.

$$V_{\text{eff}} = \frac{N_{\text{det}}}{N_{\text{gen}}} V_{\text{gen}} \quad (7.3)$$

where N_{det} is the number of detected neutrinos, i.e. the number of cascades which produce a trigger and for which the reconstruction algorithm converges, whereby the selection cuts can be applied or not. N_{gen} is the number of cascades produced in the generation volume V_{gen} , which in our case is the can volume. The aperture (B.2) is then given by

$$\mathcal{A}(E) = \int d\Omega \sigma_{\text{tot}}(E) N_t(V_{\text{eff}}) P(E, \Omega) \quad (7.4)$$

where σ_{tot} is the total neutrino nucleon cross section (5.1), N_t is the number of target nucleons inside the effective volume V_{eff} , and $P(E, \Omega)$ is the probability for

a neutrino of energy E and direction Ω to propagate to the can level. As was laid out in Sec. 5.1, we assume that all neutrinos coming from above the horizon can propagate unperturbed to the can level, whereas all neutrinos from below are absorbed inside the Earth:

$$P(E, \Omega) = \begin{cases} 1 & \text{for } \theta < 90^\circ \\ 0 & \text{for } \theta \geq 90^\circ \end{cases}$$

and thus

$$\mathcal{A}(E) = 2\pi\sigma_{\text{tot}}(E)N_t(V_{\text{eff}}) \tag{7.5}$$

The effective volume of the neutrino telescope presented in the previous sections as a function of the neutrino energy is shown in Fig. 7.9.

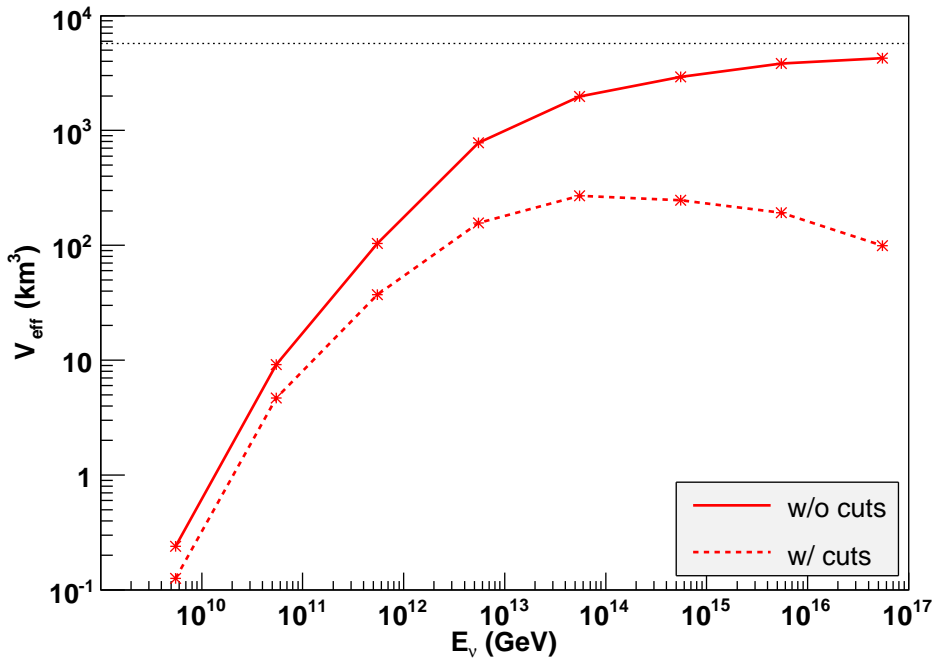


Figure 7.9: Effective volume of the 1 km³ detector as a function of the neutrino energy without selection cuts, and with selection cuts applied. The dotted line indicates the can volume.

Without the selection cuts applied the effective volume approaches the can volume of 5726 km³ asymptotically, which is a natural bound for the effective volume since we have shown that no signals from beyond the can volume reach the detector. When we apply the selection cuts, the effective volume starts to decrease again above approximately 10¹⁴ GeV due to the fact, that the selection cuts mainly discard highest energy events.

We will now investigate the influence of the detector parameters on the effective volume. Figure 7.10 shows the dependence of the effective volume on the detection threshold p_{th} of the individual acoustic modules.

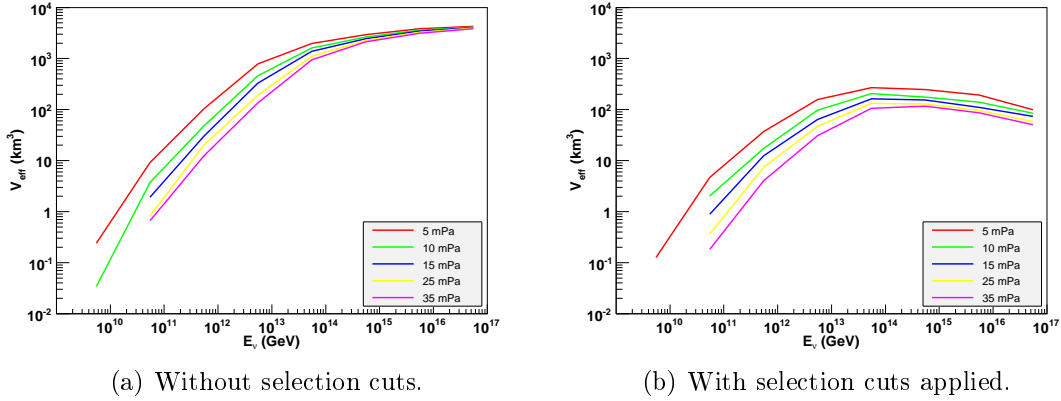


Figure 7.10: Effective volume as a function of the detection threshold p_{th} . The detector consists of 200 AMs distributed over 1 km^3 .

As we have seen, this detection threshold is set by the ambient background noise in the sea. High-level background noise, which would force an increase of the detection threshold, mainly affects the sensitivity for low energies. Whereas for the highest energies the effective volume is nearly independent of p_{th} , it decreases by about a factor of ten at 10^{10} GeV when p_{th} is increased from 5 mPa to 35 mPa. Thus, the optimisation of filtering algorithms to achieve a p_{th} as low as possible is crucial for an acoustic neutrino telescope.

The dependence of the effective volume on the density of acoustic modules is shown in Fig. 7.11.

It can be seen that an increase of the instrumentation density above $200 \text{ AM}/\text{km}^3$ does not lead to a significant increase in sensitivity. If one is only interested in neutrinos at highest energies $E_\nu \gtrsim 10^{13} \text{ GeV}$ one can even build a detector with as few as $10 \text{ AM}/\text{km}^3$ utilising the fact, that acoustic signals emitted in all directions from the cascade can be detected at these energies. We cannot show the dependence of the effective volume on the instrumentation density with selection cuts applied, since the selection cuts are sensitive to the detector geometry, and would have to be redeveloped for each detector.

At last we will investigate the dependence of V_{eff} on the instrumented volume V_{inst} . We assume that the instrumented volume is set on the sea bed at a depth of 2500 m and has cylindrical shape with a height of 1000 m, and a radius of $r_{\text{inst}} = \sqrt{V_{\text{inst}}/1 \text{ km}^3/\pi}$. Since, for a constant instrumentation density, the computing time of the simulation rises linearly with the instrumented volume, simulations for very large volume detectors are impractical and we will estimate this dependence from

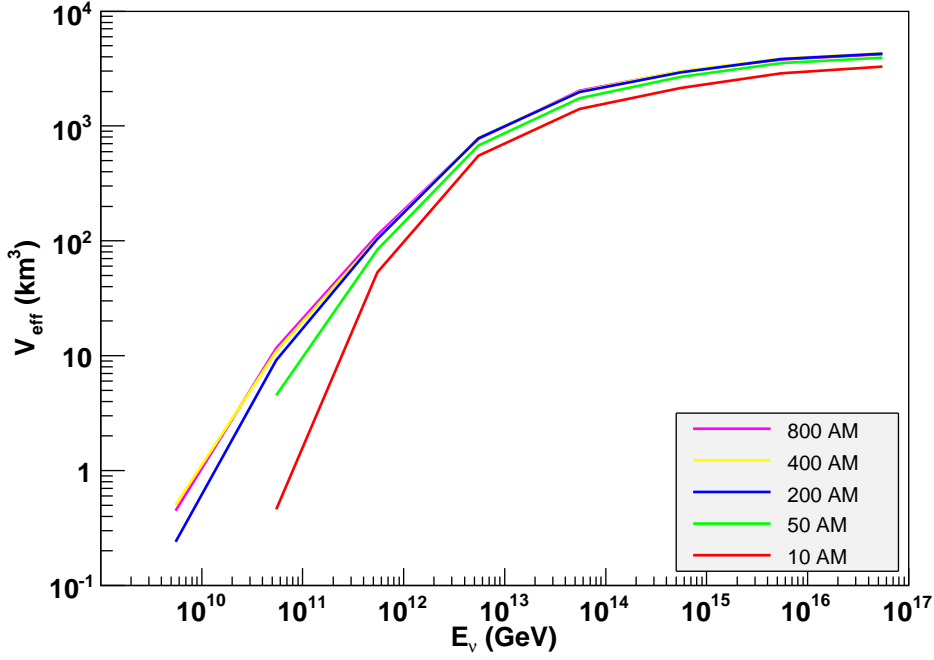


Figure 7.11: Effective volume as a function of the AM density. The instrumented volume is 1 km^3 with $p_{\text{th}} = 5 \text{ mPa}$ for each detector.

the simulations of the 1 km^3 detector.

If the effective volume is smaller than the instrumented volume, we can assume that the effective volume increases linearly with the instrumented volume:

$$V_{\text{eff}} = \frac{V_{\text{eff}, 1 \text{ km}^3}}{1 \text{ km}^3} V_{\text{inst}} \quad (7.6)$$

If the effective volume is larger than the instrumented volume, we assume that the complete instrumented volume contributes to the effective volume, and that it further extends up to the sea surface and some distance b , which is independent of V_{inst} , horizontally beyond the instrumented volume:

$$V_{\text{eff}} = \pi(r_{\text{inst}} + b)^2 \cdot 2.5 \text{ km} \quad (7.7)$$

where b can be calculated from the simulation of the 1 km^3 detector. The resulting dependence of the effective volume on the instrumented volume is shown in Fig. 7.12 for different neutrino energies.

At low energies the effective volume is proportional to the instrumented volume, whereas at highest energies V_{eff} remains nearly constant over a wide range of V_{inst} , and starts to increase only when V_{inst} becomes larger than the initial effective volume for small detectors.

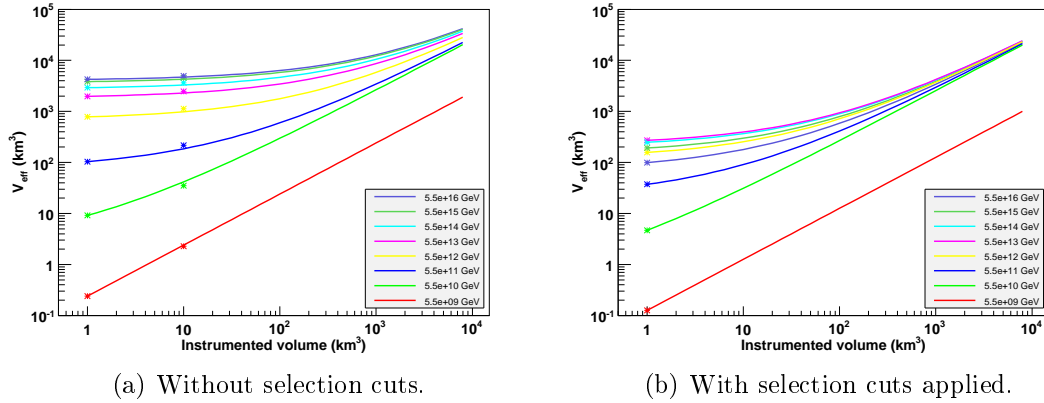


Figure 7.12: Effective volume as a function of the instrumented volume for different neutrino energies. The solid lines are calculated from (7.6) and (7.7), where b was determined from V_{inst} at 1 km^3 . The simulation results (data points) for $V_{\text{inst}} = 10 \text{ km}^3$ agree well with the model. The selection cuts cannot be applied to the events from larger detectors, so no simulation results for larger detectors are shown here.

This now allows us to estimate the sensitivity of an acoustic neutrino telescope to the neutrino fluxes expected to be produced by the different cosmological models presented in Chap. 2, and to compare the acoustic detection technique to the other experiments discussed in Chap. 3. We will restrict the discussion to a detector with 200 AM/km^3 , which was shown above to be sufficient, and a detection threshold of the acoustic modules of $p_{\text{th}} = 5 \text{ mPa}$.

First we will present a model independent flux limit at 90% confidence level (C.L.), calculated as described in Appendix B, and compare it to the results shown in Fig. 3.7. It turns out, that an instrumented volume of greater than thousand cubic kilometres is required to obtain competitive results. Figure 7.13 shows the resulting flux limit for an instrumented volume of 1500 km^3 (diameter: 44 km , height: 1 km) after a measurement time of 5 years.

Such a detector would have a sensitivity comparable to the sensitivity of the ANITA radio Čerenkov detector. This would allow to test theoretical source models with two experimental approaches which are completely independent, and thus have completely different sources of systematic errors. This is of utter importance when measuring in an energy region where no calibration sources are available. A test of all the source models shown as blue curves in Fig. 7.13 would be possible.

The sensitivity to the small flux of GZK neutrinos and the Waxman Bahcall upper bound is examined more closely in Fig. 7.14, which shows the 90% C.L. upper limit on these fluxes.

With the presented detector a non-detection of GZK neutrinos after 245 days would rule out the presented model on a 90% C.L. The Waxman Bahcall upper

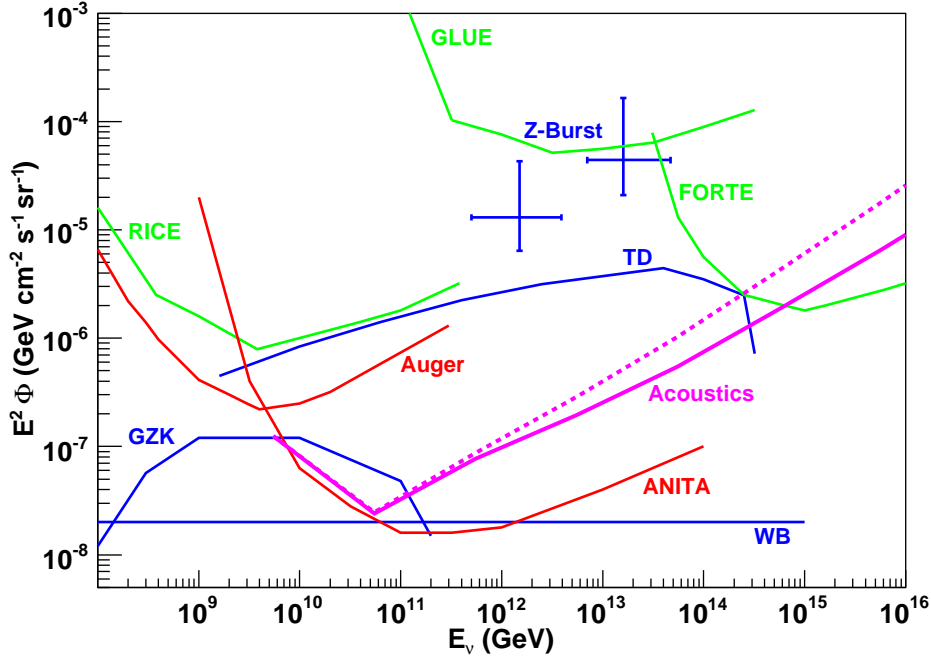


Figure 7.13: Model independent sensitivity of a 1500 km³ acoustic neutrino telescope after 5 years measurement time without selection cuts (solid line) and with selection cuts applied (dashed line) (RICE from [30], Auger from [31], GLUE from [32], FORTE from [29], ANITA from [30], WB from [12], GZK from [16], Z-Bursts from [22], TD from [21]).

bound could be reached after about 5 years of measurement time.

Despite of the large instrumented target mass the proposed detector requires only⁴ $3 \cdot 10^5$ DAQ channels⁵ to be read out. Further, data is taken with a frequency of 100 kHz only, and will only be transmitted from the acoustic module to a central DAQ system when the AM identifies a candidate bipolar pulse. Thus, from an engineering point of view, the design of such a detector should be feasible. Further, the sensitivity should be improved by the inclusion of electromagnetic cascades, which also produce utilisable acoustic signals, but had to be neglected completely in this work.

⁴For comparison: The ATLAS detector at the LHC is expected to have more than 10^8 readout channels

⁵ $200 \text{ AM/km}^3 \times 1500 \text{ km}^3$

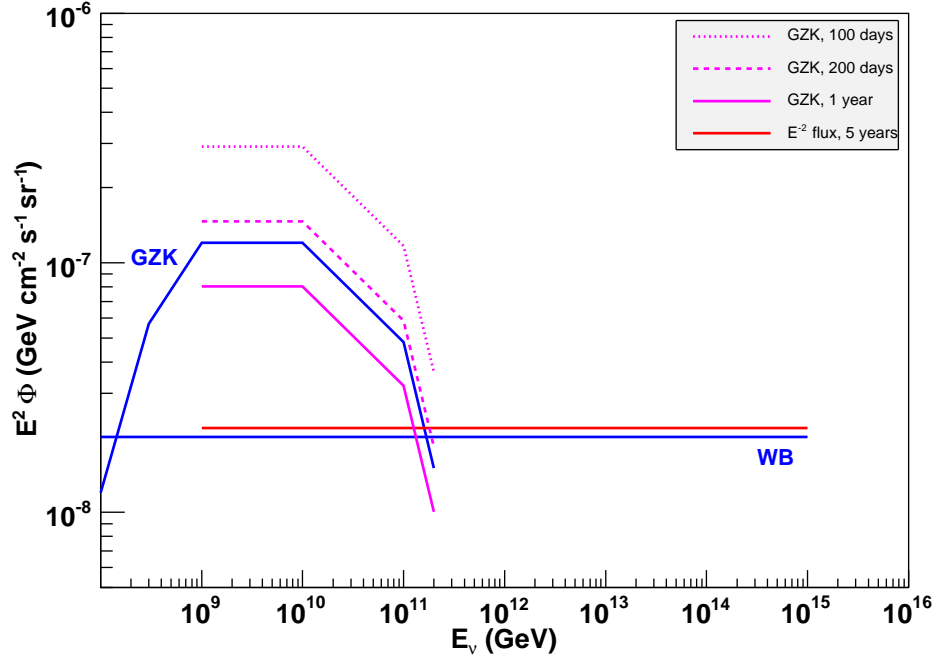


Figure 7.14: Sensitivity of a 1500 km^3 acoustic neutrino telescope to GZK neutrinos and the Waxman Bahcall upper bound (WB from [12], GZK from [16]).

7.5 Comparison with other simulations

There are other groups which are also studying acoustic neutrino telescopes in water [64, 65] or ice [66], where the latter one has published sensitivity estimates for a very large volume detector which can be compared with our results.

The speed of sound in ice ($c_{\text{ice}} \approx 3500 \text{ m/s}$) is about 2.3 times higher than in water. Since hadronic cascades are expected to develop equally in water and ice and the amplitude of the acoustic signal is proportional to c^2 (4.4) acoustic pulses in ice are expected to have a signal amplitude 5.4 times larger than in water for equal energies of the hadronic system. Thus, an acoustic neutrino telescope in ice is expected to be more sensitive than in water, especially at low energies.

In [66] the simulation of an acoustic neutrino telescope with an instrumented volume $V_{\text{inst}} = 98 \text{ km}^3$ and 27300 AMs (280 AM/km^3) arranged on 91 vertical strings submerged in ice is presented. For the simulation of the ice detector an AM threshold $p_{\text{th}} = 9 \text{ mPa}$ is used yielding a lower energy threshold of about $5 \cdot 10^9 \text{ GeV}$ comparable to the lower energy threshold of our detector obtained with $p_{\text{th}} = 5 \text{ mPa}$. Table 7.2 compares the effective volume of the ice and water acoustic telescopes in the neutrino energy range where the two simulations overlap.

As expected, the effective volume, and thus the sensitivity, of the ice detector

Table 7.2: Comparison of the effective volume V_{eff} for the ice and water acoustic neutrino telescopes (Values for $V_{\text{eff,ice}}$ from [66]).

E_ν (GeV)	$V_{\text{eff,ice}}$ (km ³)	$V_{\text{eff,water}}$ (km ³)
$5.5 \cdot 10^9$	175	25
$5.5 \cdot 10^{10}$	445	300

is larger than of the water detector. Apart from the higher sound velocity in ice, there are three other reasons leading to an increase of the effective volume for the ice detector: For the ice simulation it is assumed that a constant fraction $y = 0.2$ of the neutrino energy is transferred to the hadronic system, whereas our simulation uses the full y distribution (Fig. 5.2) with a median of 0.08 which leads, in comparison, to a decrease of the sensitivity of the water detector. Further, Fig. 7.11 shows that for the lowest neutrino energies the difference between 280 AM/km³ used for the ice detector and 200 AM/km³ for the water detector induces about a factor of two in effective volume, whereas nearly no difference is expected at $5.5 \cdot 10^{10}$ GeV. For the simulation of the ice detector a reconstruction efficiency of unity is assumed for all down-going cascades. The reconstruction algorithm we use for the water telescope has an efficiency of about 50% at $5.5 \cdot 10^9$ GeV and of 78% at $5.5 \cdot 10^{10}$ GeV.

Taking the higher density of acoustic modules and the reconstruction efficiency into account leads to a ratio between the effective volumes gained with the two simulations of the order of 1.5, which can be accounted for by the increased sound velocity in ice and the different y distributions used. Thus, the results obtained by the two completely independent simulations are compatible, whereby an acoustic neutrino telescope in ice has a slightly increased sensitivity compared to water as detection medium due to the increased sound velocity in ice.

Chapter 8

Summary

We have presented a simulation study on a new technique for the detection of ultra high energy neutrinos from cosmological sources: Listening for thermoacoustic sound pulses in water which are emitted from particle cascades produced in neutrino interactions.

Whereas we think today, that we pretty well understand the processes which produce energy in “ordinary” stars, there is a plethora of theoretical models describing the more exotic objects in which particles can be accelerated to energies of 10^{20} eV and beyond. Until today, only a few particles, presumably protons, could be measured at these highest energies. But an accelerator which is capable to accelerate hadrons should also produce neutrinos in interactions of these hadrons with the surrounding shell, interstellar matter, or radiation. These neutrinos will propagate unperturbed to the Earth, conserving the direction and energy information. This is the big advantage compared to the detection of the hadrons, which reach us only after being deflected in the magnetic fields between the galaxies, and which might have undergone several interactions on their way, transferring some part of their energy to secondary particles. Measuring the ultra high energy neutrinos would allow us to better understand the processes taking place in these accelerators.

Since the neutrino flux decreases significantly with increasing energy, its detection requires ever larger target masses. Today, water Čerenkov detectors in the gigaton range (1 km^3 of water or ice) are being constructed, which will allow to detect neutrinos with energies up to about 100 TeV. The detection of neutrinos with energies up to 100 ZeV and above will require a teraton detector (1000 km^3 of water or ice). There are several experimental approaches to observe these big target masses, and it would be desirable to implement as many of them as possible, since there are no known calibration sources in this energy range, and thus cross calibration between different experiments, yielding different systematic errors, is essential.

In our study we investigate the thermoacoustic detection method, already proposed in 1957 by G.A. Askarian. An ultra high energy neutrino which interacts in a fluid, in our case sea water, produces a particle cascade which dissipates its energy in a narrow cylinder in the medium by heating this region. This leads to

a rapid expansion of the fluid which propagates as a bipolar sonic pulse of a few microseconds duration perpendicular to the shower axis. The disc-like pressure field can be described by an inhomogeneous wave equation (4.1). We have shown the validity of the model by experiments in which a 177 MeV proton beam and an infrared Nd:YAG laser beam were dumped into water tanks, and the acoustic signals produced were measured. The measured acoustic pulses agree with simulations based on the thermoacoustic model very well. Thus, we have proceeded to study the application of the thermoacoustic model to the detection of ultra high energy neutrinos, since the absorption length of sound in water is about ten times larger than the absorption length of light. These lengths determine the required spacing of the sensors in a detector. Therefore, using acoustic techniques, much larger target masses can be instrumented with the same number of sensors.

We envision an acoustic neutrino telescope set on the sea bed of, for example, the Mediterranean Sea. Since the total neutrino nucleon cross section (5.1) increases with energy, only neutrinos coming from above the horizon will be able to propagate to the detector. Neutrinos coming from below will be absorbed in the Earth. When the neutrino interacts, most of its energy is transferred to the lepton (a neutrino in the case of a neutral current interaction; a charged lepton in the case of a charged current interaction). This part of the total energy cannot be detected with an acoustic detector, since neutrinos deposit no energy in the medium and the energy deposition of muons and electrons is too sparse to produce a significant acoustic pulse, for the electrons due to the LPM effect occurring at these highest energies. The energy deposition of tau leptons, which produce hadronic cascades in the tau decay, was not investigated yet. The remaining energy is deposited by a hadronic cascade in a narrow volume of about 5 m in length and 2 cm in diameter, which is energy independent. From this energy deposition region bipolar acoustic pulses are emitted whose amplitude is proportional to the energy in the hadronic system.

These bipolar pulses propagate mainly perpendicular to the cascade axis. For their detection over large distances sound absorption in the water has to be taken into account. The absorption length is strongly frequency dependent, and is about 1 km for the central frequency of 20 kHz of the pulses. Based on Monte Carlo simulations of hadronic cascades, on the thermoacoustic model, and on the frequency dependent absorption length a parameterisation of the amplitude of the bipolar pulses was derived (Fig. 6.9). For the detection of the neutrino induced acoustic signals we use acoustic modules (AMs): Hypothetical devices which are able to detect bipolar pulses with an amplitude larger than some threshold pressure p_{th} in the ambient noise always present in the sea and record their amplitude and arrival time. The ambient noise is well known and fortunately has a minimum between 30 kHz and 200 kHz, depending on the weather conditions, the frequency range where main contributions of the signal are. Further it was shown that due to refraction no signals produced further away than 27 km from an AM can be detected, which sets a natural limit to the target mass that can be observed by a single AM.

Based on the acoustic modules a complete detector simulation code was developed and tested with an exemplary detector of 1 km^3 size containing 200 AMs. We have shown that a significant part (27%) of all neutrinos with energies between 10^8 GeV and 10^{16} GeV which interact in the surroundings of the detector generate a trigger, and that 79% of these triggered events can be reconstructed with a simple minimisation algorithm. The energy of the hadronic cascade can be determined up to a factor of 10, which is sufficient since all predicted neutrino fluxes extend over several orders of magnitude in energy. The direction resolution can be improved up to 12° with rigid selection cuts, but it is of only minor importance for diffuse neutrino fluxes. An important factor towards the realisation of an acoustic neutrino telescope will be the rate of background events with long correlation lengths, i.e. of natural or anthropogenic sources which produce causally correlated bipolar acoustic pulses that could be identified wrongly as neutrinos. So far, this rate is completely unknown, and the Erlangen ANTARES group has proposed an experiment to measure it within the ANTARES experimental setup.

We could show that using an underwater acoustic neutrino telescope with an instrumented volume of 1500 km^3 , where only 200 AM/km^3 would be required, many cosmological models predicting ultra high energy neutrino fluxes could be tested within 5 years of measurement time (Figs. 7.13 and 7.14). Such a detector would be a possible approach to the detection of ultra high energy cosmological neutrinos, which is complementary to the radio Čerenkov experiments currently under construction.

Chapter 9

Zusammenfassung

Die vorliegende Arbeit beschreibt eine Simulationsstudie zu einer neuen Nachweistechnik für höchstenergetische Neutrinos aus kosmischen Quellen: Der Nachweis thermoakustischer Schallpulse, die im Meer von neutrinoinduzierten Teilchenschauern erzeugt werden.

Physiker nehmen heutzutage an, die Energieerzeugung in „normalen“ Sternen sehr gut verstanden zu haben. Es gibt jedoch eine Vielzahl theoretischer Modelle, die exotische kosmische Objekte beschreiben, die in der Lage sind Teilchen auf Energien von 10^{20} eV oder höher zu beschleunigen. Bis heute konnten nur wenige dieser Teilchen — man geht davon aus, dass es sich um Protonen handelt — auf der Erde nachgewiesen werden. Ein Beschleuniger, der Hadronen auf solch hohe Energien beschleunigt, muss auch eine Quelle höchstenergetischer Neutrinos sein, die bei der Wechselwirkung der Protonen mit der umgebenden Materie oder Strahlung entstehen. Diese Neutrinos können als nur schwach wechselwirkende Teilchen, nachdem sie den Beschleuniger verlassen haben, die Erde ungestört erreichen. Neutrinos tragen, im Gegensatz zu Protonen, die in den intergalaktischen Magnetfeldern abgelenkt werden und mit dem Restgas wechselwirken können, wobei ein Teil ihrer Energie an Sekundärteilchen übertragen wird, eine Richtungs- und Energieinformation. Der Nachweis dieser höchstenergetischen Neutrinos würde einen tiefen Einblick in die Beschleunigungsprozesse, die in kosmologischen Objekten stattfinden, erlauben.

Da der Neutrinofluss mit zunehmender Energie stark abnimmt, werden immer größere Detektormassen zu seinem Nachweis benötigt. Derzeit geplante oder im Aufbau befindliche Wasser-Čerenkov Detektoren mit einer Masse von einer Gigatonne (1 km^3 Wasser oder Eis) ermöglichen den Nachweis von Neutrinos mit einer Energie von bis zu 100 TeV. Die Messung von Neutrinos mit Energien von 100 ZeV und darüber wird die Entwicklung von Detektoren mit einer Masse im Bereich einer Teratonne (1000 km^3 Wasser oder Eis) erfordern. Es gibt verschiedenste experimentelle Ansätze zur Instrumentierung solch großer Volumina, und es wäre sinnvoll in Zukunft möglichst viele von ihnen zu realisieren, da in diesem Energiebereich keinerlei Kalibrationsquellen bekannt sind. Somit ist ein Vergleich zwischen Ergebnissen, die mit verschiedenen experimentellen Techniken gemessen wurden

und somit unterschiedliche systematische Fehler aufweisen, unerlässlich.

Diese Studie beschäftigt sich mit der thermoakustischen Nachweismethode, die erstmals 1957 von G.A. Askarian vorgeschlagen wurde. Ein höchstenergetisches Neutrino wechselwirkt in einem Fluid, in diesem Fall Wasser, und es entsteht ein Teilchenschauer, dessen Energie innerhalb eines schmalen Zylinders in Form von Wärme an das Wasser abgegeben wird. Dies führt zu einer plötzlichen Ausdehnung der Flüssigkeit, und es breitet sich ein bipolarer akustischer Puls von wenigen Mikrosekunden Länge senkrecht zur Schauerachse aus. Das entstehende scheibenförmige Druckfeld kann durch die inhomogene Wellengleichung (4.1) beschrieben werden. Wir konnten dieses Modell in zwei Experimenten, in denen ein Strahl von 177 MeV Protonen, bzw. ein infraroter Nd:YAG Laser in einen mit Wasser gefüllten Tank geschossen wurden, und die dabei entstehenden akustischen Pulse aufgezeichnet wurden, bestätigen. Die gemessenen Signale stimmen mit Simulationsrechnungen, die unter der Annahme eines thermoakustischen Schallerzeugungsmechanismus gemacht wurden, sehr gut überein. Dieses Ergebnis ermutigte uns, die Möglichkeit des Nachweises ultrahochenergetischer Neutrinos mit einem akustischen Detektor weiter zu studieren, insbesondere da die Abschwächlänge von Schall in Wasser etwa zehn mal größer ist als die Abschwächlänge von Licht. Diese Abschwächlänge ist es, die den für einen Detektor zu wählenden Abstand zwischen den einzelnen Sensoren bestimmt. Somit kann mittels eines akustischen Detektors ein sehr viel größeres Volumen mit der selben Anzahl von Sensoren bestückt werden, als dies in einem optischen Detektor möglich wäre.

Wir untersuchen ein mögliches akustisches Neutrino teleskop auf dem Meeresgrund, zum Beispiel auf dem Grund des Mittelmeers. Da der totale Wirkungsquerschnitt (5.1) für die Wechselwirkung von Neutrinos mit Nukleonen mit wachsender Neutrinoenergie ansteigt, können bei höchsten Energien nur von oben kommende Neutrinos den Detektor erreichen; von unten kommende Neutrinos werden in der Erde absorbiert. Bei der Wechselwirkung wird ein Großteil der Neutrinoenergie auf das entstehende Lepton übertragen (ein geladenes Lepton im Falle einer Wechselwirkung über einen geladenen Strom; ein Neutrino im Falle einer Neutralstromwechselwirkung). Dieser Teil ist für die Detektion mit einem akustischen Neutrino teleskop verloren, da Neutrinos keine, und Muonen und Elektronen nur sehr dünn Energie im Medium deponieren, letztere auf Grund des LPM Effekts. Die Energiedeposition von Tau-Leptonen, bei deren Zerfall ein hadronischer Schauer entstehen kann, wurde im Rahmen dieser Arbeit nicht untersucht. Die verbleibende Energie wird in Form eines hadronischen Teilchenschauers in einem zylindrischen Volumen von etwa 5 m Länge und 2 cm Durchmesser abgegeben. In diesem Volumen, dessen Abmessungen energieunabhängig sind, wird dann ein bipolarer akustischer Puls ausgesendet, dessen Amplitude proportional zur Energie der hadronischen Kaskade ist.

Das Signal breitet sich hauptsächlich senkrecht zur Achse des Schauers aus. Beim Nachweis muss jedoch noch die Abschwächung des Signals im Wasser berücksichtigt

werden. Die stark frequenzabhängige Absorptionslänge beträgt für die 20 kHz Schwerpunktsfrequenz des Signals etwa 1 km. Basierend auf Monte Carlo Simulationen hadronischer Schauer, dem thermoakustischen Modell und der frequenzabhängigen Absorptionslänge wurde eine Parametrisierung der Amplitude des akustischen Pulses für beliebige Sensorpositionen entwickelt (Abb. 6.9). Für die Messung neutrinoinduzierter Schallpulse definieren wir ein hypothetisches *akustisches Modul* (AM): Ein Gerät, das bipolare akustische Schallpulse, wie sie zum Beispiel von neutrinoinduzierten hadronischen Schauern ausgesandt werden, mit einer Amplitude größer einer Schwelle p_{th} aus dem umgebenden Untergrundrauschen herausfiltern kann, und ihre Ankunftszeit und Amplitude messen und weitersenden kann. Das Umgebungsrauschen im Meer ist eine bekannte Größe, und hat ein Minimum zwischen 30 kHz und 200 kHz je nach Windstärke. Dies ist der Frequenzbereich in dem neutrinoinduzierten akustischen Pulse erwartet werden. Weiter konnte gezeigt werden, dass auf Grund von Brechung keine Signale, die weiter als 27 km von einem Detektor erzeugt werden, diesen erreichen können. Dadurch wird eine natürliche obere Grenze für das Volumen festgelegt, das mit einem einzelnen Sensor beobachtet werden kann.

Aufbauend auf akustischen Modulen wurde eine vollständige Detektor-Simulationkette entwickelt, und am Beispiel eines 1 km^3 großen Detektors bestehend aus 200 AMs untersucht. Wir konnten zeigen, dass ein erheblicher Teil (27%) aller in der Umgebung des Detektors wechselwirkenden Neutrinos mit einer Energie zwischen 10^8 GeV und 10^{16} GeV im Detektor Trigger auslösen, und dass für 79% dieser getriggerten Ereignisse die Richtung und Energie des hadronischen Schauers mit einem einfachen Minimierungs-Algorithmus bestimmt werden können. Die Energie kann bis auf einen Faktor 10 genau bestimmt werden, was noch ausreichend ist, da die zu untersuchenden kosmologischen Modelle ein Neutrinospektrum vorausagen, das sich über mehrere Zehnerpotenzen in der Energie erstreckt. Die Richtungsrekonstruktion kann mittels Schnitten bis auf 12° verbessert werden, was aber für diffuse Neutrinoflüsse nur eine untergeordnete Rolle spielt. Ein wichtiger Faktor bei der Realisierung eines akustischen Neutrinooteleskops wird die Rate des korrelierten Untergrunds sein, das heißt natürlicher oder anthropogener Schallquellen, die bipolare Pulse mit langer Korrelationslänge erzeugen, die fälschlicherweise als Neutrinos identifiziert werden könnten. Da diese Rate völlig unbekannt ist, plant die Erlanger ANTARES Gruppe ein Experiment mit dem diese Rate innerhalb der experimentellen Infrastruktur von ANTARES gemessen werden kann.

Wir konnten zeigen, dass ein akustisches Unterwasser-Neutrinooteleskop mit einem instrumentierten Volumen von 1500 km^3 , wobei lediglich 200 AM/km^3 benötigt würden, in der Lage wäre viele kosmologische Modelle, die einen Fluss ultrahoch-energetischer Neutrinos vorhersagen, innerhalb von fünf Jahren Messzeit zu testen (Abb. 7.13 und 7.14). Ein solches Experiment würde einen komplementären Ansatz zu den verschiedenen Radio Čerenkov Experimenten darstellen, die zur Zeit entwickelt werden.

Appendix A

Derivation of the thermoacoustic model

In this chapter the basic wave equation describing the connection between energy deposited in a fluid and the resulting acoustic pressure field is derived.

We consider an arbitrary compressible fluid, which can be described by five fields: the pressure $p(\vec{r}, t)$, the density $\rho(\vec{r}, t)$, and the velocity $\vec{v}(\vec{r}, t)$. It is important to note, that all fields describe the properties of the fluid at a fixed point (\vec{r}, t) in space and time, and *not* the properties of a moving volume element of the fluid.

First we note, that in the processes observed no fluid is created or destroyed, i.e. we have an equation of continuity for the mass of the fluid. Considering an arbitrary volume V with border ∂V we have:

$$\frac{d}{dt} \int_V d^3r \rho = - \oint_{\partial V} d\vec{\sigma} \cdot (\rho \vec{v}) \quad (\text{A.1})$$

The left hand side of this equation represents the increase of mass with time inside the volume V , which has to be equal to the mass flow into the element through its surface, which is written on the right hand side ($d\vec{\sigma}$ is defined to point to the outside of the volume, thus the minus sign). Using Gauss's integral theorem $\oint_{\partial V} d\vec{\sigma} \cdot (\rho \vec{v}) = \int_V d^3r \vec{\nabla} \cdot (\rho \vec{v})$, and noting that (A.1) is valid for all volumes V , we can write it in the differential form:

$$\frac{\partial \rho}{\partial t} + \vec{\nabla} \cdot (\rho \vec{v}) = 0 \quad (\text{A.2})$$

Next, we will derive Euler's law by noting, that the force \vec{F} applied by the whole fluid on the volume element V is:

$$\vec{F} = - \oint_{\partial V} d\vec{\sigma} p = - \int_V d^3r \vec{\nabla} p \quad (\text{A.3})$$

This allows us to write down the equation of motion for a single volume element dV with mass ρdV :

$$(\rho dV) \frac{d\vec{v}}{dt} = -dV \vec{\nabla} p \quad (\text{A.4})$$

We can write the total derivative of \vec{v} as a sum of partial derivatives:

$$d\vec{v} = \frac{\partial \vec{v}}{\partial t} dt + \sum_{j \in \{x,y,z\}} \frac{\partial \vec{v}}{\partial j} dj = \frac{\partial \vec{v}}{\partial t} dt + (\vec{dr} \cdot \vec{\nabla}) \vec{v}$$

or

$$\frac{d\vec{v}}{dt} = \frac{\partial \vec{v}}{\partial t} + (\vec{v} \cdot \vec{\nabla}) \vec{v}$$

Inserting this into (A.4) leads to Euler's law:

$$\frac{\partial \vec{v}}{\partial t} + (\vec{v} \cdot \vec{\nabla}) \vec{v} = -\frac{\vec{\nabla} p}{\rho} \quad (\text{A.5})$$

For the derivation of the thermoacoustic model we consider a fluid at rest in a static state. The acoustic waves are considered to be small deviations from the static quantities:

$$\begin{aligned} p_{\text{tot}}(\vec{r}, t) &= p_0 + p(\vec{r}, t) & p \ll p_0 \forall(\vec{r}, t) \\ \rho_{\text{tot}}(\vec{r}, t) &= \rho_0 + \rho(\vec{r}, t) & \rho \ll \rho_0 \forall(\vec{r}, t) \\ \vec{v}_{\text{tot}}(\vec{r}, t) &= \vec{0} + \vec{v}(\vec{r}, t) \end{aligned} \quad (\text{A.6})$$

We further assume that these deviations vary slowly enough in space and time, that their derivatives can also be considered as small quantities. Substituting these terms in the equation of continuity (A.2), and neglecting terms which are the product of two or more small quantities, we get:

$$\frac{\partial \rho}{\partial t} + \rho_0 (\vec{\nabla} \cdot \vec{v}) = 0 \quad (\text{A.7})$$

Euler's law (A.5) is reduced to:

$$\frac{\partial \vec{v}}{\partial t} = -\frac{\vec{\nabla} p}{\rho_0} \quad (\text{A.8})$$

We now take the partial time derivative of (A.7), exchange the spatial and temporal derivatives, and substitute (A.8):

$$0 = \frac{\partial^2 \rho}{\partial t^2} + \rho_0 \left(\vec{\nabla} \cdot \frac{\partial \vec{v}}{\partial t} \right) = \frac{\partial^2 \rho}{\partial t^2} - \vec{\nabla} \cdot (\vec{\nabla} p)$$

or

$$\frac{\partial^2 \rho}{\partial t^2} - \Delta p = 0 \quad (\text{A.9})$$

Let us now, for simplicity, consider first the adiabatic case, where the density is a function of the pressure only: $\rho_{\text{tot}} = \rho_{\text{tot}}(p_{\text{tot}})$. We expand $\rho_{\text{tot}}(p_{\text{tot}})$ in a Taylor series around p_0 :

$$\rho = \rho_{\text{tot}}(p_0 + p) - \rho_{\text{tot}}(p_0) \approx \frac{d\rho}{dp}(p_0) p =: \frac{1}{c^2} p$$

Therefore, for the adiabatic case we get the following simple wave equation, where c is the speed of sound:

$$\frac{1}{c^2} \frac{\partial^2 p}{\partial t^2} - \Delta p = 0 \quad (\text{A.10})$$

If we consider the case important for particle detection, we have to investigate the process where energy is deposited with an energy density $\varepsilon(\vec{r}, t)$. This process is not adiabatic, and leads to local heating and expansion of the fluid. Thus, the local density is not a function of the pressure only any more, but of the pressure *and* the deposited energy. We get:

$$d\rho = \left(\frac{\partial \rho}{\partial p} \right)_E dp + \left(\frac{\partial \rho}{\partial E} \right)_p dE$$

where the derivative $\partial \rho / \partial p$ at constant energy E results in the speed of sound $1/c^2$ again. For the derivative $\partial \rho / \partial E$ at constant pressure we look at an infinitesimal volume element V with mass m :

$$\left(\frac{\partial \rho}{\partial E} \right)_p = \left(\frac{\partial}{\partial E} \frac{m}{V} \right)_p = -\frac{m}{V^2} \left(\frac{\partial V}{\partial E} \right)_p \approx -\frac{\rho}{V} \left(\frac{\Delta V}{\Delta E} \right)$$

The change of the volume ΔV can be calculated from specific heat capacity at constant pressure C_p , and the thermal bulk expansion coefficient α as

$$\Delta V = \frac{\alpha}{\rho C_p} \Delta E$$

We finally get:

$$d\rho = \frac{1}{c^2} dp - \frac{\alpha}{C_p} d\varepsilon$$

where $d\varepsilon = dE/V$ is the energy density in the infinitesimal volume element V . Substituting this into (A.9) we arrive at the thermoacoustic model which describes the pressure field produced by energy with an energy density distribution $\varepsilon(\vec{r}, t)$ deposited in a fluid.

$$\frac{1}{c^2} \frac{\partial^2 p}{\partial t^2} - \Delta p = \frac{\alpha}{C_p} \frac{\partial^2 \varepsilon}{\partial t^2} \quad (\text{A.11})$$

Appendix B

On the calculation of flux limits

No existing experiment has detected any extra-galactic neutrinos so far, so the only published results are upper limits on the neutrino flux. On the other hand, new experiments publish limits on the lowest neutrino flux they will be able to detect in a given lifetime

When comparing limits on the neutrino flux presented by different experiments one has to be aware that there are different methods to calculate these limits. In this section, these methods are derived, and the possibility to compare results obtained with different methods are discussed.

We assume a constant and isotropic flux of neutrinos $\Phi(E)$, which depends only on the neutrino energy E . Then the mean number of events $\langle N_{\text{ev}} \rangle$ expected to be detected by an experiment is given by

$$\langle N_{\text{ev}} \rangle = \int dE \int dt \int d\Omega \Phi(E) A_{\text{eff}}(E, \Omega) \quad (\text{B.1})$$

The above equation can also be read as a definition for the effective area A_{eff} of the experiment. The effective area depends on the neutrino cross section, and thus on its energy, and it depends further on the detection mechanism and the geometrical acceptance of the detector, i.e. on the direction of incidence Ω . A_{eff} is either calculated analytically or by Monte Carlo simulations including all aspects of a given detector.

For an isotropic neutrino flux one can define the aperture $\mathcal{A}(E)$ of the detector:

$$\mathcal{A}(E) = \int d\Omega A_{\text{eff}}(E, \Omega) \quad (\text{B.2})$$

and thus

$$\langle N_{\text{ev}} \rangle = \int dE \int dt \Phi(E) \mathcal{A}(E) \quad (\text{B.3})$$

If further the flux is constant in time, the lifetime T of the experiment can be introduced:

$$\langle N_{\text{ev}} \rangle = T \int dE \Phi(E) \mathcal{A}(E) \quad (\text{B.4})$$

Let us assume that the number of events N_{ev} detected by a given experiment during its lifetime T follows a Poisson distribution with mean value $\langle N_{\text{ev}} \rangle$, and that the mean number of background events expected to be detected during the time T is zero (which is true for most ultra high energy neutrino experiments). Then, if the experiment has detected no events ($N_{\text{ev}} = 0$), it can be derived [67] that the true mean value $\langle N_{\text{ev}} \rangle$ is inside the interval $[0, 2.44]$ with a confidence of 90% ($[0, 3.09]$ with a confidence of 95%).

Thus, setting $\langle N_{\text{ev}} \rangle = 2.44$ results in an upper limit $\Phi_{90}(E)$ on the real neutrino flux with a confidence level of 90%:

$$\int dE \Phi(E) \mathcal{A}(E) \leq \frac{2.44}{T} \quad (90\% \text{ C.L.}) \quad (\text{B.5})$$

or

$$\int dE \Phi_{90}(E) \mathcal{A}(E) = \frac{2.44}{T} \quad (\text{B.6})$$

To solve this equation further to get $\Phi_{90}(E)$, one has to make certain assumptions on the flux. There are three assumptions commonly used in the literature:

Limit on a given source model. It is assumed that the neutrino spectrum to be measured follows a given functional form determined by a certain theoretical source model:

$$\Phi_{90}(E) = \mathcal{N} \Phi_{\text{model}}(E) \quad (\text{B.7})$$

where \mathcal{N} is a normalisation constant for the neutrino flux, which can then be calculated from:

$$\mathcal{N} = \frac{2.44}{T \int dE \Phi_{\text{model}}(E) \mathcal{A}(E)} \quad (\text{B.8})$$

which can be solved analytically or numerically, since the aperture $\mathcal{A}(E)$ is a known quantity.

Often power-law spectra $\Phi(E) \propto E^{-\alpha}$ are used, which are typical hadronic source spectra expected from many cosmological accelerator models. Especially a spectral index of $\alpha = 2$ is expected from first order Fermi acceleration.

$$\Phi_{90}(E) = \mathcal{N} E^{-2} \quad (\text{B.9})$$

Limits based on power-law spectra can be recognised as straight lines in double-logarithmic flux plots, where α determines the slope. Especially the important case of $\alpha = 2$ reduces to a constant in the $E^2 \Phi$ plots used in this work.

Non-detection in a given energy-interval. There are two possibilities of calculating model independent limits. The above model dependent limit was derived from the non-detection of any neutrinos over the whole energy range covered by the model. For an experiment with an energy resolution better than this range, a limit can be set on every energy interval compatible with the energy resolution.

Typical energy resolutions $\Delta E/E$ for neutrino telescopes are of the order of 3 to 10. So a common value for the non-detection energy interval found in the literature is one decade in energy, i.e. an energy range $[E, 10E]$.

If further the aperture can be assumed constant around some mean energy \bar{E} of the energy interval with length ΔE , or some mean aperture $\bar{\mathcal{A}}(\bar{E})$ over the interval can be used, the equation for the flux limit can be linearised to

$$\Delta E \Phi_{90}(\bar{E}) \bar{\mathcal{A}}(\bar{E}) = \frac{2.44}{T} \quad (\text{B.10})$$

and thus

$$\Phi_{90}(\bar{E}) = \frac{2.44}{T \Delta E \bar{\mathcal{A}}(\bar{E})} \quad (\text{B.11})$$

Model independent estimate. The FORTE collaboration suggests a method to derive a flux limit which is independent of a given functional form of the source spectrum, but only assumes that the source spectrum is smooth (i.e. the source spectrum can be written as linear combination of a set of functions to be defined below) [29].

We assume a source model flux, that depends on an additional parameter or set of parameters P :

$$\Phi(E, P) = \mathcal{N} \Phi_{\text{model}}(E, P) \quad (\text{B.12})$$

Then, using the model dependent limit (B.8), we come to the following relation:

$$\Phi(E, P) \leq \frac{2.44 \Phi_{\text{model}}(E, P)}{T \int dE' \Phi_{\text{model}}(E', P) \mathcal{A}(E')} \quad (\text{B.13})$$

We get a conservative, but always valid upper limit which is independent of the parameter P if we take the maximum value of the right hand side for every energy:

$$\Phi(E) \leq \max_P \frac{2.44 \Phi_{\text{model}}(E, P)}{T \int dE' \Phi_{\text{model}}(E', P) \mathcal{A}(E')} \quad (\text{B.14})$$

In the next step we will prove that the above relation is valid for *any* linear combination of flux models, i.e.:

$$\Phi(E) = \int dP \mathcal{N}(P) \Phi_{\text{model}}(E, P) \quad (\text{B.15})$$

The proof assumes the opposite of the above relation, i.e. we assume that *for all* P :

$$\Phi(E) > \frac{2.44 \Phi_{\text{model}}(E, P)}{T \int dE' \Phi_{\text{model}}(E', P) \mathcal{A}(E')}$$

or

$$\int dE' \Phi_{\text{model}}(E', P) \mathcal{A}(E') > \frac{2.44 \Phi_{\text{model}}(E, P)}{T \Phi(E)} \quad (\text{B.16})$$

we multiply both sides by $\mathcal{N}(P)$ and integrate over all P

$$\int dE' \left(\int dP \mathcal{N}(P) \Phi_{\text{model}}(E', P) \right) \mathcal{A}(E') > \frac{2.44}{T \Phi(E)} \int dP \mathcal{N}(P) \Phi_{\text{model}}(E', P)$$

using definition (B.15) of $\Phi(E)$ we get

$$\int dE' \Phi(E') \mathcal{A}(E') > \frac{2.44}{T}$$

which is in contradiction to our initial assumption (B.5) about the flux at 90% C.L.

So for any flux which can be represented as an arbitrary linear combination of functions $\Phi_{\text{model}}(E, P)$, the upper limit at 90% confidence level can be written as:

$$\Phi_{90}(E) = \max_P \frac{2.44 \Phi_{\text{model}}(E, P)}{T \int dE' \Phi_{\text{model}}(E', P) \mathcal{A}(E')} \quad (\text{B.17})$$

This can be simplified very much if we restrain ourselves to a set of convex curves $\Phi_C(E, E_0)$, which have their maximum at E_0 each, and have a width of $\approx E_0$. The curves shall be normalised, so that $\int dE \Phi_C(E, E_0) = 1$. Then we have at the maximum $\max_E \Phi_C(E, E_0) \lesssim 1/E_0$. If further the aperture $\mathcal{A}(E)$ is smooth enough that it can be assumed constant over the validity of a certain Φ_C , so that $\int dE \Phi_C(E, E_0) \mathcal{A}(E) \approx \mathcal{A}(E_0)$, equation (B.17) is reduced to:

$$\Phi_{90}(E) = \frac{2.44}{TE\mathcal{A}(E)} \quad (\text{B.18})$$

This result deviates from the one of the non-detection in a given interval by a constant factor if energy intervals of constant width in $\log E$ are used, which usually is the case. Further, this factor is of the order of unity if the energy E in the latter model compares to the mean value \bar{E} of a decade in energy of the second model presented.

Bibliography

- [1] V. F. Hess, “Über Beobachtungen der durchdringenden Strahlung bei sieben Freiballonfahrten,” *Physik. Zeitschr.* **XIII** (1912) 1084–1091.
- [2] C. L. Cowan, F. Reines, F. B. Harrison, H. W. Kruse, and A. D. McGuire, “Detection of the free neutrino: A Confirmation,” *Science* **124** (1956) 103–104.
- [3] F. Reines and C. Cowan, “The Neutrino,” *Nature* **178** (1956) 446–449.
- [4] M. S. Longair, *High Energy Astrophysics*, vol. 2. Cambridge University Press, second ed., 1994.
- [5] F. W. Stecker, C. Done, M. H. Salamon, and P. Sommers, “High-energy neutrinos from active galactic nuclei,” *Phys. Rev. Lett.* **66** (1991) 2697–2700. [Erratum-ibid. **69** (1992) 2738].
- [6] F. W. Stecker, “A note on high energy neutrinos from AGN cores,” [astro-ph/0510537](#).
- [7] F. Halzen and E. Zas, “Neutrino fluxes from active galaxies: A model-independent estimate,” *Astrophys. J.* **488** (1997) 669–674, [astro-ph/9702193](#).
- [8] R. Wischnewski *et al.*, “The Baikal neutrino telescope: Results and plans,” [astro-ph/0507698](#).
- [9] P. Mészáros, “Gamma-ray bursts: Afterglow implications, progenitor clues and prospects,” *Science* **291** (2001) 79–84, [astro-ph/0102255](#).
- [10] E. Waxman and J. N. Bahcall, “High energy neutrinos from cosmological gamma-ray burst fireballs,” *Phys. Rev. Lett.* **78** (1997) 2292–2295, [astro-ph/9701231](#).
- [11] E. Waxman and J. N. Bahcall, “High energy neutrinos from astrophysical sources: An upper bound,” *Phys. Rev.* **D59** (1999) 023002, [hep-ph/9807282](#).

- [12] J. N. Bahcall and E. Waxman, “High energy astrophysical neutrinos: The upper bound is robust,” *Phys. Rev.* **D64** (2001) 023002, [hep-ph/9902383](#).
- [13] K. Greisen, “End to the cosmic ray spectrum?,” *Phys. Rev. Lett.* **16** (1966) 748–750.
- [14] G. T. Zatsepin and V. A. Kuzmin, “Upper limit of the spectrum of cosmic rays,” *JETP Lett.* **4** (1966) 78–80.
- [15] J. N. Bahcall and E. Waxman, “Has the GZK cutoff been discovered?,” *Phys. Lett.* **B556** (2003) 1–6, [hep-ph/0206217](#).
- [16] R. Engel, D. Seckel, and T. Stanev, “Neutrinos from propagation of ultra-high energy protons,” *Phys. Rev.* **D64** (2001) 093010, [astro-ph/0101216](#).
- [17] J. Bernstein, *An Introduction to Cosmology*. Prentice-Hall, 1998.
- [18] T. J. Weiler, “Resonant absorption of cosmic ray neutrinos by the relic neutrino background,” *Phys. Rev. Lett.* **49** (1982) 234.
- [19] E. Roulet, “Ultrahigh-energy neutrino absorption by neutrino dark matter,” *Phys. Rev.* **D47** (1993) 5247–5252.
- [20] A. Gangui, “Cosmology from topological defects,” *AIP Conf. Proc.* **668** (2003) 226–262, [astro-ph/0303504](#).
- [21] S. Yoshida, H. Dai, C. C. H. Jui, and P. Sommers, “Extremely high energy neutrinos and their detection,” *Astrophys. J.* **479** (1997) 547–559, [astro-ph/9608186](#).
- [22] Z. Fodor, S. D. Katz, and A. Ringwald, “Determination of absolute neutrino masses from bursts of Z bosons in cosmic rays,” *Phys. Rev. Lett.* **88** (2002) 171101, [hep-ph/0105064](#).
- [23] F. Halzen and D. Hooper, “High energy neutrinos from the TeV blazar 1ES 1959+650,” *Astropart. Phys.* **23** (2005) 537–542, [astro-ph/0502449](#).
- [24] G. A. Askarian, “Excess negative charge of an electron-photon shower and its coherent radio emission,” *Sov. Phys. JETP.* **14** (1962) 441–443.
- [25] D. Saltzberg *et al.*, “Observation of the Askaryan effect: Coherent microwave Cherenkov emission from charge asymmetry in high energy particle cascades,” *Phys. Rev. Lett.* **86** (2001) 2802–2805, [hep-ex/0011001](#).
- [26] I. Kravchenko *et al.*, “Performance and simulation of the RICE detector,” *Astropart. Phys.* **19** (2003) 15–36, [astro-ph/0112372](#).

-
- [27] P. W. Gorham, K. M. Liewer, C. J. Naudet, D. P. Saltzberg, and D. R. Williams, “Radio limits on an isotropic flux of > 100 EeV cosmic neutrinos,” *astro-ph/0102435*.
- [28] J. Bacelar, O. Scholten, G. de Bruyn, and H. Falcke, “Using the Westerbork radio observatory to detect UHE cosmic particles interacting on the moon.” Presented at the 1st International ARENA Workshop, DESY Zeuthen, Germany, May 17-19, 2005.
- [29] N. G. Lehtinen, P. W. Gorham, A. R. Jacobson, and R. A. Roussel-Dupre, “FORTE satellite constraints on ultra-high energy cosmic particle fluxes,” *Phys. Rev.* **D69** (2004) 013008, *astro-ph/0309656*.
- [30] P. Miočinović *et al.*, “Tuning into UHE neutrinos in Antarctica: The ANITA experiment,” *eConf* **C041213** (2004) 2516, *astro-ph/0503304*.
- [31] X. Bertou, P. Billoir, O. Deligny, C. Lachaud, and A. Letessier-Selvon, “Tau neutrinos in the Auger observatory: A new window to UHECR sources,” *Astropart. Phys.* **17** (2002) 183–193, *astro-ph/0104452*.
- [32] P. W. Gorham *et al.*, “Experimental limit on the cosmic diffuse ultra-high energy neutrino flux,” *Phys. Rev. Lett.* **93** (2004) 041101, *astro-ph/0310232*.
- [33] G. A. Askarian *At. Energ.* **3** (1957) 152.
- [34] G. A. Askarian, B. A. Dolgoshein, A. N. Kalinovsky, and N. V. Mokhov, “Acoustic detection of high energy particle-showers in water,” *Nucl. Instrum. Meth.* **164** (1979) 267–278.
- [35] H.-J. Kretzschmar, “Stoffwertsammlung Technische Thermodynamik: Wärme- und Stoffübertragung.” University of Applied Sciences Zittau/Görlitz. [Table 4. Based on data of the International Association for the Properties of Water and Steam (<http://www.iapws.org/>)].
- [36] N. Budnev, “The high frequency noise as a background for acoustic detection of high energy neutrinos in the Lake Baikal.” Presented at the 1st International ARENA Workshop, DESY Zeuthen, Germany, May 17-19, 2005.
- [37] N. G. Lehtinen, S. Adam, G. Gratta, T. K. Berger, and M. J. Buckingham, “Sensitivity of an underwater acoustic array to ultra-high energy neutrinos,” *Astropart. Phys.* **17** (2002) 279–292, *astro-ph/0104033*.
- [38] G. Riccobene, L. Cosentino, M. Musumeci, G. Pavan, and F. Speziale, “Acoustic detection of UHE neutrinos: A station for measurement of the deep sea acoustic noise,” *Nucl. Instrum. Meth.* **A518** (2004) 220–222.

- [39] C. Naumann, G. Anton, K. Graf, J. Höfl, A. Kappes, T. Karg, U. Katz, R. Lahmann, and K. Salomon, “Development of acoustic sensors for the ANTARES experiment.” Presented at the 1st International ARENA Workshop, DESY Zeuthen, Germany, May 17-19, 2005.
- [40] J. Vandenbroucke, G. Gratta, and N. Lehtinen, “Experimental study of acoustic ultra-high-energy neutrino detection,” *Astrophys. J.* **621** (2005) 301–312, [astro-ph/0406105](#).
- [41] L. Sulak *et al.*, “Experimental studies of the acoustic signature of proton beams traversing fluid media,” *Nucl. Instr. Meth.* **161** (1979) 203.
- [42] S. D. Hunter *et al.*, “Acoustic signals of nonthermal origin from high energy protons in water,” *J. Acoust. Soc. Am.* **69** (1981) 1557–1562.
- [43] V. I. Albul *et al.*, “Measurements of the parameters of the acoustic radiation accompanying the moderation of an intense proton beam in water,” *Instrum. Exp. Tech.* **44** (2001) 327–334.
- [44] K. Graf, “Teststrahlmessungen zur akustischen Neutrinodetektion: Thermoakustische Schallerzeugung in Wasser,” Diploma thesis, Friedrich-Alexander-Universität Erlangen-Nürnberg, July, 2004. FAU-PI1-DIPL-04-002.
- [45] K. Graf, G. Anton, J. Höfl, A. Kappes, T. Karg, U. Katz, R. Lahmann, C. Naumann, K. Salomon, and C. Stegmann, “Testing thermo-acoustic sound generation in water with proton and laser beams.” Presented at the 1st International ARENA Workshop, DESY Zeuthen, Germany, May 17-19, 2005.
- [46] S. Agostinelli *et al.*, “GEANT4: A simulation toolkit,” *Nucl. Instrum. Meth.* **A506** (2003) 250–303.
- [47] S. Schwemmer, “Testmessungen zur akustischen Neutrinodetektion mit einem Nd:YAG-Laser,” Diploma thesis, Friedrich-Alexander-Universität Erlangen-Nürnberg, Apr., 2005. FAU-PI1-DIPL-05-002.
- [48] J. P. Ralston, D. W. McKay, and G. M. Frichter, “The ultra high energy neutrino nucleon cross section,” [astro-ph/9606007](#).
- [49] A. Gazizov and M. P. Kowalski, “ANIS: High energy neutrino generator for neutrino telescopes,” *Comput. Phys. Commun.* **172** (2005) 203–213, [astro-ph/0406439](#).

-
- [50] L. D. Landau and I. Pomeranchuk, “Limits of applicability of the theory of bremsstrahlung electrons and pair production at high energies,” *Dokl. Akad. Nauk Ser. Fiz.* **92** (1953) 535–536.
- [51] L. D. Landau and I. Pomeranchuk, “Electron cascade process at very high energies,” *Dokl. Akad. Nauk Ser. Fiz.* **92** (1953) 735–738.
- [52] A. B. Migdal, “Bremsstrahlung and pair production in condensed media at high energies,” *Phys. Rev.* **103** (1956) 1811–1820.
- [53] S. Eidelman *et al.*, “Review of particle physics,” *Phys. Lett.* **B592** (2004) 1.
- [54] J. Alvarez-Muñiz and E. Zas, “Cherenkov radio pulses from EeV neutrino interactions: The LPM effect,” *Phys. Lett.* **B411** (1997) 218–224, [astro-ph/9706064](#).
- [55] R. J. Urick, *Principles of underwater sound*. Peninsula Publishing, 1983.
- [56] G. S. Verma, “Ultrasonic absorption due to chemical relaxation in electrolytes,” *Revs. Modern Phys.* **31** (1959) 1052–1071.
- [57] J. A. Aguilar *et al.*, “Transmission of light in deep sea water at the site of the ANTARES neutrino telescope,” *Astropart. Phys.* **23** (2005) 131–155, [astro-ph/0412126](#).
- [58] P. Askebjerg *et al.*, “Optical properties of the South Pole ice at depths between 0.8 km and 1 km,” *Science* **267** (1995) 1147–1150, [astro-ph/9412028](#).
- [59] V. Niess, “Underwater acoustic positioning in ANTARES,” in *Proceedings of the 29th International Cosmic Ray Conference*. Pune, India, August 3-10, 2005.
- [60] R. J. Urick, *Ambient Noise in the Sea*. Peninsula Publishing, 1986.
- [61] S. Danaher *et al.*, “The UK ACoRNE group: Present projects and future plans.” Presented at the 1st International ARENA Workshop, DESY Zeuthen, Germany, May 17-19, 2005.
- [62] T. Karg, G. Anton, K. Graf, J. Höfl, A. Kappes, U. Katz, R. Lahmann, C. Naumann, K. Salomon, and S. Schwemmer, “Development of acoustic devices for ultra-high energy neutrino detectors,” in *Proceedings of the 29th International Cosmic Ray Conference*. Pune, India, August 3-10, 2005. [astro-ph/0509455](#).

- [63] R. Lahmann, G. Anton, K. Graf, J. Höfl, A. Kappes, T. Karg, U. Katz, C. Naumann, and K. Salomon, “Integration of acoustic detection equipment into ANTARES.” Presented at the 1st International ARENA Workshop, DESY Zeuthen, Germany, May 17-19, 2005.
- [64] J. Perkin, “ACoRNE simulation work.” Presented at the 1st International ARENA Workshop, DESY Zeuthen, Germany, May 17-19, 2005.
- [65] V. Niess, “Détection acoustique sous-marine de neutrinos de ultra haute énergie dans le cadre de l’expérience ANTARES,” PhD thesis, Université de la Méditerranée, Aix-Marseille II, Sept., 2005.
- [66] D. Besson, S. Böser, R. Nahnauer, P. B. Price, and J. A. Vandenbroucke, “Simulation of a Hybrid Optical/Radio/Acoustic Extension to IceCube for EeV Neutrino Detection,” in *Proceedings of the 29th International Cosmic Ray Conference*. Pune, India, August 3-10, 2005.
- [67] G. J. Feldman and R. D. Cousins, “A unified approach to the classical statistical analysis of small signals,” *Phys. Rev.* **D57** (1998) 3873–3889, physics/9711021.

Danksagung

Viele Menschen haben zum Gelingen dieser Arbeit beigetragen, so dass ich mich zuerst bei denjenigen entschuldigen möchte, die hier keine namentliche Erwähnung finden.

Mein besonderer Dank gilt Frau Prof. Dr. Gisela Anton, die mir beim Anfertigen dieser Arbeit alle Freiheiten ließ, und mir dennoch stets mit Rat und Tat weiterhelfen konnte.

Den Mitarbeitern der Arbeitsgruppen Astroteilchenphysik und Medizinphysik, mittlerweile mehr, als dass ich sie hier alle einzeln nennen könnte, danke ich für die angenehme Arbeitsatmosphäre und fortwährende Diskussionsbereitschaft, ohne die diese Arbeit niemals vollendet worden wäre. Besonders möchte ich bei meinem langjährigen Zimmerkollegen Norman Uhlmann bedanken, der mir geholfen hat dem ständigen Rechner-Wahnsinn Herr zu werden.

Den Mitgliedern der ANTARES Kollaboration schulde ich Dank für die freundliche Aufnahme und die steten Bemühungen mein Französisch zu verbessern. Insbesondere sei hier Valentin Niess genannt, mit dem ich viele fruchtbare Diskussionen über akustische Detektion führen durfte.

Ich danke Felix, Jürgen, Kay und Klaus für das Korrekturlesen der Arbeit, sowie Herrn Prof. Dr. Karl-Heinz Kampert für die bereitwillige Übernahme des Zweitgutachtens.

Lebenslauf

Persönliche Daten:

Timo Thomas Karg
Hartmannstraße 89
91052 Erlangen
Geburtsdatum: 30. September 1976
Geburtsort: Nürnberg

Hochschulausbildung:

08/2002 Beginn des Promotionsstudiums
Physikalisches Institut, Abt. 4
Universität Erlangen-Nürnberg
10/1997 – 07/2002 Grund- und Hauptstudium (Physik, Diplom)
Universität Erlangen-Nürnberg
06/2001 – 06/2002 Anfertigung der Diplomarbeit
Physikalisches Institut, Abt. 4
Thema: „Entwicklung eines Bildrekonstruktions-
algorithmus für die Compton-Kamera“
10/1999 – 03/2000 ERASMUS Stipendiat
Imperial College, London
07/1999 Diplom-Vorprüfung

Zivildienst:

07/1996 – 07/1997 Klinikum Süd der Stadt Nürnberg

Schulbildung:

1987 – 1996 Martin-Behaim-Gymnasium, Nürnberg
1983 – 1987 Grundschule Zugspitzstraße, Nürnberg

Berufserfahrung:

seit 08/2002 Wissenschaftlicher Angestellter
Physikalisches Institut, Abt. 4
Universität Erlangen-Nürnberg

